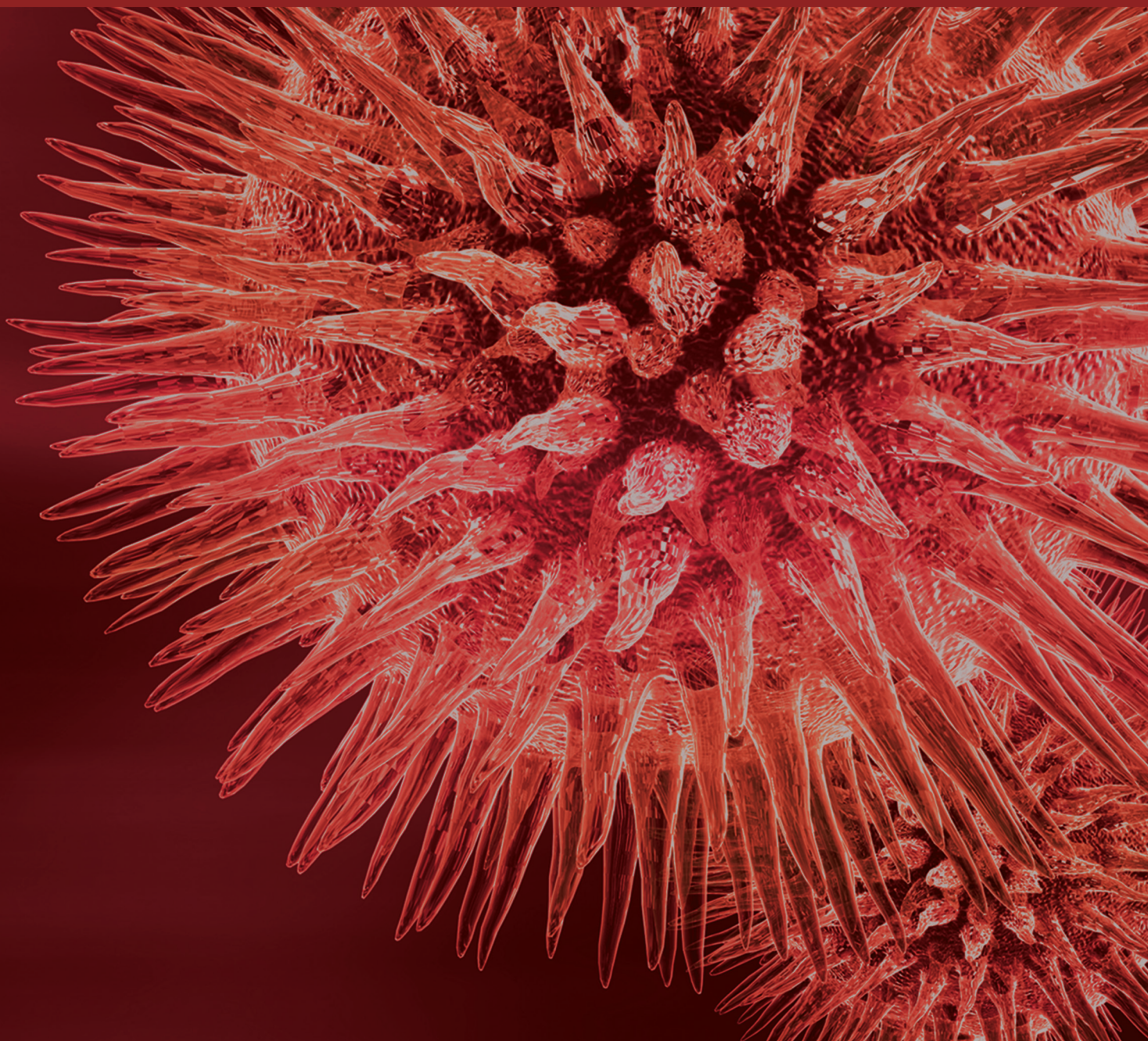


Novel Technologies for Improved Treatment Outcome and Patient Safety in Cancer Radiotherapy

Guest Editors: Jun Deng, Yuanming Feng, Charlie Ma, and Fang-Fang Yin





**Novel Technologies for
Improved Treatment Outcome and
Patient Safety in Cancer Radiotherapy**

BioMed Research International

**Novel Technologies for
Improved Treatment Outcome and
Patient Safety in Cancer Radiotherapy**

Guest Editors: Jun Deng, Yuanming Feng, Charlie Ma,
and Fang-Fang Yin



Copyright © 2016 Hindawi Publishing Corporation. All rights reserved.

This is a special issue published in “BioMed Research International.” All articles are open access articles distributed under the Creative Commons Attribution License, which permits unrestricted use, distribution, and reproduction in any medium, provided the original work is properly cited.

Contents

Novel Technologies for Improved Treatment Outcome and Patient Safety in Cancer Radiotherapy

Jun Deng, Yuanming Feng, Charlie Ma, and Fang-Fang Yin

Volume 2016, Article ID 3016454, 2 pages

3D-2D Deformable Image Registration Using Feature-Based Nonuniform Meshes

Zichun Zhong, Xiaohu Guo, Yiqi Cai, Yin Yang, Jing Wang, Xun Jia, and Weihua Mao

Volume 2016, Article ID 4382854, 19 pages

Combining Whole-Brain Radiotherapy with Gefitinib/Erlotinib for Brain Metastases from Non-Small-Cell Lung Cancer: A Meta-Analysis

Mao-hua Zheng, Hong-tao Sun, Ji-guang Xu, Gang Yang, Lei-ming Huo, Pan Zhang, Jin-hui Tian, and Ke-hu Yang

Volume 2016, Article ID 5807346, 9 pages

Replanning Criteria and Timing Definition for Parotid Protection-Based Adaptive Radiation Therapy in Nasopharyngeal Carcinoma

Wei-Rong Yao, Shou-Ping Xu, Bo Liu, Xiu-Tang Cao, Gang Ren, Lei Du, Fu-Gen Zhou, Lin-Chun Feng, Bao-Lin Qu, Chuan-Bin Xie, and Lin Ma

Volume 2015, Article ID 476383, 8 pages

Volumetric Modulated Arc Therapy of the Pelvic Lymph Nodes to the Aortic Bifurcation in Higher Risk Prostate Cancer: Early Toxicity Outcomes

Gina Hesselberg, Gerald Fogarty, Lauren Haydu, Nicole Dougheney, and Phillip Stricker

Volume 2015, Article ID 696439, 8 pages

An IMRT/VMAT Technique for Nonsmall Cell Lung Cancer

Nan Zhao, Ruijie Yang, Junjie Wang, Xile Zhang, and Jinna Li

Volume 2015, Article ID 613060, 7 pages

Editorial

Novel Technologies for Improved Treatment Outcome and Patient Safety in Cancer Radiotherapy

Jun Deng,¹ Yuanming Feng,² Charlie Ma,³ and Fang-Fang Yin⁴

¹*Department of Therapeutic Radiology, Yale University, New Haven, CT 06510, USA*

²*Department of Biomedical Engineering, Tianjin University, Tianjin 300072, China*

³*Department of Radiation Oncology, Fox Chase Cancer Center, Philadelphia, PA 19111, USA*

⁴*Department of Radiation Oncology, Duke University, Durham, NC 27710, USA*

Correspondence should be addressed to Jun Deng; jun.deng@yale.edu

Received 17 January 2016; Accepted 17 January 2016

Copyright © 2016 Jun Deng et al. This is an open access article distributed under the Creative Commons Attribution License, which permits unrestricted use, distribution, and reproduction in any medium, provided the original work is properly cited.

Cancer radiotherapy has been largely driven by technological development in the past thirty years, resulting in improved local tumor control for a variety of lesion sites [1]. Yet the paradigm has shifted more recently toward a patient-centered healthcare model and value-based medicine where success is measured by improved treatment outcome, enhanced patient safety, and increased patient satisfaction [2]. Clinically, local tumor control should be optimized simultaneously with treatment outcome and patient safety in order to maximize the therapeutic ratio while maintaining a high standard of patient care. This special issue aims to present some of the novel technological developments in recent years and discuss their potentials in improving treatment outcome and patient safety in the radiotherapeutic management of cancers worldwide.

The research work entitled “An IMRT/VMAT Technique for Non-Small Cell Lung Cancer” investigated a novel approach in treating non-small cell lung cancer (NSCLC) with radiation, that is, a hybrid intensity-modulated radiotherapy (IMRT) and volumetric modulated arc therapy (VMAT) technique, in order to achieve the delivery efficiency from VMAT and the critical structure sparing with IMRT. The proposed hybrid approach involved an initial IMRT plan delivering the first half of the total prescription dose, followed by a VMAT plan delivering the second half of the total dose, which was optimized based on the initially optimized IMRT plan. With the dosimetric evaluation of 15 NSCLC patients, the hybrid technique has been shown to reduce V_5 , V_{10} , V_{30} ,

and the mean lung dose (MLD) of normal lungs compared with VMAT and better protect the organs-at-risk (OARs) with fewer monitor units (MUs) at the cost of slightly higher dosimetric indexes as compared to IMRT. The proposed hybrid approach demonstrated its promise in improving the treatment outcome and reducing normal tissue toxicity in the radiotherapy of lung cancers, which is one of the most deadly cancers in the modern era.

The clinical study entitled “Volumetric Modulated Arc Therapy of the Pelvic Lymph Nodes to the Aortic Bifurcation in Higher Risk Prostate Cancer: Early Toxicity Outcomes” addressed a controversial issue in the clinic, the treatment of pelvic lymph nodes (PLNs) in higher risk prostate carcinoma, by evaluating the early toxicity profile for this cohort of patients treated with VMAT. In this study, 113 patients treated with VMAT were enrolled with a median follow-up of 14 months. Acute and late genitourinary (GU) and gastrointestinal (GI) toxicities were documented as per the Radiation Therapy Oncology Group (RTOG) guidelines. Their study indicated that VMAT can be utilized efficaciously in a variety of indications to manage carcinoma of the prostate, especially in the high risk prostate cancer where pelvic lymph node volumes can be included up to the aortic bifurcation. This study clearly demonstrated that VMAT was a favorable treatment option in both the definitive and salvage settings in terms of reducing acute toxicity in GU and GI, which can lead to a better quality of life for patients with higher risk prostate cancer.

Another clinical investigation entitled “Replanning Criteria and Timing Definition for Parotid Protection-Based Adaptive Radiation Therapy in Nasopharyngeal Carcinoma” explored a clinically relevant and important issue, that is, the criteria and timing points of replanning for adaptive radiation therapy of nasopharyngeal carcinoma (NPC). Based on 50 NPC patients who were treated with helical tomotherapy, they evaluated the changes of volumetric and dosimetric indexes (D_{mean} , V_1 , and D_{50}) of the parotid glands at various fractional points. Their study indicated that initial parotid volume, initial parotid D_{mean} , and weight loss rate were the most significant indicators for the parotid protection-based replanning in the adaptive radiotherapy of NPC. They further suggested three cutoff values which could be used to predict the timing for replanning in order to better protect the parotid glands during radiotherapy. This interesting clinical study emphasized the importance of patient safety and normal tissue sparing in order to improve the treatment outcome and quality of life of cancer patients.

Another research paper entitled “3D-2D Deformable Image Registration Using Feature-Based Nonuniform Meshes” proposed a novel feature-based nonuniform meshing method to efficiently register 3D images such as CTs with a small portion of 2D projection images of cone-beam CT in image-guided radiotherapy of cancers. In this work, they evaluated and compared the new 3D-2D deformable image registration (DIR) algorithm with other 3D-2D DIR methods in terms of image visualization and quantitative evaluations with two XCAT phantoms and five head and neck cancer patients. Compared with the traditional voxel-based DIR method, the proposed algorithm demonstrated faster computational speed and higher quality of reconstructed images. This technique could be used for accurate deformable image registration and fast adaptive radiotherapy replanning for better tumor control.

Finally, the review article entitled “Combining Whole-Brain Radiotherapy with Gefitinib/Erlotinib for Brain Metastases from Non-Small-Cell Lung Cancer: A Meta-Analysis” conducted systematic review and meta-analysis on the efficacy and safety of whole-brain radiotherapy (WBRT) combined with gefitinib/erlotinib for treatment of brain metastases (BM) from non-small cell lung cancer (NSCLC). Through an extensive literature search, a total of 7 case-controlled and randomized controlled trials involving 622 patients were included in this retrospective study. Statistical analyses indicated that WBRT plus gefitinib/erlotinib can significantly improve the response rate, the remission rate of the central nervous system, the disease control rate, the overall survival, and the one-year survival rate in patients with BM from NSCLC, as compared to WBRT alone or WBRT plus chemotherapy.

In general, this special issue presents a snapshot of what is being actively pursued currently in cancer radiotherapy. In addition to the technological developments featured in this special issue, there have been numerous exciting developments on a variety of topics, such as advanced imaging for treatment response assessment, advanced tumor tracking and monitoring, online quality assurance of treatment delivery, advanced algorithms for real-time monitoring of patient

safety, biologically guided radiation therapy, and electronic health record data mining for more efficient radiotherapy. The successful implementation of these novel technologies into routine clinical workflow will undoubtedly improve patient safety and treatment outcome in the radiotherapeutic management of cancers and usher in a new paradigm for a more personalized radiation therapy.

Jun Deng
Yuanming Feng
Charlie Ma
Fang-Fang Yin

References

- [1] R. Siegel, D. Naishadham, and A. Jemal, “Cancer statistics, 2013,” *CA Cancer Journal for Clinicians*, vol. 63, no. 1, pp. 11–30, 2013.
- [2] M. E. Porter, “What is value in health care?” *The New England Journal of Medicine*, vol. 363, no. 26, pp. 2477–2481, 2010.

Research Article

3D-2D Deformable Image Registration Using Feature-Based Nonuniform Meshes

Zichun Zhong,^{1,2} Xiaohu Guo,¹ Yiqi Cai,¹ Yin Yang,³ Jing Wang,²
Xun Jia,² and Weihua Mao²

¹University of Texas at Dallas, Richardson, TX 75080, USA

²University of Texas Southwestern Medical Center, Dallas, TX 75235, USA

³University of New Mexico, Albuquerque, NM 87131, USA

Correspondence should be addressed to Weihua Mao; weihuamao@gmail.com

Received 11 September 2015; Accepted 28 December 2015

Academic Editor: Cristiana Corsi

Copyright © 2016 Zichun Zhong et al. This is an open access article distributed under the Creative Commons Attribution License, which permits unrestricted use, distribution, and reproduction in any medium, provided the original work is properly cited.

By using prior information of planning CT images and feature-based nonuniform meshes, this paper demonstrates that volumetric images can be efficiently registered with a very small portion of 2D projection images of a Cone-Beam Computed Tomography (CBCT) scan. After a density field is computed based on the extracted feature edges from planning CT images, nonuniform tetrahedral meshes will be automatically generated to better characterize the image features according to the density field; that is, finer meshes are generated for features. The displacement vector fields (DVF) are specified at the mesh vertices to drive the deformation of original CT images. Digitally reconstructed radiographs (DRRs) of the deformed anatomy are generated and compared with corresponding 2D projections. DVFs are optimized to minimize the objective function including differences between DRRs and projections and the regularity. To further accelerate the above 3D-2D registration, a procedure to obtain good initial deformations by deforming the volume surface to match 2D body boundary on projections has been developed. This complete method is evaluated quantitatively by using several digital phantoms and data from head and neck cancer patients. The feature-based nonuniform meshing method leads to better results than either uniform orthogonal grid or uniform tetrahedral meshes.

1. Introduction

Cone-Beam Computed Tomography (CBCT) has been widely used for accurate patient setup (initial positioning) and adaptive radiation therapy. Attentions are still needed to reduce imaging radiation doses and improve image qualities. Traditionally, Conventional Cone-Beam Computed Tomography (CBCT) image reconstruction in radiation therapy needs hundreds of projections, which deliver high imaging dose to patients. In order to reduce the number of CBCT projections, recently, some researchers have proposed methods to reconstruct images by using the information of prior images, such as a planning CT [1–3] or a previous CBCT [4], and a deformation model, which is essentially a 3D-2D deformable image registration (DIR) procedure. A lot of researches have been done related to 3D-2D image registration. Previously, only rigid registrations between 3D images

and 2D fluoroscopic images have been addressed [5–7]. For 3D-2D nonrigid registration [1, 2, 4, 8, 9], the multiscale technique was applied, instead of using the finite element method- (FEM-) based methods to speed up the reconstruction process and increase the accuracy. For nonrigid modeling of respiratory motion, Zeng et al. [10] introduced a method to estimate the 3D motion parameters of a nonrigid, free breathing motion model from a set of projection views. In order to improve the computational efficiency, Jia et al. [11] developed a GPU-based algorithm to reconstruct high-quality CBCT images from undersampled and noisy projection data so as to lower the imaging dose, but it does not make use of the planning CT. However, in all these methods, voxel-based deformation fields were employed to estimate a large number of unknowns, which required extremely long computational time. Additionally, in their deformation models, the image features and organ boundaries were not

specifically considered, which may cause inaccurate deformation estimation. In this work, we proposed a new FEM-based approach, that is, a feature-based nonuniform meshing method, to overcome these limitations.

FEM can be best understood from its practical application, for instance, mesh discretization of a continuous domain into a set of discrete subdomains. It has already been used in image registration [12, 13]. Usually, FEM is exploited to achieve two important advantageous aspects. On one hand, it endows the efficiency of the registration process due to a small number of sampling points compared with voxel-based sampling methods. On the other hand, it provides the smoothness of the displacement vector field (DVF) due to the smoothness constraint between elements and the interpolation within one element. The quality of geometric discretization is crucial for the effectiveness of the image registration applications. Surface meshing methods in 3D-3D image registration [13–15] and volume meshing methods in 3D-3D image registration [16–19] and in 3D image reconstruction [20, 21] have been applied, but none of them were employed in 3D-2D DIR.

When 3D-2D DIR algorithm is used iteratively to reconstruct 3D volumetric images, the number of sampling points is crucial for the computation. A large number of sampling points could lead to a very slow computational speed, while a limited number of points with uniform distribution could miss some important image features and make the registration less accurate. In our proposed method, a special FEM system is developed to automatically generate high-quality adaptive meshes conforming to the image features for the whole volume without user's manual segmentation. This system allows for more sampling points placed in important regions (at organ/tissue/body boundaries or regions with highly nonlinearly varying image intensity); while fewer sampling points are placed within homogeneous or in regions with linearly varying intensity. In this way, deformations of boundaries and other important features can be directly characterized by the displacements of the sampling points that are lying on boundaries or features, rather than interpolating from a uniform grid or a larger-sized tetrahedron in the volume mesh. As a result, the deformation can be controlled more precisely. With approximately the same numbers of sampling points, the feature-based nonuniform meshing method produces better deformed volumetric images comparing with methods using uniform meshes. The high-quality digitally reconstructed radiographs (DRRs) of the deformed anatomy are generated by using ray tracing method. Subsequently, these DRRs are compared with corresponding 2D projections from CBCT scans, and the DVF is optimized iteratively to obtain the final reconstructed volumetric images.

In order to provide a good initial DVF and accelerate the calculation, we proposed a boundary-based 3D-2D DIR method before the aforementioned 3D-2D DIR. Although researches on boundary-guided (or contour-guided) image registrations [22–24] have been carried out for many years, their methods were applied on either 2D-2D or 3D-3D DIR cases. Our proposed algorithm is suitable to employ on 3D-2D DIR, while dealing with large deformations for adaptive radiation therapy.

This paper makes the following contributions for effectively computing 3D-2D DIR:

- (i) Compared with the traditional voxel-based method, the mesh-based methods have faster computational speed and better DVFs, since the voxel-based deformations were employed to estimate a large number of unknowns, which required extremely long computational time and were easy to be trapped in localized deformations.
- (ii) When equal numbers of sampling points are used, the nonuniform meshing method leads to obtaining higher quality reconstructed images and better DVF compared with that of uniform meshes under the same number of optimization iterations.
- (iii) Due to the large data sizes of the volume and projection images, the boundary-based DIR technique and GPU-based parallel implementation have been applied and achieved high computational efficiency and the reconstruction of $512 \times 512 \times 140$ CBCT image can be done within 3 minutes, which is close to clinical applications.

The rest of the paper is organized as follows. Section 2 describes the proposed methods and materials in detail, including nonuniform mesh generation, the framework of the nonuniform meshing to reconstruct volumetric images by using 3D-2D DIR, and the boundary-based 3D-2D DIR. In Section 3, the experimental results are discussed to evaluate the proposed methods qualitatively and quantitatively. Several digital phantoms and patient data sets are measured. Finally, the conclusion and future work are given in Section 4.

2. Methods and Materials

Figure 1 illustrates a flow chart of the entire proposed technique. The dash-line box is used to provide initial DVFs and accelerate the calculation by proposed boundary-based 3D-2D DIR method, which will be described in Section 2.3. All other parts illustrate how the proposed novel nonuniform-mesh-guided 3D-2D image registration method is used to deform the original planning CT images. This requires much smaller degrees of freedom to generate the DVF than that of voxel-based methods. Each step is described in the following subsections and we will firstly introduce the nonuniform-mesh-guided 3D-2D image registration method and then discuss the boundary-based 3D-2D DIR method.

2.1. Creation of Nonuniform Meshes. After the user specifies the total number of mesh vertices, a feature-based nonuniform tetrahedral mesh is generated automatically. Nonuniform meshes are important for improving the accuracy of the numerical simulations as well as better approximating the shapes. Zhong et al. [25] developed a novel particle-based nonuniform surface meshing approach by formulating the interparticle energy optimization in a fast convergence technique. In this method, users will design a density field, which is used to control the distribution of the particles (sampling points). This particle-based surface meshing framework is

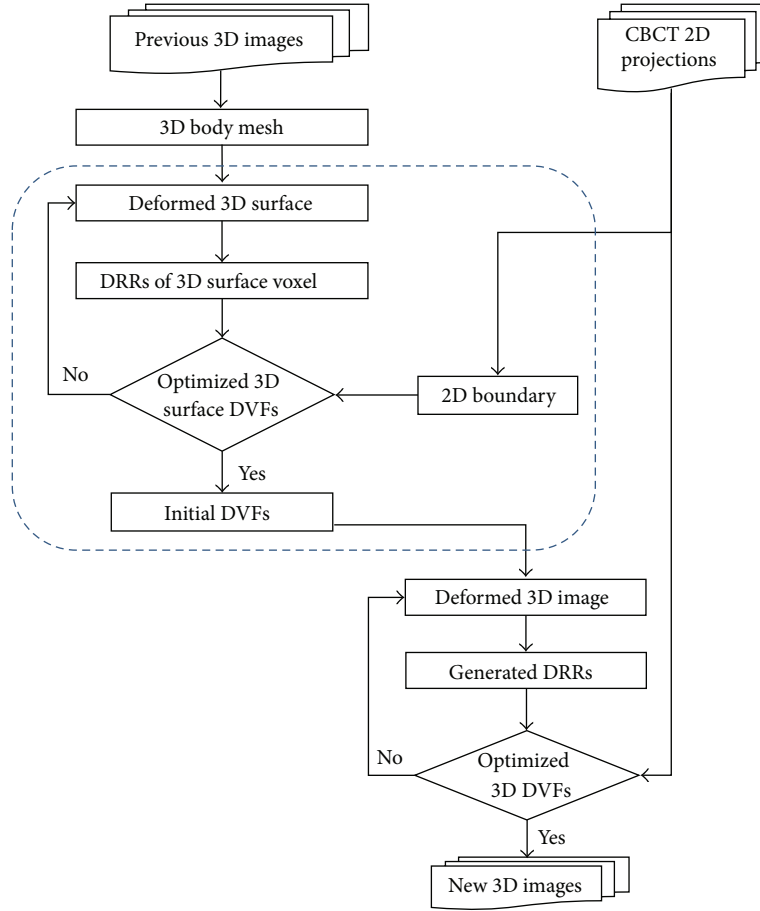


FIGURE 1: Flow chart of the proposed 3D-2D image registration method. The dash-line box is used to provide initial DVFs and accelerate the calculation by proposed boundary-based 3D-2D DIR method. It may be skipped according to different scenarios. More details are given in Section 2.3.

extended to 3D volume case in this paper so as to generate tetrahedral meshes based on 3D volume images.

2.1.1. Basic Meshing Framework. The basic idea of the mesh generation is similar to Zhong et al.'s work [25], and the main difference is that we extend their work to 3D nonuniform volume meshing. There are two steps in mesh generation: particle optimization and Delaunay triangulation computation.

Regarding each mesh vertex as a particle, the potential energy between the particles decides the interparticle forces. When the forces on each particle reach equilibrium, particles arrive at an optimal balanced state, resulting in a uniform distribution. In this case, an isotropic meshing can be generated. To handle the adaptive meshing, the concept of “embedding space” [26, 27] is applied. In the Nash embedding theorem, it is stated that every Riemannian manifold [28] can be isometrically embedded into some high-dimensional Euclidean space. In such high-dimensional embedding space, the metric is uniform and isotropic. When the forces applied on each particle become equilibrial in this embedding space, the particle distribution in the original domain will exhibit the desired adaptive property, that is, conforming to

the user-defined density field. This property is used to formulate the particle-based adaptive meshing framework. The following concepts of density field, interparticle energy, and force are defined based on [25].

The density field is defined by using the following metric tensor as

$$\mathbf{M}(\mathbf{v}) = \rho(\mathbf{v})^{2/m} \cdot \mathbf{I}, \quad (1)$$

where \mathbf{v} is the particle position. \mathbf{I} is the 3×3 identity matrix. $\mathbf{M}(\mathbf{v})$ defines an isotropic adaptive metric with the user-defined density function $\rho(\mathbf{v})$. m is the dimension of the original volume space, so $m = 3$.

Given N_v particles with their positions $\mathbf{V} = \{\mathbf{v}_i \mid i = 1 \cdots N_v\}$ in the volume Ω ($\Omega \in \mathbb{R}^m$) which is embedded in $\mathbf{R}^{\bar{m}}$ space, denoted as $\bar{\mathbf{V}} = \{\bar{\mathbf{v}}_i \mid i = 1 \cdots N_v\}$, where $m \leq \bar{m}$, the interparticle energy between particles i and j in such embedding space is defined as

$$\bar{E}^{ij} = e^{-\|\bar{\mathbf{v}}_i - \bar{\mathbf{v}}_j\|^2 / 4\sigma^2} = e^{-\langle \mathbf{v}_i - \mathbf{v}_j \rangle^T \mathbf{M}_{ij} (\mathbf{v}_i - \mathbf{v}_j) / 4\sigma^2}, \quad (2)$$

where \mathbf{M}_{ij} is the metric tensor between particles i and j , and, for simplicity, it is approximated by the average of metric tensors at two positions: $\mathbf{M}_{ij} \approx (\mathbf{M}(\mathbf{v}_i) + \mathbf{M}(\mathbf{v}_j)) / 2$.

Data: a 3D volume Ω with density field $\rho(\mathbf{v})$, and the desired number of vertices N_v
Result: an adaptive sampling \mathbf{V} of Ω
Initialize particle locations \mathbf{V} ;
While *stopping condition not satisfied* **do**
 Update the k - d tree [22] data structure for the current sampling locations \mathbf{V} ;
 for each particle i **do**
 Obtain particle i 's k -nearest neighbors $N(i)$ within five standard deviations (5σ) from k - d tree;
 for each particle $j \in N(i)$ **do**
 Compute \bar{E}^{ij} by (2);
 Compute $\bar{\mathbf{F}}^{ij}$ by (4);
 end
 Compute the total force $\bar{\mathbf{F}}^i$ by (5);
 end
 Compute the total energy \bar{E} by (3);
 Run L-BFGS algorithm with \bar{E} and $\{\bar{\mathbf{F}}^i\}$, to update the particle locations \mathbf{V} ;
 Project \mathbf{V} onto the 3D volume surface, if \mathbf{V} jumps out of the volume boundary;
end

ALGORITHM 1: Particle optimization with density field $\rho(\mathbf{v})$.

The exponent in the term \bar{E}^{ij} can be approximated by $\|\bar{\mathbf{v}}_i - \bar{\mathbf{v}}_j\|^2 \approx (\mathbf{v}_i - \mathbf{v}_j)^T \mathbf{M}_{ij} (\mathbf{v}_i - \mathbf{v}_j)$. The interparticle energy as defined in (2) depends on how to choose the fixed kernel width σ . If σ is chosen too small, then particles will nearly stop spreading because there are almost no forces between particles. If σ is chosen too large, then nearby particles cannot repel each other and the resulting sampling distribution will be poor. From our extensive experiments, we find out that the best adaptive mesh quality can be achieved when Gaussian kernel width is set as $\sigma = 0.3\sqrt{|\bar{\Omega}|/N_v}$. $|\bar{\Omega}|$ is the image volume in the embedding space.

The total energy can be computed by summing up all pairs of interparticle energies:

$$\bar{E} = \sum_{i=1}^{N_v} \sum_{j=1, j \neq i}^{N_v} \bar{E}^{ij}. \quad (3)$$

The gradient of \bar{E}^{ij} can be considered as the *force* $\bar{\mathbf{F}}^{ij}$ in the embedding space:

$$\begin{aligned} \bar{\mathbf{F}}^{ij} &= \frac{\partial \bar{E}^{ij}}{\partial \bar{\mathbf{v}}_j} = \frac{(\bar{\mathbf{v}}_i - \bar{\mathbf{v}}_j)}{2\sigma^2} e^{-\|\bar{\mathbf{v}}_i - \bar{\mathbf{v}}_j\|^2/4\sigma^2} \\ &= \frac{\mathbf{Q}_{ij} (\mathbf{v}_i - \mathbf{v}_j)}{2\sigma^2} e^{-(\mathbf{v}_i - \mathbf{v}_j)^T \mathbf{M}_{ij} (\mathbf{v}_i - \mathbf{v}_j)/4\sigma^2}, \end{aligned} \quad (4)$$

where $\mathbf{Q}_{ij} = \sqrt{\mathbf{M}_{ij}}$. The details of the mathematical derivations are given in Sec. 3.2.2 of [25].

Then the total force applied on particle i is

$$\bar{\mathbf{F}}^i = \sum_{j \neq i} \bar{\mathbf{F}}^{ij}. \quad (5)$$

In the particle optimization algorithm, user can specify a density field $\rho(\mathbf{v})$ and desired number of vertices N_v . In

our implementation, for each particle, we only compute the mutual effects (i.e., energy and forces) from the particles within a neighborhood of five standard deviations (5σ); otherwise, the particles have no mutual effects due to the large distance between each other. The k - d tree [29] is a space-partitioning data structure for organizing points in a k -dimensional space and can quickly search such neighborhoods. With the total interparticle energy (3) and force (5), L-BFGS [30] (a quasi-Newton algorithm) optimization method is used to obtain the optimized adaptive particle positions. This optimization proceeds iteratively until convergence by satisfying a specified stopping condition; for example, the magnitude of the gradient or the maximal displacement of particles is smaller than a threshold, or the total number of iterations. Algorithm 1 shows the details of the adaptive particle optimization on 3D volume.

After optimizing the particle positions, the final desired nonuniform tetrahedral mesh can be generated by using the Delaunay triangulation [29]. If the density field is uniform in the entire volume, we can generate the isotropic tetrahedron mesh, which is used in Section 3 for comparison experiments.

2.1.2. Feature-Based Nonuniform Meshing on Medical Image.

Figure 2 illustrates the feature-based nonuniform mesh generation on a set of torso images acquired from a digital phantom XCAT [31]. The 4D XCAT provides an accurate representation of complex human anatomy and has the advantage that its organ shapes can be changed to realistically model anatomical variations and patient motions; more importantly, it also provides voxel-based DVFs, which are used as the ground truths to evaluate the accuracy of the deformation.

It is necessary to design a density field to match the volume image features. Original images are preanalyzed using a Laplacian operator (searching for zero crossings in the second

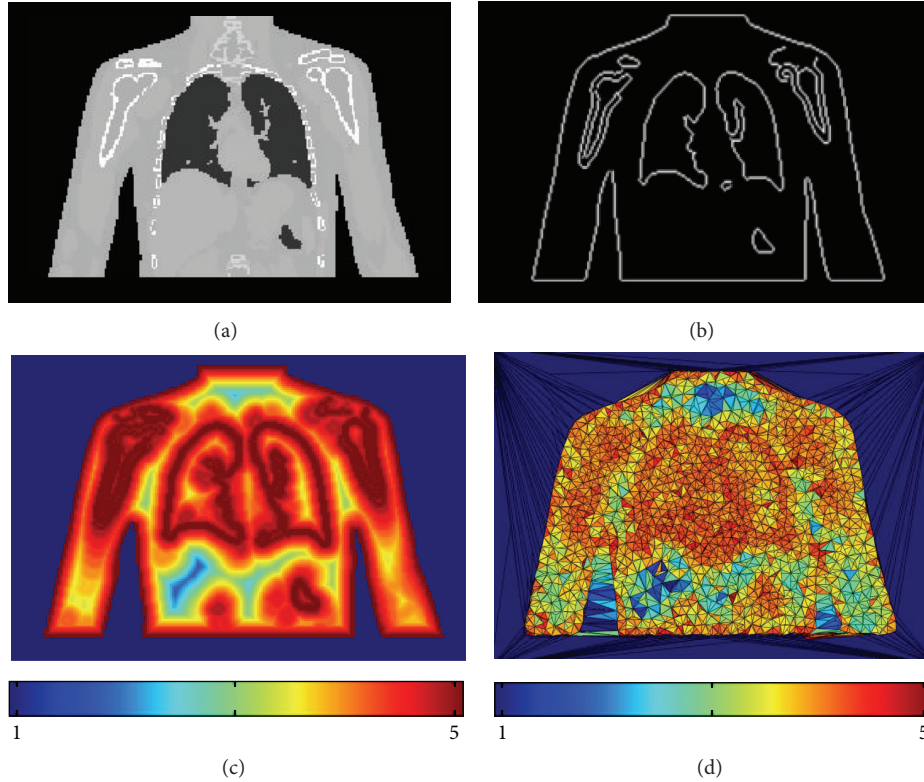


FIGURE 2: Demonstration of the feature-based nonuniform mesh generation on a digital XCAT phantom. (a) The original image; (b) extracted feature edges; (c) density field; (d) a 2D view of the interior meshes with color-mapping.

derivative of the image to find edges) to extract features including contour edges and boundaries between organs and tissues, which are regions with highly nonlinearly varying image intensities. Since the Laplacian operator as high-pass operator highlights edges as well as noise, it is desirable to smooth the image in order to suppress noises at first. When the feature edges of the volume image are obtained as shown in Figure 2(b), a density field could be calculated automatically without manual segmentation (Figure 2(c)). The density function $\rho(\mathbf{v})^{1/3}$ depends on the distance between the feature edges and the voxels in the volume domain. In our experiments, the smooth density field is defined as a piecewise linear function:

$$\rho(\mathbf{v})^{1/3} = \begin{cases} 5, & 0 \leq \varphi \leq 2, \\ \frac{49}{9} - \frac{2}{9}\varphi, & 2 < \varphi \leq 20, \\ 1, & \text{otherwise,} \end{cases} \quad (6)$$

where φ is the distance between the feature edges and the voxels measured by the voxel grid unit. The red color means the higher density field area, while the blue color means the lower density field area. The user can choose any other density functions according to their requirement. The motivation of designing the density field as a piecewise linear function is to make the density field as smooth as possible, so that the volume sizes of the tetrahedrons in the computed mesh can be controlled to vary smoothly. Finally, we can generate adaptive

meshes with high-quality tetrahedral elements. Equation (6) is given under our extensive DIR experiments, which is based on the volume image resolutions and voxel scales: if the sampling point is located within 2-voxel distance with respect to its nearest feature edge point, the density value is 5; if the sampling point is located between 2-voxel and 20-voxel distance with respect to its nearest feature edge point, the density value is computed based on the designed linear function in (6); if the sampling point is located beyond 20-voxel distance with respect to its nearest feature edge point, the density value is 1. From Figure 2, we can see that the designed density field can generate good tetrahedral meshes, which can well conform to the image features as well as obtain high-quality tetrahedral meshes.

After designing the density field, a binary mask needs to be computed from the original image by setting “one” inside of the human anatomy and “zero” outside to constrain the vertex positions inside or on the body during mesh vertices optimization. The mesh vertices are automatically computed by Algorithm 1. Vertices are densely positioned in the regions with highly nonlinearly varying image intensities, while regions of constant or linearly varying image intensities are assigned fewer vertices. Following this process, vertex locations are optimized conforming to the density field as illustrated in Figure 2(c). In order to control the entire volume image more effectively, 8 bounding box vertices of the human anatomy are added (as shown in Figure 3). Then volume meshes (tetrahedrons) are created based on the Delaunay

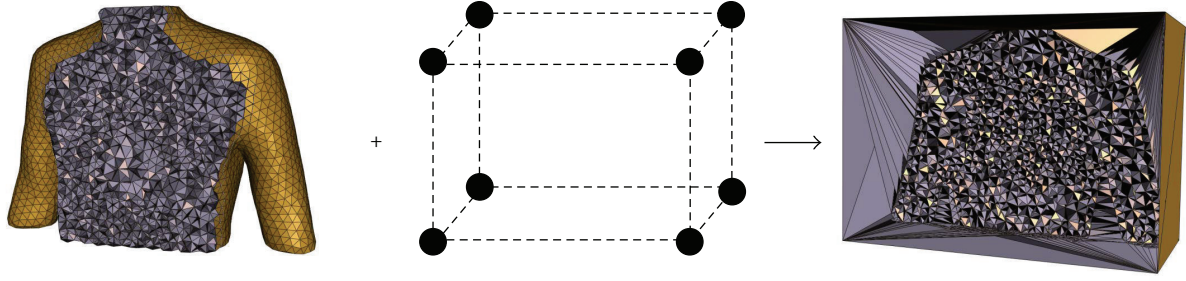


FIGURE 3: In order to control the entire volume image more effectively, 8 bounding box vertices of the human anatomy are added.

triangulation of the vertices. As a result, meshes corresponding to boundaries between organs and tissues are denser. The color-coded tetrahedrons of the generated feature-based mesh in Figure 2(d) illustrate that the tetrahedral volumes are well conforming to the desired density defined by the features of the given image. Due to the importance of deformations occurring around boundaries between organs and tissues, it is necessary to place more vertices (or sampling points) at features, while placing fewer vertices in nonfeature regions. In this way, if DVF is specified to each mesh vertex (or sampling point), the boundaries and other important features can be directly represented by the displacements of sampling points or represented by smaller tetrahedrons, rather than interpolating through four vertices of one larger-sized tetrahedron; then the deformation can be diffused from the mesh vertices to each voxel of the volume more accurately. This is the most significant advantage of the feature-based nonuniform meshing method.

2.2. Volumetric Image Reconstruction by 3D-2D DIR. This section introduces how to use our generated feature-based nonuniform meshing to reconstruct high-quality volumetric images by using 3D-2D DIR.

2.2.1. Computation of Deformed Volume. The displacement vector of each voxel (\mathbf{D}^v) is obtained through interpolating the DVF on mesh vertices (\mathbf{D}) by using the barycentric coordinates [32] of each voxel in its corresponding tetrahedron, and the deformed volume is resampled onto a uniform grid volume. The intensity of each voxel in the new deformed image U_{new} is calculated from the original CT image U_{original} according to \mathbf{D}^v as follows:

$$U_{\text{new}}(a, b, c) = U_{\text{original}}(a + D_1^v(a, b, c), b + D_2^v(a, b, c), c + D_3^v(a, b, c)), \quad (7)$$

where D_1^v , D_2^v , and D_3^v are three floating point spatial components of the displacement vector (\mathbf{D}^v) along x , y , and z directions. The displacement vector points from the center of voxel (a, b, c) in the new deformed image to a point at $(a + D_1^v(a, b, c), b + D_2^v(a, b, c), c + D_3^v(a, b, c))$ in the original source image that will unlikely be at a voxel center. Then the original source intensity at that point is obtained via trilinear interpolation from its eight neighboring voxels.

This technique not only gives an accurate CT intensity to map to the new deformed image, but also acts as an antialiasing technique to avoid artifacts in the projected DRRs, since it is easy and efficient to compute DRRs from a uniform grid sampled volume by using ray tracing algorithm.

2.2.2. Computation of DRR Using Ray Tracing Algorithm. Ray tracing is a technique for generating an image by tracing the path of light through pixels in an image plane and simulating the effects of its encounters with objects. In the DRR generation, the Siddon ray tracing algorithm is applied [33].

To better simulate the realistic raw target CBCT projections from XCAT phantom data and test the sensitivity of our method to the realistic complications, after the noise-free ray line integrals p_i are computed, the noisy signal I_i at each pixel i is generated based on the following noise model:

$$I_i = \text{Poisson}(I_0 e^{-p_i}) + \text{Normal}(0, \sigma_e^2), \quad (8)$$

where Poisson is Poisson distribution and Normal is normal distribution. I_0 is the incident X-ray intensity and σ_e^2 is the background electronic noise variance. In this study, I_0 is set to 1×10^5 and σ_e^2 is set to 10 [34, 35].

2.2.3. Optimization of 3D-2D DIR Energy. The deformation is optimized by minimizing the total energy E , which includes two terms, the regularization ($E_{\text{reg}}(\mathbf{D})$) used to achieve smoothness of the DVF and the similarity ($E_{\text{sim}}(\mathbf{D})$) between the two images:

$$E(\mathbf{D}) = E_{\text{reg}}(\mathbf{D}) + E_{\text{sim}}(\mathbf{D}) = \mu L(\mathbf{D}) + \sum_{m=1}^{N_p} \|R(\mathbf{D}, \theta_m) - I(\theta_m)\|^2, \quad (9)$$

where μ is a weighting factor to control the tradeoff between the similarity and regularization. It is empirically set at 10.0 for all of the experiments in this paper. \mathbf{D} is the DVF defined on the mesh vertices. $L(\mathbf{D})$ is regularization term defined as

$$L(\mathbf{D}) = \sum_{i=1}^{N_v} \sum_{d=1}^3 \left[\left(\frac{\sum_{j \in N(i)} (\mathbf{D}_d(j) - \mathbf{D}_d(i))}{|N(i)|} \right)^2 \right], \quad (10)$$

where $L(\mathbf{D})$ is a summation of the square of Graph Laplacian operations [36] on the DVF over every vertex except those on the external borders. \mathbf{D}_d ($d = 1, 2, 3$) are three components of DVFs. N_v is the total number of the mesh vertices. $N(i)$ is the set of one-ring neighboring vertices (j) of vertex i . $|N(i)|$ is the size of set $N(i)$.

The second term of the energy function in (9) represents the similarity between the CBCT projections ($I(\theta_m)$) acquired at gantry angle (θ_m) beforehand and the DRRs ($R(\mathbf{D}, \theta_m)$) created after the deformation of \mathbf{D} applied on planning CT at the same gantry angle. N_p is the number of projections involved. This term is a summation of the square of intensity difference over every pixel of all projections. Although R and I are two-dimensional in reality, we can easily use one-dimensional arrays to represent them for computational simplification.

L-BFGS algorithm [30] is used to optimize the DVF (\mathbf{D}). The gradient of the energy function E with respect to \mathbf{D} can be calculated as follows:

$$\begin{aligned} \nabla E(\mathbf{D}) &= \mu \nabla L(\mathbf{D}) \\ &+ 2 \sum_{m=1}^{N_p} (R(\mathbf{D}, \theta_m) - I(\theta_m)) \nabla R(\mathbf{D}, \theta_m). \end{aligned} \quad (11)$$

For each iteration of L-BFGS optimization, the energy E and its gradient ∇E are updated.

The DRRs ($R(\mathbf{D}, \theta_m)$) are generated from the resampled deformed planning CT (U_{new}) by the ray tracing method for each gantry angle as

$$R(\mathbf{D}, \theta_m) = \mathbf{P}(\theta_m) U_{\text{new}}(\mathbf{D}), \quad (12)$$

where $\mathbf{P}(\theta_m)$ is the cone-beam projection matrix that describes the X-ray projection operations. The element $\omega^{\alpha, \beta}$ of matrix \mathbf{P} is the weight of voxel β in U_{new} contributed to the pixel α in DRR during the projection simulation calculated by the ray tracing method.

Using (12), the gradient of the energy function E of (11) becomes

$$\begin{aligned} \nabla E(\mathbf{D}) &= \mu \nabla L(\mathbf{D}) + 2 \sum_{m=1}^{N_p} \mathbf{P}(\theta_m) \\ &\cdot (\mathbf{P}(\theta_m) U_{\text{new}}(\mathbf{D}) - I(\theta_m)) \nabla U_{\text{new}}(\mathbf{D}). \end{aligned} \quad (13)$$

2.2.4. GPU-Based Acceleration. The entire process of this volumetric image reconstruction method was implemented on GPU. The GPU card used in our experiments is an NVIDIA GeForce GTX 780 Ti with 3 GB GDDR5 video memory. It has 2,880 CUDA cores with a clock speed of 1,006 MHz. Utilizing such a GPU card with tremendous parallel computing ability can significantly increase the computation efficiency. There are two time-consuming processes during the reconstruction. One is the DRR generation, and the other is the gradient computation of the similarity term in the total energy E .

(1) *DRR Generation on GPU.* For the DRR generation part, it is straightforward to accomplish the ray tracing algorithm in parallel computation. For example, each pixel intensity of

the DRR is determined by accumulating all of the weighted voxel intensities through which one X-ray goes. This computation process is highly independent between each ray line. In this case, different GPU threads can compute each ray line simultaneously without conflict.

(2) *Computation of Energy Gradient on GPU.* From (13), it can be seen that there are two terms in the gradient of the energy. One is the gradient of regularization $\mu \nabla L(\mathbf{D})$ with respect to DVF \mathbf{D} : this can be easily computed in parallel based on each mesh vertex. The other is the gradient of the similarity term. In order to demonstrate clearly how to compute this term in parallel, the second part of (13) is rewritten in more detail based on pixel α in DRR and voxel β in U_{new} at one projection in angle (θ_m). The gradient of the similarity term with respect to displacement vector of vertex i (i.e., \mathbf{D}_i) can be denoted as follows:

$$\begin{aligned} \frac{\partial E_{\text{sim}}(\mathbf{D}, \theta_m)}{\partial \mathbf{D}_i} &= 2 \sum_{\beta=1}^{|U_{\text{new}}(\mathbf{D}, i)|} \sum_{\alpha=1}^{|R(\beta)|} \omega^{\alpha, \beta} (R^\alpha - I^\alpha) \nabla U_{\text{new}}^\beta(\mathbf{D}, i), \end{aligned} \quad (14)$$

where $U_{\text{new}}(\mathbf{D}, i)$ is the set of voxels controlled by vertex i . $R(\beta)$ is the set of pixels on DRR affected by voxel β . $|U_{\text{new}}(\mathbf{D}, i)|$ and $|R(\beta)|$ are the sizes of the corresponding sets. R^α is the intensity of pixel α on DRR. I^α is the intensity of pixel α on CBCT projection. $\omega^{\alpha, \beta}$ is one element in the projection matrix $\mathbf{P}(\theta_m)$, that is, the weight of voxel β ($U_{\text{new}}^\beta(\mathbf{D}, i)$) contributed to the pixel α in DRR generation. $\nabla U_{\text{new}}^\beta(\mathbf{D}, i)$ is the gradient of voxel β ($U_{\text{new}}^\beta(\mathbf{D}, i)$) with respect to \mathbf{D}_i .

Then the gradient of the similarity term, that is, (14), can be rewritten by simplification as

$$\frac{\partial E_{\text{sim}}(\mathbf{D}, \theta_m)}{\partial \mathbf{D}_i} = \sum_{\beta=1}^{|U_{\text{new}}(\mathbf{D}, i)|} \frac{\partial E_{\text{sim}}(\mathbf{D}, \theta_m)}{\partial U_{\text{new}}^\beta(\mathbf{D}, i)} \frac{\partial U_{\text{new}}^\beta(\mathbf{D}, i)}{\partial \mathbf{D}_i}. \quad (15)$$

Finally the total gradient for all projections with respect to displacement vector \mathbf{D}_i is

$$\frac{\partial E_{\text{sim}}(\mathbf{D})}{\partial \mathbf{D}_i} = \sum_{m=1}^{N_p} \sum_{\beta=1}^{|U_{\text{new}}(\mathbf{D}, i)|} \frac{\partial E_{\text{sim}}(\mathbf{D}, \theta_m, \beta)}{\partial \mathbf{D}_i}, \quad (16)$$

where N_p is the number of projections.

Now it is clearly shown that there are two components in the gradient of the similarity term in (15).

(a) Gradient computation of the similarity energy with respect to voxel intensity ($\partial E_{\text{sim}}(\mathbf{D}, \theta_m) / \partial U_{\text{new}}^\beta(\mathbf{D}, i)$): this can be computed when the DRRs are generated and then stored in a volume-sized matrix. However, this computation is a little bit complicated for GPU computation. One voxel of the CT image may probably affect a number of pixels on the DRR image during the projection simulation, so that in the gradient computation, it is inevitable to consider it; that is, when mapping back the DRRs to the volume image, there is probably more than one ray line going through one voxel.

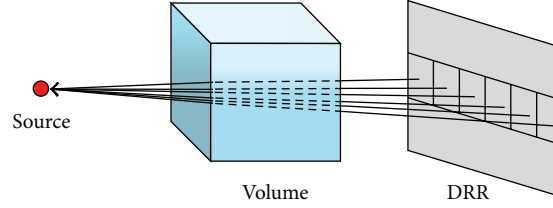


FIGURE 4: Subdividing the DRR image into small subgroups for GPU parallel computation.

If the original ray tracing implementation is directly used to parallelize all ray lines in the gradient computation, there will be a memory conflict within the GPU; that is, the gradient of the similarity energy E_{sim} with respect to one voxel intensity is updated by different ray lines simultaneously. To overcome this problem, the DRR image is subdivided into small subgroups so that the ray lines in different groups cannot go through the same voxel concurrently as shown in Figure 4. Currently, the computation can be computed on each voxel simultaneously by assigning it to each GPU thread. After that the total gradient of the similarity term as (16) is obtained by summing up all the gradient values from different subgroups and projections.

To maximally utilize the GPU's parallel computing power, the best subgroup size for the XCAT data is 8×8 pixels, and the head and neck (H&N) patient data is 16×24 pixels, which is determined during the preprocessing step. The general idea is computed based on similar triangle property according to the voxel scale, the pixel scale, the distance from source to volume position, and the distance from source to DRR position.

(b) Gradient of voxel intensity with respect to displacement vector of vertex i , $(\partial U_{\text{new}}^\beta(\mathbf{D}, i)/\partial \mathbf{D}_i)$: this can be done in parallel based on each mesh vertex when the deformed volume is computed, which is independent of the projection computation.

The CPU-based serial implementation of mesh-based 3D-2D registration method on XCAT data ($256 \times 256 \times 132$) with 60 projections (256×256) takes about 2.5 hours; after using the GPU-based parallel implementation, it takes about 3 minutes, which is about 50 times faster.

2.2.5. A Multiresolution Scheme. The size of H&N patient data used in this study is relatively large. CT volume data size is $512 \times 512 \times 140$ and CBCT projection size is 1024×768 . The reconstruction running time of CPU-based implementation on mesh-based 3D-2D registration method with 30 projections is about 12 hours, while the running time of GPU-based implementation is about 20 minutes, which is about 36 times faster than the CPU-based one. The multiresolution scheme is used to further improve the speed. In the experiment, both the CT volume image and CBCT images are downsampled into different resolution levels (three levels for experiments on H&N patient data), from the coarsest level (CT volume: $256 \times 256 \times 70$, CBCT projection: 256×192 , and time per iteration: 2.08 seconds) to the higher level (CT volume: $512 \times 512 \times 140$, CBCT projection: 512×384 , and time per iteration:

9.91 seconds) and finally to the full resolution level (CT volume: $512 \times 512 \times 140$, CBCT projection: 1024×768 , and time per iteration: 40.44 seconds). By using this strategy, the volumetric image reconstruction can be accomplished in 6.9 minutes, including 30 iterations of coarsest level, 15 iterations of higher level, and 5 iterations of full resolution level (about 60 times faster than CPU-based serial implementation). It is comparable to the fastest iterative CBCT techniques.

2.3. A Boundary-Based 3D-2D DIR. In order to further improve the computational speed of the proposed 3D-2D DIR method, in this section, we introduce a boundary-based 3D-2D DIR as mentioned in Section 2.2, is used to generate the final volumetric images.

2.3.1. Extraction of 3D and 2D Boundaries. After generating the feature-based nonuniform meshes (Section 2.1), both planning CT images and CBCT projections are preprocessed to create binary masks by setting "one" inside of the studied tissue and "zero" outside as shown in Figure 5(b). Then, the 3D tissue surface and CBCT projection boundaries are extracted by Canny edge detector [37] (Figure 5(c)).

2.3.2. Computation of Projections by Splatting Method. In order to directly and conveniently control the updated positions of the deformed anatomy surface voxels, we prefer to use the splatting method [38] to generate projections of 3D surface, instead of using the ray tracing method. This is one main advantage of splatting method. Every voxel's contribution to a projection is mapped directly onto the image plane by a kernel centered on the voxel as shown in Figure 6. This reconstruction kernel is called a "splat" or "footprint":

$$f(x, y) = \sum_{i,j,k} \text{voxel}(i, j, k) \text{kernel}(x, y) \quad (17)$$

$$= \sum_{i,j,k} \text{voxel}(i, j, k) \frac{1}{\sqrt{2\pi}\sigma^2} e^{-((x-s)^2/2\sigma^2 + (y-t)^2/2\sigma^2)},$$

where $f(x, y)$ is the final pixel intensity of the projection image and $\text{voxel}(i, j, k)$ is the intensity of voxel at (i, j, k) position. $\text{kernel}(x, y)$ is the "footprint function" centered at (s, t) . x and y are the Gaussian kernel area within radius 3σ on the projection image. σ is the Gaussian kernel width.

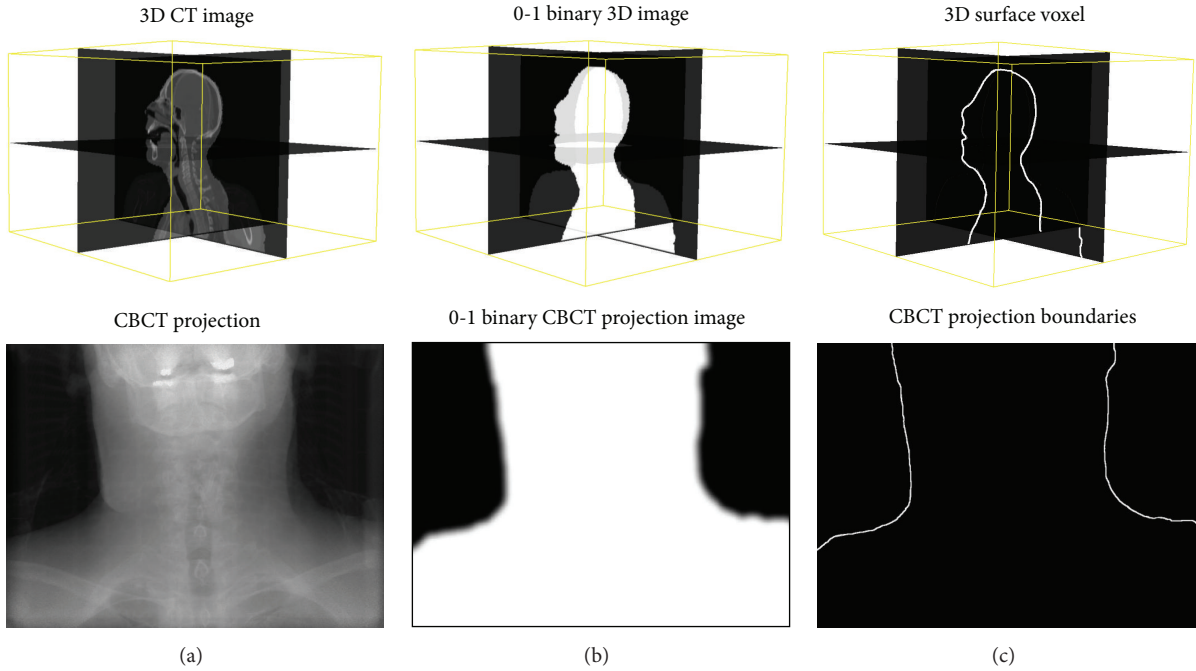


FIGURE 5: (a) Original images; (b) the 0-1 binary images; (c) boundaries of an H&N patient data.

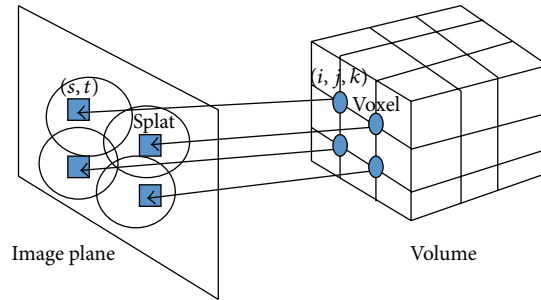


FIGURE 6: Splatting projection.

For perspective projection with antialiasing consideration, the Gaussian kernel radius should have dynamic sizes, which can be calculated from similar triangles shown in Figure 7 and

$$\frac{d1}{d2} = \frac{\text{voxel scale}}{r}, \tag{18}$$

$$\sigma = 0.57r,$$

where $d1$ is the distance from the X-ray source to the voxel center and $d2$ is the distance from the source to kernel center on the image plane going through a specific voxel point. r is the size of splat, and voxel scale is the size of the voxel. The best coefficient value between σ and r is 0.57 based on our extensive experimental results. If the volume is a regular grid, voxel scale is fixed for all the voxels.

Another main advantage of splatting method over ray tracing is that splatting has a faster calculation speed; that is, it is very easy to ignore empty voxels (nonsurface voxels), which

do not contribute to the final projection image. However, this is difficult to realize in ray tracing method.

It is noted that if we directly project the volume surface voxels (without considering kernels) onto the image plane, some pixels may be included there not belonging to the final 2D boundaries of the projection as shown at the top left of Figure 8. At the same time, in order to efficiently control the projection of the surface voxels, we do not use the projection with kernels to compute the boundaries. Instead, there are two projections computed at each gantry angle to extract the final 2D boundaries of the surface voxel projection. One is the projection with voxel kernels (similar to ordinary DRR computation) shown at the top right of Figure 8 and the other is without kernels (directly project each surface voxel onto the image plane) shown at the top left of Figure 8. We have to use the projections with kernels to compute rough DRRs (possibly aliasing exists, but we only care the image boundaries) and then employ it to filter out the exact 2D projection boundaries of the deformed anatomy surface shown at the bottom of Figure 9.

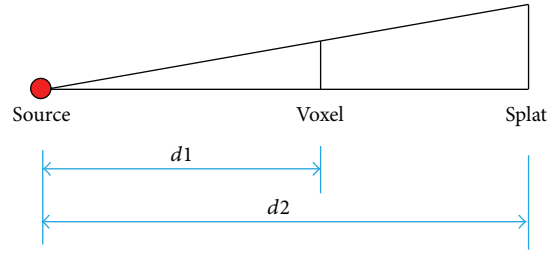


FIGURE 7: Geometry of the perspective projection with antialiasing for splatting method.

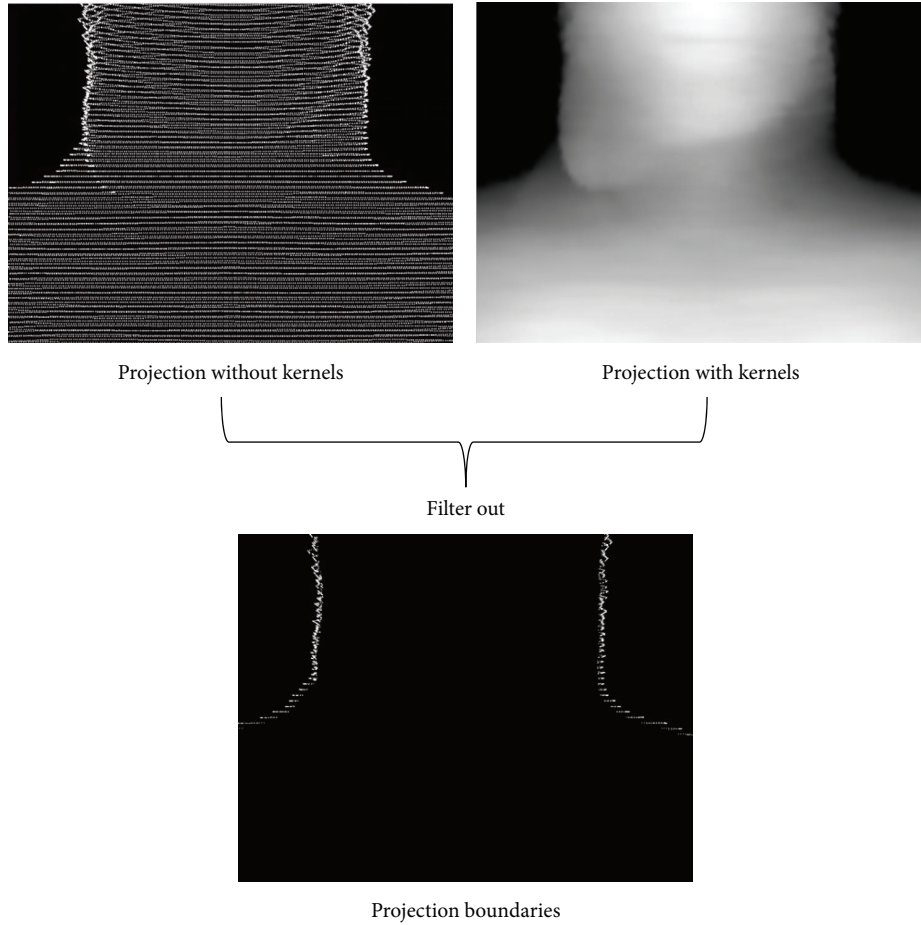


FIGURE 8: Computation of 2D projection boundaries of the deformed anatomy surface from an H&N patient data.

2.3.3. Optimization of Boundary-Based 3D-2D DIR Energy. The computed projections of 3D surface are compared with corresponding 2D projection boundaries from CBCT scans, and the primary DVF is iteratively optimized to obtain a good initial deformation for final volumetric image. The surface deformation is optimized by minimizing the total energy E_{bound} , which includes two terms, the regularization used to achieve smoothness of the DVF and the similarity between the two images that is different from the previous intensity-based formulation. Here, the projections of

the anatomy surface voxel are compared with corresponding 2D projection boundaries from CBCT scans:

$$\begin{aligned}
 E_{\text{bound}} &= \mu L(\mathbf{D}) \\
 &+ \sum_{m=1}^{N_p} \|\text{dist}_{\min}(R_{\text{bound}}(\mathbf{D}, \theta_m), I_{\text{bound}}(\theta_m))\|^2,
 \end{aligned} \tag{19}$$

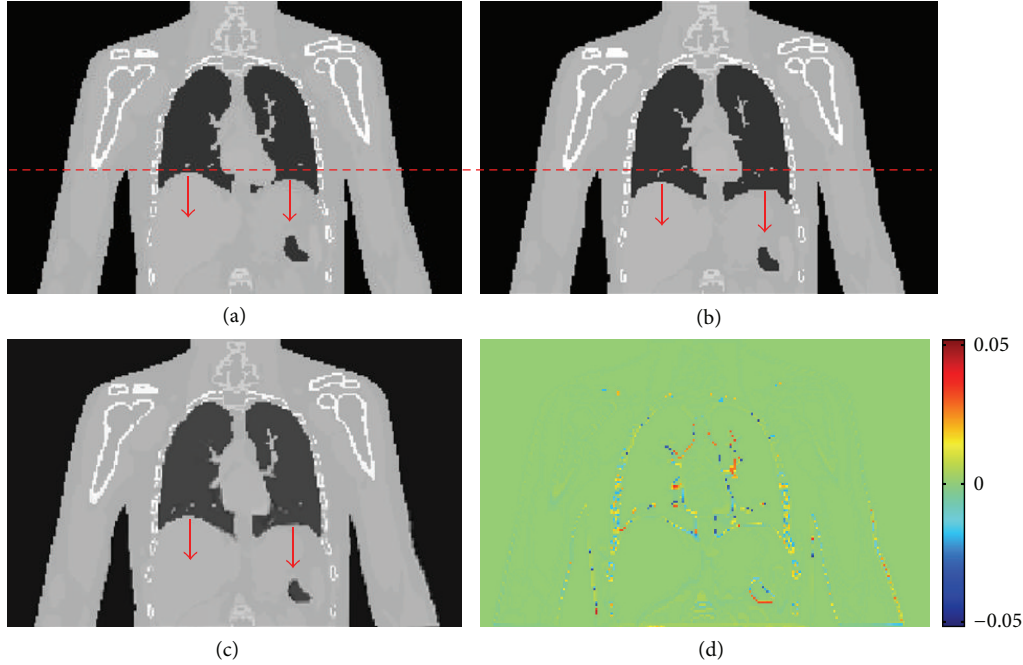


FIGURE 9: Demonstration of XCAT male phantom results. (a) Original image (Phase 1); (b) target image (Phase 4); (c) deformed image from Phase 1; (d) differences between deformed and target images.

where μ is a weighting factor and empirically set at 10.0 for the experiments. \mathbf{D} is the DVF defined on the mesh vertices. $L(\mathbf{D})$ is regularization term defined as in (10). The second term of the energy function indicates the similarity between the CBCT projections boundaries $I_{\text{bound}}(\theta_m)$ acquired at gantry angle θ_m beforehand and the projections $R_{\text{bound}}(\mathbf{D}, \theta_m)$ created after the deformation of \mathbf{D} applied on planning CT body surface at the same gantry angle. N_p is the number of projections involved. This term is a summation of the square of the shortest Euclidean distance between every pixel on projections of the deformed CT surface and the corresponding CBCT projection boundaries. k - d tree data structure is applied to efficiently search such nearest pixels for boundaries [38].

L-BFGS algorithm is used to optimize the DVF (\mathbf{D}). The gradient of the energy function E_{bound} with respect to \mathbf{D} can be calculated as follows:

$$\begin{aligned} \nabla E_{\text{bound}} &= \mu \nabla L(\mathbf{D}) \\ &+ 2 \sum_{m=1}^{N_p} \text{dist}_{\min}(R_{\text{bound}}(\mathbf{D}, \theta_m), I_{\text{bound}}(\theta_m)) \quad (20) \\ \nabla \text{dist}_{\min}(R_{\text{bound}}(\mathbf{D}, \theta_m), I_{\text{bound}}(\theta_m)). \end{aligned}$$

$\nabla \text{dist}_{\min}(R_{\text{bound}}(\mathbf{D}, \theta_m), I_{\text{bound}}(\theta_m))$ can be computed numerically by finite difference with a small $\Delta \mathbf{D}$.

Because we do not need the exact DRRs of the deformed 3D anatomy image, the resampling is not required. What we focus on is the updated voxel positions of the deformed 3D anatomy surface. Then we can use the splatting method to compute the projections of the deformed volume surface.

After the above boundary-based registration, the primary DVF is obtained and then applied in further complete intensity-based DIR as the initial deformation. As a result, the final volumetric images are obtained by applying the optimized DVF to planning CT images.

3. Results

The algorithms are implemented by using Microsoft Visual C++ 2010, MATLAB R2013a, and NVIDIA CUDA 5.5. For the hardware platform, the experiments are run on a desktop computer with Intel® Xeon E5645 CPU with 2.40 GHz, 34 GB DDR3 RAM, and NVIDIA GeForce GTX 780 Ti GPU with 3 GB GDDR5 video memory.

We evaluate and compare our proposed nonuniform tetrahedral meshing for 3D-2D DIR with other 3D-2D DIR methods, that is, voxel-based method [1–3], uniform orthogonal grid mesh [16], and uniform tetrahedral mesh on image visualization and quantitative evaluations on two XCAT phantoms and five H&N cancer patients.

3.1. Evaluation. This method is evaluated thoroughly by using two sets of digital XCAT phantoms and H&N patient data. Taking the XCAT male phantom data for example, two sets of 3D images, representing the same patient (phantom) at two different respiratory phases, are created. Both the beating heart and respiratory motions are considered, and in order to simulate the large deformation, the max diaphragm motion is set to 10 cm. Phase 1 and Phase 4 are shown in Figures 9(a) and 9(b). Phase 1 data is used as the original planning CT image, while Phase 4 data represents daily CBCT images.

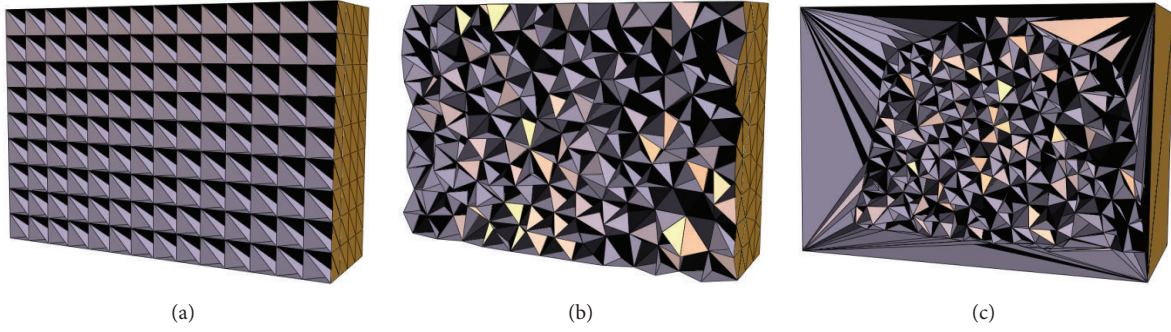


FIGURE 10: Three types of meshing for XCAT male phantom data. (a) A uniform orthogonal grid; (b) a uniform tetrahedron mesh; (c) a feature-based nonuniform tetrahedron mesh.

The deformation vector of every voxel between these two phases is provided by the XCAT software and it is used as the ground truth of DVF for evaluation. A set of DRRs from Phase 4 data is created using a ray tracing method with noise simulation as mentioned in Section 2.2.2 and subsequently used as the raw projections from the daily CBCT. The original CT (Phase 1 data) is deformed to fit the raw projections of daily CBCT and finally a new set of volumetric images is created and compared with the ground truth, Phase 4 data. Simultaneously, the final DVF is compared with the DVF obtained from the XCAT software.

A conventional normalized cross correlation (NCC) is used to evaluate the similarity (i.e., the linear correlation) of 3D images and DVFs:

$$\text{NCC} = \frac{\sum_{i=1}^N [F_{\text{intp}}(i) - \bar{F}_{\text{intp}}] [F(i) - \bar{F}]}{\sqrt{\sum_{i=1}^N [F_{\text{intp}}(i) - \bar{F}_{\text{intp}}]^2} \sqrt{\sum_{i=1}^N [F(i) - \bar{F}]^2}}, \quad (21)$$

where $F_{\text{intp}}(i)$ and $F(i)$ are the interpolated and target values, respectively, over N voxels. \bar{F}_{intp} and \bar{F} are the average values of the interpolated and target values. The range of the NCC is $[-1, 1]$. If NCC is 1, it means two values are exactly the same. The larger the NCC is, the more similar the values are.

The normalized root mean square error (NRMSE) between the interpolated values $F_{\text{intp}}(i)$ and the target values $F(i)$ is also used for comparison of 3D images and DVFs and it denotes the related error:

$$\text{NRMSE} = \sqrt{\frac{\sum_{i=1}^N [F_{\text{intp}}(i) - F(i)]^2}{\sum_{i=1}^N [F(i)]^2}}. \quad (22)$$

The range of the NRMSE is $[0, +\infty)$. If NRMSE is 0, it means two values are exactly the same. The smaller the NRMSE is, the more similar the values are.

To demonstrate the advantage of using feature-based nonuniform mesh, results of three types of meshing methods are compared. These are (1) a bounding box uniform orthogonal grid in Figure 10(a), as mentioned in [9]; (2) a uniform tetrahedron mesh in Figure 10(b); (3) a feature-based nonuniform tetrahedron mesh in Figure 10(c). A voxel-based deformation method is also evaluated.

3.2. Meshing Computation. In order to apply the meshing-based method in the 3D-2D image registration framework, we have to compute the meshes at first. The number of vertices of the tetrahedron meshes in XCAT phantom data and H&N patient data are all around 1,000; hence the execution time of the particle-based meshing method is the same. H&N patient data ($512 \times 512 \times 140$) is larger than XCAT data ($256 \times 256 \times 132$), so it takes more time in the preprocessing steps of image feature edges computation and the density field computation for feature-based tetrahedron mesh generation. Compared with the uniform orthogonal grid mesh generation (5 seconds), the isotropic tetrahedron mesh generation needs 10 seconds, and the feature-based tetrahedron mesh generation needs more time in preprocessing steps: (a) compute the image feature edges: 3.5 seconds (XCAT data) versus 15 seconds (H&N patient data); (b) compute the density field: 0.4 minutes (XCAT data) versus 1.5 minutes (H&N patient data); (c) run particle-based meshing framework: 10 seconds. Uniform and feature-based nonuniform tetrahedron meshes can be generated by our particle-based meshing approach only if the desired density field is available (the density field of uniform tetrahedron mesh is globally uniform). Once these meshes are generated, they are used by the 3D-2D DIR framework, and no additional computation is required for the meshes. It should be noted that the mesh generation could be done in advance as soon as the planning CT is performed. So the time for this preprocess can be hidden for the image registration process.

3.3. XCAT Phantom Data. Feature-based nonuniform tetrahedral meshes are created using approximately 1,000 vertices on the original CT image (Figure 9(a), Phase 1 of the XCAT male model). 60 DRRs are created from the target image (Figure 9(b), Phase 4) at 60 different gantry angles equally spaced over 360 degrees. The new volumetric images are obtained by optimizing the deformation of the meshes by comparing the 60 DRRs of the deformed images with the corresponding projections of the target images in 100 iterations of the elastic registration algorithm. Figure 9(c) shows that the new reconstructed images are very close to the target images. Their differences are illustrated in Figure 9(d), which are very small.

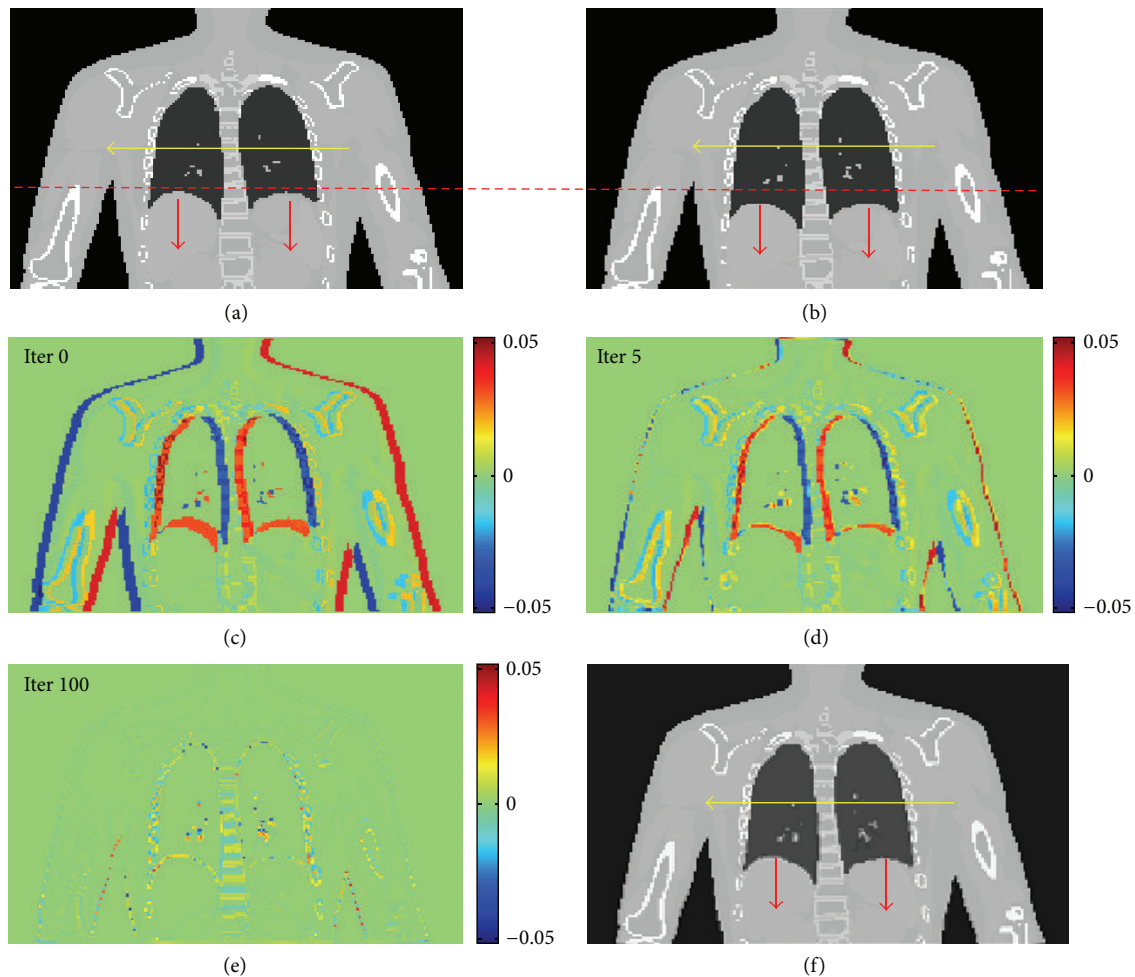


FIGURE 11: Demonstration of XCAT female phantom results. (a) Original image (Phase 1); (b) target image (Phase 4); (c) differences between deformed and target images at the beginning of optimization; (d) differences between deformed and target images at iteration 5; (e) differences between deformed and target images at iteration 100 (end of the optimization); (f) final deformed image from Phase 1.

To test the robustness and accuracy of the algorithm, another XCAT female phantom with more complicated motions including a large deformation between respiratory Phase 1 and Phase 4 and the translation (globally translated by four-voxel-size distance (i.e., about 4.68 mm) in the horizontal direction) is used. Other configurations are the same as the previous male phantom case. Figure 11 shows the intermediate and final results during the optimization process.

While a conventional CBCT reconstruction requires hundreds of projections, the mesh-based algorithm uses far fewer projections since the information from the planning CT image is used. The number of projections may vary from case to case. Table 1 lists the deformation results using varying numbers of projections. A larger number of projections do yield a higher NCC and lower NRMSE, though at the expense of longer calculation time and more radiation dose. A reasonable balance can be observed at 60 projections, as diminishing returns start to take effect by using a larger number of projections.

Comparisons of results from different meshing algorithms are shown in Tables 2 and 3. With regard to the similarity of the final images, the nonuniform mesh provides better results than the uniform orthogonal grid or uniform tetrahedron meshes in 100 optimization iterations, for the approximately same number of vertices. The uniform orthogonal grid mesh is the same as mentioned by Foteinos et al., who pointed out that it has the best registration performance in their experiments [16]. With more vertices, the nonuniform meshing method provides image results very close to the voxel-based method, which has as many vertices as voxels. It shows that the voxel-based deformation may yield good image intensity result, but the resulting DVF represents an unrealistic anatomical mapping. This is a drawback of voxel-based deformation and is due to its localized deformation (i.e., there are too many sampling points and it is easy to be trapped into some local minima). The feature-based nonuniform meshing method overcomes this drawback and yields more anatomically accurate DVF (both the NCC and NRMSE measurements on DVF of the nonuniform meshing

TABLE 1: Digital XCAT male phantom study results using various numbers of projections.

Number of projections used	10	20	30	60	90	120
NCC of images	0.9788	0.9812	0.9825	0.9855	0.9859	0.9860
NRMSE of images	0.1952	0.1836	0.1769	0.1612	0.1587	0.1585
NCC of DVF	0.7823	0.7946	0.8012	0.8150	0.8189	0.8201
NRMSE of DVF	1.0055	0.9076	0.8525	0.8118	0.7959	0.7951

Note. These comparison experiments are run through 100 iterations.

TABLE 2: Evaluation of reconstruction accuracy based on a digital XCAT male phantom.

	Uniform orthogonal grid	Uniform tetrahedron mesh	Nonuniform tetrahedron mesh	Nonuniform tetrahedron mesh	Voxel-based method
Number of vertices	1,050	987	1,005	10,004	8,650,762
NCC of images	0.9829	0.9835	0.9855	0.9858	0.9872
NRMSE of images	0.1749	0.1705	0.1612	0.1593	0.1514
NCC of DVF	0.7690	0.7829	0.8150	0.8265	0.6061
NRMSE of DVF	1.2366	1.0923	0.8118	0.8059	1.2484

Note. The three mesh-based methods are run through 100 iterations, while the voxel-based method needs 200 iterations.

TABLE 3: Evaluation of reconstruction accuracy based on a digital XCAT female phantom.

	Uniform orthogonal grid	Uniform tetrahedron mesh	Nonuniform tetrahedron mesh	Nonuniform tetrahedron mesh	Voxel-based method
Number of vertices	980	981	1,011	10,000	8,650,752
NCC of images	0.9789	0.9792	0.9829	0.9846	0.9775
NRMSE of images	0.1970	0.1954	0.1766	0.1682	0.2035
NCC of DVF	0.7687	0.7680	0.7672	0.7649	0.6292
NRMSE of DVF	1.3875	1.1358	0.9705	0.9777	1.0317

Note. The three mesh-based methods are run through 100 iterations, while the voxel-based method needs 200 iterations.

method are better than those of the voxel-based method, which were applied in [1–3]). Furthermore, from Figure 12, it is clearly seen that the energy curve of the feature-based meshing method (the red line with triangle marker) decreases dramatically faster than any other methods; that is, it has faster convergence speed during the image registration optimization. It is noted that because different meshes or voxel-based methods may have different regularization terms, such as different numbers of displacement vectors, we only compare the similarity term in (9) to make the comparison fair. With the large translation in the XCAT female phantom, the results (in Table 3) of voxel-based method are not as good as the meshed-based methods in both images and DVF measurements, due to its localized deformation and translation.

3.4. *H&N Patient Data.* This feature-based nonuniform meshing image registration method has been tested on five clinical data sets from the head and neck cancer patients H&N01~H&N05. Figure 13 illustrates the density field mapping based on image feature edges and feature-based tetrahedron mesh of H&N01 patient data. Figure 14 shows the deformation results from axial view (a big tumor on the right

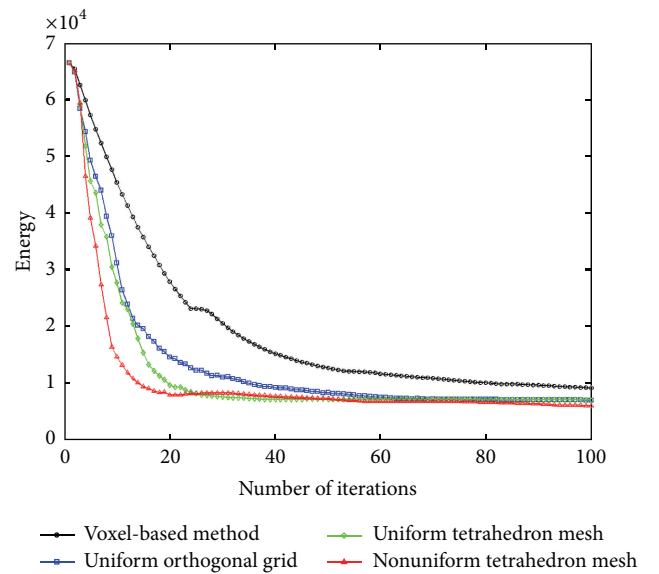


FIGURE 12: The similarity energy ($E_{\text{sim}}(\mathbf{D})$) curves of different methods (voxel-based, uniform orthogonal grid, uniform tetrahedron mesh, and nonuniform tetrahedron mesh) in image registration.

TABLE 4: Results with different numbers of projections on H&N01 patient data.

Number of projections used	10	20	30	60	90
NCC of images	0.8458	0.8459	0.8460	0.8460	0.8460
NRMSE of images	0.4798	0.4794	0.4792	0.4792	0.4792

Note. These comparison experiments are run through 50 iterations.

TABLE 5: Comparison of three meshes on the data of five head and neck cancer patients.

Patients	Uniform orthogonal grid	Uniform tetrahedron mesh	Nonuniform tetrahedron mesh
H&N01			
Number of vertices	936	992	1,007
NCC	0.8327	0.8358	0.8460
NRMSE	0.4988	0.4938	0.4792
H&N02			
Number of vertices	1,040	990	1,000
NCC	0.9036	0.9122	0.9134
NRMSE	0.4182	0.4116	0.4084
H&N03			
Number of vertices	980	1,000	998
NCC	0.8470	0.8471	0.8482
NRMSE	0.4748	0.4743	0.4722
H&N04			
Number of vertices	1,001	1,000	1,000
NCC	0.7756	0.7806	0.8111
NRMSE	0.5841	0.5817	0.5567
H&N05			
Number of vertices	980	1,000	995
NCC	0.7565	0.7690	0.7843
NRMSE	0.6278	0.6092	0.5712

Note. The three mesh-based methods are run through 50 iterations.

TABLE 6: Evaluation of boundary-based DIR accuracy on an H&N cancer patient data.

Status	Initial	Boundary-based DIR	Full DIR
NCC of images	0.7627	0.7875	0.7919
NRMSE of images	0.5938	0.5569	0.5479

side of the patient's chin shrinks) compared with the conventional CBCT reconstruction results of H&N01 patient data. The effects of various numbers of projections are also evaluated and the results are shown in Table 4. The three meshing methods, uniform orthogonal, uniform tetrahedron, and feature-based nonuniform tetrahedron (as shown in Figure 15), are evaluated with results shown in Table 5 for all patient data sets. The nonuniform meshing method again yields the highest accuracy and has faster convergence speed during the image registration. It is noted that, comparing the accuracies in the XCAT phantom data and the H&N patient data, the NRMSE seems larger in the patient cases (~ 0.5) than that in the XCAT cases (< 0.2); this is because, in the patient case, the reconstructed CBCT image is computed based on the planning CT image, and the patient had the planning CT scan and daily CBCT scans on different days and machines, which may cause the differences in the image background, noises, and so forth, resulting in larger NRMSE

values. However, it is acceptable in the image results as shown in Figure 14.

3.5. Boundary-Based 3D-2D DIR Results. For the H&N05 cancer patient data, which has a large deformation on tumor during treatment, we use it to evaluate the effectiveness of the boundary-based 3D-2D DIR method. Figures 16(a) and 16(b) show the original and final differences of one projection boundary in boundary-based DIR. Figure 16(d) demonstrates that the final deformed CT images are very close to the target images (Figure 16(e)) and their differences are very small by further intensity-based 3D-2D DIR.

The accuracy of the boundary-based 3D-2D DIR and further intensity-based 3D-2D DIR are performed on H&N05 cancer patient data. Both the NCC and NRMSE shown in Table 6 demonstrate that boundary-based DIR can provide a good initial guess of the deformation for the further intensity-based 3D-2D DIR; that is, after the boundary-based 3D-2D

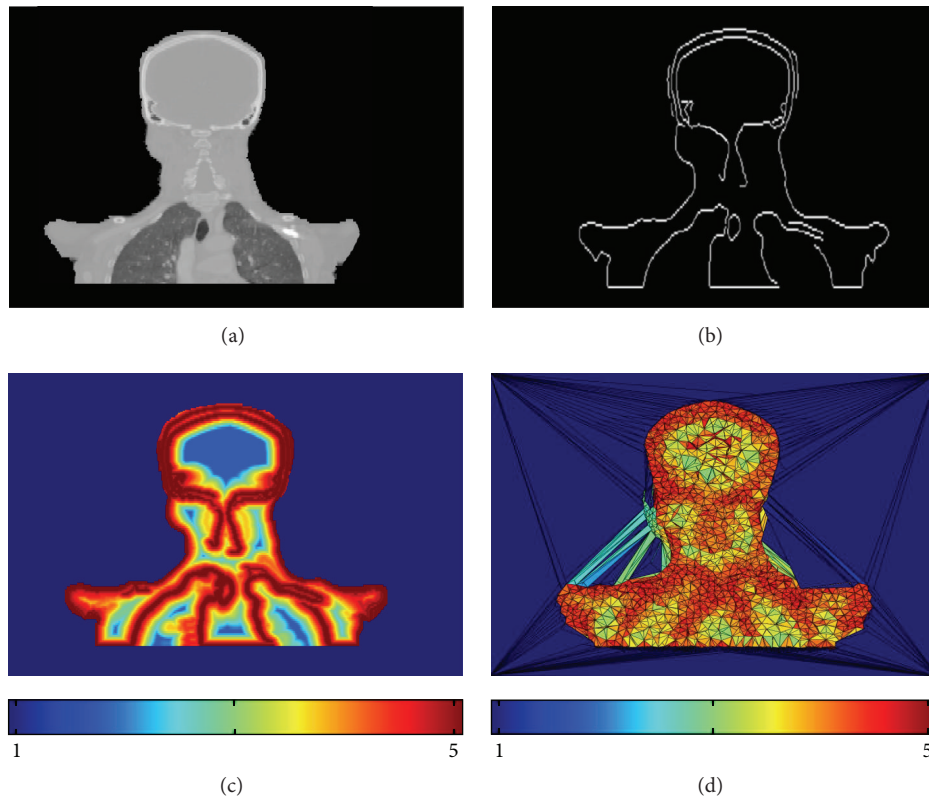


FIGURE 13: Demonstration of the feature-based mesh generation on the H&N01 patient data. (a) The original image; (b) extracted feature edges; (c) density field; (d) a 2D view of the interior meshes with color-mapping.

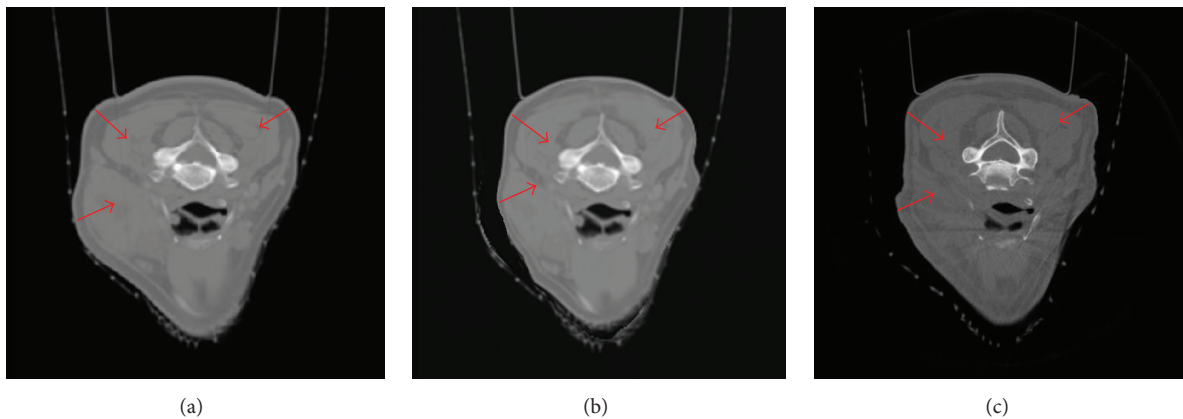


FIGURE 14: Demonstration of H&N01 patient results from axial view. (a) Original CT image; (b) deformed image; (c) target image (daily CBCT).

DIR, NCC and NRMSE are close to the final 3D-2D DIR accuracy results.

With the GPU-based implementation, taking this H&N cancer patient data for example, our boundary-guided method takes 5.26 seconds per iteration, which is about 10 times faster than the non-boundary-guided method (i.e., 59.75 seconds). The multiresolution scheme is used to further improve the speed on both boundary-based 3D-2D DIR and

further intensity-based 3D-2D DIR. In the experiment, only the CBCT images are downsampled into different resolution levels (three levels for experiments on H&N05 patient data), from the coarsest level (CBCT projection: 256×192 , time for boundary-based DIR: 1.37 seconds/iteration, and time for intensity-based DIR: 3.15 seconds/iteration) to the higher level (CBCT projection: 512×384 , time for boundary-based DIR: 2.11 seconds/iteration, and time for intensity-based DIR:

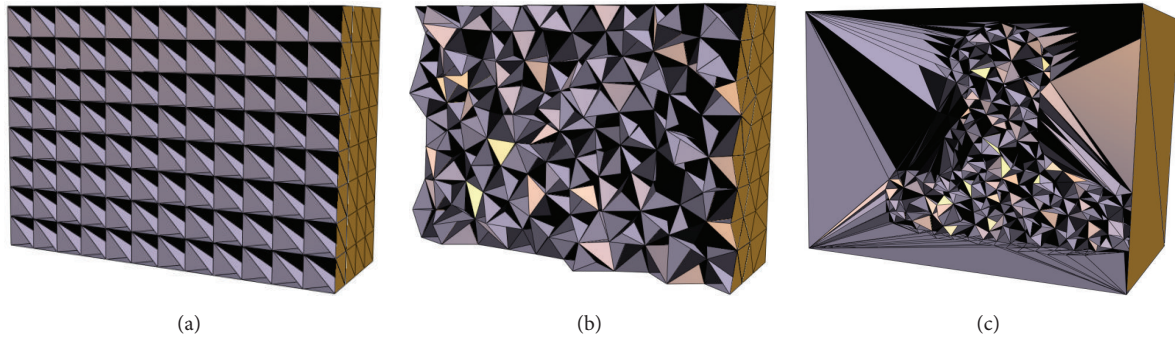


FIGURE 15: Three types of meshing for H&N01 cancer patient data. (a) A uniform orthogonal grid; (b) a uniform tetrahedron mesh; (c) a feature-based nonuniform tetrahedron mesh.

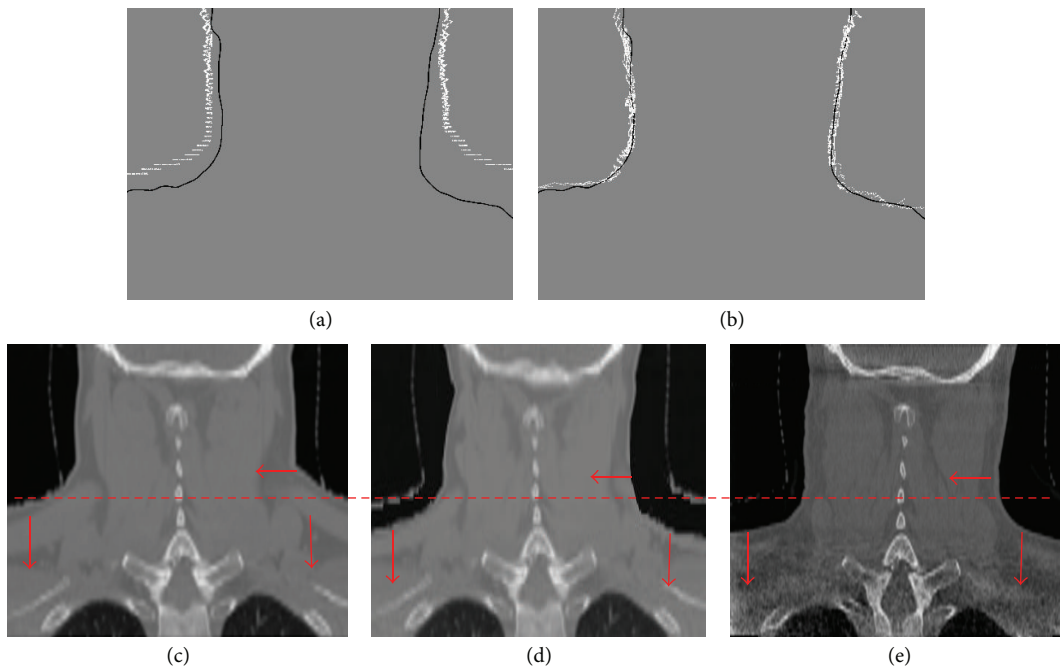


FIGURE 16: Demonstration of H&N05 patient data results. (a), (b) Differences between projection of the original/final surface voxel (white dots) and the target CBCT projection boundary (black dots); (c) original CT image; (d) reconstructed image from original CT image; (e) target image (daily CBCT).

15.01 seconds/iteration) and finally to the full resolution level (CBCT projection: 1024×768 , time for boundary-based DIR: 5.26 seconds/iteration, and time for intensity-based DIR: 59.75 seconds/iteration). At the same time, the proposed method needs fewer optimization iterations (35 iterations compared with original 50 iterations). The significant advantage of this method is that, instead of registering the whole image, we just need to register the surface voxel and projection boundaries, which involves much fewer number of voxels and pixels. In addition, in the H&N patient data case, we only focus on the 3D surface and 2D projection boundaries, so that the effects of different image modalities will be ignored. By using both GPU implementation and multiresolution scheme, the volumetric image reconstruction of $512 \times 512 \times 140$ H&N cancer patient can be accomplished

within 3 minutes (compared with 6.9 minutes of the original 3D-2D DIR in Section 2.2.5), so that this boundary-based 3D-2D DIR method could be probably used in the clinically practical studies.

4. Conclusion and Future Work

The feature-based nonuniform meshing allows more sampling points to be placed in the important regions; thus the deformation can be controlled more precisely. With the approximately same numbers of sampling points (vertices), the feature-based nonuniform meshing method produces better registration results, where a larger NCC is obtained compared with the uniform orthogonal grid and the uniform tetrahedron meshes. While this improvement may seem

small, it is important to note that the NCC is very close to 1 because only minor anatomic changes occur. The NRMSE measurement is also provided to represent the differences between deformed images and the ground truth images. In H&N patient data, again, the feature-based nonuniform meshing method yields the highest accuracy of registration among the various methods.

It is intuitive that more sampling points (10,000 versus 1,000) lead to better results. In contrast, the voxel-based deformation provides the best image results in XCAT male phantom but requires using more than eight million sampling points. However, when the optimized DVF is compared with the ground truth DVF, the DVF of voxel-based deformation is significantly less similar to the ground truth than the feature-based nonuniform meshing method. Voxel-based deformation may yield better image intensity result, but the resulting DVF represents an unrealistic anatomical mapping. This is a drawback of voxel-based deformation and is due to its localized deformation. The feature-based meshing method overcomes this drawback and yields more anatomically accurate DVF.

As for the mesh quality, before deformation, the nonuniform tetrahedral meshes are generated based on the smooth density field as introduced in Section 2.1.2 so that we can obtain the high-quality adaptive tetrahedral meshes without any degradation and self-intersection. After image registration (deformation), the adaptive tetrahedral meshes are all good as well. These are two factors to guarantee no degraded and self-intersected tetrahedrons in the deformed meshes: (1) in the proposed energy function in (9), the regularization term $L(\mathbf{D})$ and weighting factor μ are to achieve the smoothness of the DVFs. (2) The target DVFs are quite smooth in both the XCAT phantoms and H&N cancer patients. Of course, if the DVFs are highly varying with sharp discontinuities or weighting factor μ is not set properly, the deformed tetrahedral meshes will have problems, such as degradations or self-intersections. Since the mesh quality study is beyond the scope of this work, future studies are warranted.

The repeated use of CBCT during a course of treatment could deliver high extra imaging dose to patients. For example, if weekly CBCT pelvis scans are performed with the conventional fraction scheme, the total dose will be around $4.05 \text{ mSv/scan} \times 6 \text{ weeks} = 24.3 \text{ mSv}$; and the total dose of head scans will be around $2.0 \text{ mSv/scan} \times 6 \text{ weeks} = 12.0 \text{ mSv}$ (Table II in [39]). If the daily CBCT is performed, the total dose will be much higher. Using this method, far fewer projections are needed to produce a set of high-quality volumetric deformed images than in conventional CBCT reconstruction, which can dramatically reduce the radiation dose during CBCT scans. Additionally, it is clearly seen that the feature-based nonuniform meshing method has faster convergence speed than other methods during the registration process.

Moreover, the proposed boundary-based 3D-2D DIR method can substantially further improve both the accuracy and the speed of reconstructing volumetric images by producing a good initial DVF. This eventually will lead to a fast and safe daily volumetric imaging with a very small number of projections for image-guided radiation therapy or online

adaptive radiation therapy. There might be a limitation of this boundary-based method, if the deformation happens mainly in the internal organs. In the case of lung, its intensity is significantly different from that of chest wall, so we may segment lung and apply the proposed boundary-based 3D-2D DIR method only focusing on the lung first.

In the future, our feature-based nonuniform meshing method may also be applied to 4D images registration. A CBCT scan acquires approximately 600 hundred projections in a full rotation, and if they are sorted into ten respiratory phases, the corresponding 4D simulation CT set can be used to generate a high-quality, full 4D CBCT image set without exposing the patient to additional imaging dose. Currently, the feature-based nonuniform meshing method has been employed to some head and neck cancer patient data and achieved excellent results. In the future, we will investigate and determine the clinical accuracy of the method based on more patient data and statistical analysis in some follow-up applications for other cancer cases: such as breast, lung, and prostate cancers.

Conflict of Interests

The authors declare that there is no conflict of interests regarding the publication of this paper.

Acknowledgments

The authors would like to thank Drs. John Yordy, Susie Chen, and Lucien Nedzi in the Department of Radiation Oncology at UT Southwestern Medical Center for providing the head and neck cancer patients' data. This project was partially supported by Cancer Prevention & Research Institute of Texas (CPRIT) under Grant nos. RP110329 and RP110562 and National Science Foundation (NSF) under Grant nos. IIS-1149737 and CNS-1012975.

References

- [1] Y. Long, J. A. Fessler, and J. M. Balter, "Accuracy estimation for projection-to-volume targeting during rotational therapy: a feasibility study," *Medical Physics*, vol. 37, no. 6, pp. 2480–2490, 2010.
- [2] R. S. Brock, A. Docef, and M. J. Murphy, "Reconstruction of a cone-beam CT image via forward iterative projection matching," *Medical Physics*, vol. 37, no. 12, pp. 6212–6220, 2010.
- [3] J. Wang and X. Gu, "High-quality four-dimensional cone-beam CT by deforming prior images," *Physics in Medicine and Biology*, vol. 58, no. 2, pp. 231–246, 2013.
- [4] L. Ren, I. J. Chetty, J. Zhang et al., "Development and clinical evaluation of a three-dimensional cone-beam computed tomography estimation method using a deformation field map," *International Journal of Radiation Oncology Biology Physics*, vol. 82, no. 5, pp. 1584–1593, 2012.
- [5] G. P. Penney, J. Weese, J. A. Little, P. Desmedt, D. L. G. Hill, and D. J. Hawkes, "A comparison of similarity measures for use in 2D-3D medical image registration," *IEEE Transactions on Medical Imaging*, vol. 17, no. 4, pp. 586–595, 1998.
- [6] J. Kim, F.-F. Yin, Y. Zhao, and J. H. Kim, "Effects of x-ray and CT image enhancements on the robustness and accuracy of a rigid 3D/2D image registration," *Medical Physics*, vol. 32, no. 4, pp. 866–873, 2005.

- [7] R. Munbodh, H. D. Tagare, Z. Chen et al., "2D-3D registration for prostate radiation therapy based on a statistical model of transmission images," *Medical Physics*, vol. 36, no. 10, pp. 4555–4568, 2009.
- [8] J. Kybic and M. Unser, "Fast parametric elastic image registration," *IEEE Transactions on Image Processing*, vol. 12, no. 11, pp. 1427–1442, 2003.
- [9] A. Docef, M. Murphy, P. Keall, J. Siebers, and J. Williamson, "Forward CT reconstruction from limited projection data," in *Proceedings of the 19th Conference on Computer-Assisted Radiology and Surgery*, pp. 104–108, June 2005.
- [10] R. Zeng, J. A. Fessler, and J. M. Balter, "Estimating 3-D respiratory motion from orbiting views by tomographic image registration," *IEEE Transactions on Medical Imaging*, vol. 26, no. 2, pp. 153–163, 2007.
- [11] X. Jia, B. Dong, Y. Lou, and S. B. Jiang, "GPU-based iterative cone-beam CT reconstruction using tight frame regularization," *Physics in Medicine and Biology*, vol. 56, no. 13, pp. 3787–3807, 2011.
- [12] M. Ferrant, S. K. Warfield, A. Nabavi, F. A. Jolesz, R. Kikinis, and B. Macq, "Registration of 3-D intraoperative MR images of the brain using a finite-element biomechanical model," *IEEE Transactions on Medical Imaging*, vol. 20, no. 12, pp. 1384–1397, 2001.
- [13] O. Clatz, H. Delingette, I.-F. Talos et al., "Robust nonrigid registration to capture brain shift from intraoperative MRI," *IEEE Transactions on Medical Imaging*, vol. 24, no. 11, pp. 1417–1427, 2005.
- [14] B. Ahn and J. Kim, "Measurement and characterization of soft tissue behavior with surface deformation and force response under large deformations," *Medical Image Analysis*, vol. 14, no. 2, pp. 138–148, 2010.
- [15] Y. Hu, T. J. Carter, H. U. Ahmed et al., "Modelling prostate motion for data fusion during image-guided interventions," *IEEE Transactions on Medical Imaging*, vol. 30, no. 11, pp. 1887–1900, 2011.
- [16] P. Foteinos, Y. Liu, A. Chernikov, and N. Chrisochoides, "An evaluation of tetrahedral mesh generation for nonrigid registration of brain MRI," in *Computational Biomechanics for Medicine*, pp. 131–142, Springer, 2011.
- [17] E. Haber, S. Heldmann, and J. Modersitzki, "Adaptive mesh refinement for nonparametric image registration," *SIAM Journal on Scientific Computing*, vol. 30, no. 6, pp. 3012–3027, 2008.
- [18] M. Fogtman and R. Larsen, "Adaptive mesh generation for image registration and segmentation," in *Proceedings of the 20th IEEE International Conference on Image Processing (ICIP '13)*, pp. 757–760, IEEE, Melbourne, Australia, September 2013.
- [19] J. Zhang, J. Wang, X. Wang, and D. Feng, "The adaptive FEM elastic model for medical image registration," *Physics in Medicine and Biology*, vol. 59, no. 1, pp. 97–118, 2014.
- [20] J. G. Brankov, Y. Yang, and M. N. Wernick, "Content-adaptive 3D mesh modeling for representation of volumetric images," in *Proceedings of the International Conference on Image Processing*, vol. 3, pp. 849–852, IEEE, June 2002.
- [21] J. G. Brankov, Y. Yang, and M. N. Wernick, "Tomographic image reconstruction based on a content-adaptive mesh model," *IEEE Transactions on Medical Imaging*, vol. 23, no. 2, pp. 202–212, 2004.
- [22] W.-S. V. Shih, W.-C. Lin, and C.-T. Chen, "Contour-model-guided nonlinear deformation model for intersubject image registration," in *Medical Imaging: Image Processing*, vol. 3034 of *Proceedings of SPIE*, pp. 611–620, International Society for Optical Engineering, Newport Beach, Calif, USA, February 1997.
- [23] W.-N. Lie and C.-H. Chuang, "Contour-based image registration with local deformations," *Optical Engineering*, vol. 42, no. 5, pp. 1405–1416, 2003.
- [24] X. Gu, B. Dong, J. Wang et al., "A contour-guided deformable image registration algorithm for adaptive radiotherapy," *Physics in Medicine and Biology*, vol. 58, no. 6, pp. 1889–1901, 2013.
- [25] Z. Zhong, X. Guo, W. Wang et al., "Particle-based anisotropic surface meshing," *ACM Transactions on Graphics (TOG): SIGGRAPH 2013 Conference Proceedings*, vol. 32, no. 4, article 99, 2013.
- [26] J. Nash, " C^1 -isometric imbeddings," *Annals of Mathematics*, vol. 60, pp. 383–396, 1954.
- [27] N. H. Kuiper, "On C^1 -isometric embeddings I," *Proceedings of the Koninklijke Nederlandse Akademie van Wetenschappen Series A*, vol. 58, pp. 545–556, 1955.
- [28] M. do Carmo, *Riemannian Geometry*, Birkhäuser, 1992.
- [29] M. de Berg, O. Cheong, M. van Kreveld, and M. Overmars, *Computational Geometry: Algorithms and Applications*, Springer, New York, NY, USA, 2008.
- [30] D. C. Liu and J. Nocedal, "On the limited memory BFGS method for large scale optimization," *Mathematical Programming*, vol. 45, no. 3, pp. 503–528, 1989.
- [31] W. P. Segars and B. M. W. Tsui, "MCAT to XCAT: the evolution of 4-D computerized phantoms for imaging research," *Proceedings of the IEEE*, vol. 97, no. 12, pp. 1954–1968, 2009.
- [32] H. Coxeter, *Introduction to Geometry*, John Wiley & Sons, 2nd edition, 1969.
- [33] R. L. Siddon, "Fast calculation of the exact radiological path for a three-dimensional CT array," *Medical Physics*, vol. 12, no. 2, pp. 252–255, 1985.
- [34] J. Wang, T. Li, H. Lu, and Z. Liang, "Penalized weighted least-squares approach to sinogram noise reduction and image reconstruction for low-dose X-ray computed tomography," *IEEE Transactions on Medical Imaging*, vol. 25, no. 10, pp. 1272–1283, 2006.
- [35] P. J. La Rivière and D. M. Billmire, "Reduction of noise-induced streak artifacts in X-ray computed tomography through spline-based penalized-likelihood sinogram smoothing," *IEEE Transactions on Medical Imaging*, vol. 24, no. 1, pp. 105–111, 2005.
- [36] K. Zhou, J. Huang, J. Snyder et al., "Large mesh deformation using the volumetric graph laplacian," *ACM Transactions on Graphics*, vol. 24, no. 3, pp. 496–503, 2005.
- [37] J. Canny, "A computational approach to edge detection," *IEEE Transactions on Pattern Analysis and Machine Intelligence*, vol. 8, no. 6, pp. 679–698, 1986.
- [38] L. Westover, "Footprint evaluation for volume rendering," in *Proceedings of the 17th Annual Conference on Computer Graphics and Interactive Techniques (SIGGRAPH '90)*, pp. 367–376, ACM, Dallas, Tex, USA, August 1990.
- [39] R. A. Hälgl, J. Besserer, and U. Schneider, "Systematic measurements of whole-body imaging dose distributions in image-guided radiation therapy," *Medical Physics*, vol. 39, no. 12, pp. 7650–7661, 2012.

Review Article

Combining Whole-Brain Radiotherapy with Gefitinib/Erlotinib for Brain Metastases from Non-Small-Cell Lung Cancer: A Meta-Analysis

Mao-hua Zheng,^{1,2,3} Hong-tao Sun,⁴ Ji-guang Xu,¹ Gang Yang,¹
Lei-ming Huo,¹ Pan Zhang,² Jin-hui Tian,^{2,3} and Ke-hu Yang^{2,3}

¹Department of Neurosurgery, First Clinical Medical College of Lanzhou University, Lanzhou 730000, China

²Evidence-Based Medicine Center of Lanzhou University, Lanzhou 730000, China

³Key Laboratory of Evidence-Based Medicine and Knowledge Translation of Gansu Province, Lanzhou 730000, China

⁴Department of Neurosurgery, Affiliated Hospital, Medical College of Chinese People's Armed Police, Tianjin 300162, China

Correspondence should be addressed to Ke-hu Yang; kehuyangebm2006@163.com

Received 3 July 2015; Accepted 2 December 2015

Academic Editor: Jun Deng

Copyright © 2016 Mao-hua Zheng et al. This is an open access article distributed under the Creative Commons Attribution License, which permits unrestricted use, distribution, and reproduction in any medium, provided the original work is properly cited.

Background. To comprehensively assess the efficacy and safety of whole-brain radiotherapy (WBRT) combined with gefitinib/erlotinib for treatment of brain metastases (BM) from non-small-cell lung cancer (NSCLC). **Methods.** Databases including PubMed, EMBASE.com, Web of Science, and Cochrane Library were searched from inception to April 12, 2015. Studies on randomized controlled trials (RCTs) and case-control trials comparing WBRT combined with gefitinib/erlotinib versus WBRT alone for BM from NSCLC were included. Literature selection, data extraction, and quality assessment were performed independently by two trained reviewers. RevMan 5.3 software was used to analyze data. **Results.** A total of 7 trials involving 622 patients were included. Compared with WBRT alone or WBRT plus chemotherapy, WBRT plus gefitinib/erlotinib could significantly improve response rate (OR = 2.16, 95% CI: 1.35–3.47; $P = 0.001$), remission rate of central nervous system (OR = 6.06, 95% CI: 2.57–14.29; $P < 0.0001$), disease control rate (OR = 3.34, 95% CI: 1.84–6.07; $P < 0.0001$), overall survival (HR = 0.72, 95% CI: 0.58–0.89; $P = 0.002$), and 1-year survival rate (OR = 2.43, 95% CI: 1.51–3.91; $P = 0.0002$). In adverse events (III–IV), statistically significant differences were not found, except for rash (OR = 7.96, 95% CI: 2.02–31.34; $P = 0.003$) and myelosuppression (OR = 0.19, 95% CI: 0.07–0.51; $P = 0.0010$). **Conclusions.** WBRT plus gefitinib/erlotinib was superior to WBRT alone and well tolerated in patients with BM from NSCLC.

1. Introduction

Brain metastases (BM) are the most frequent intracranial brain tumors, which can be found in approximately 20–40% of all cancer patients. Lung and breast cancers and melanoma are responsible for up to 80% of metastatic brain lesions [1]. Among patients with non-small-cell lung cancer (NSCLC), the proportion that develops brain metastases is as high as 50% [2]. Life expectancy for these patients is poor, and the average survival is 1–2 months without any treatment [3]. A median survival of 3–6 months can be obtained for patients receiving symptomatic therapy with corticosteroids and whole-brain radiotherapy (WBRT) [4].

Recently, several phase II or phase III trials of standard platinum-based chemotherapy regimens for BM from NSCLC have been conducted [5–10], resulting in 23%–68% response rate and 4–12.6-month overall survival. However the effect of combining WBRT with chemotherapy in the management of BM is limited and inconsistent due to the limited ability of most chemotherapeutic drugs to cross the blood brain barrier [11].

In recent years, new targeted therapies are undergoing active development and encouraging results have been obtained so far [12]. A previously published review demonstrated the intracranial efficacy of targeted therapies (EGFR tyrosine kinase inhibitors, ALK inhibitors), which were

globally superior to the efficacy of standard chemotherapy [13]. However, this review was qualitative and the quality of evidence was not evaluated. Some retrospective series and phase II randomized studies have been conducted recently to compare the efficacy of combining WBRT with gefitinib/erlotinib versus WBRT alone for patients with BM from NSCLC.

Our study aims therefore to comprehensively assess the quality of currently available evidences and to quantitatively evaluate the efficacy and safety of WBRT combined with gefitinib/erlotinib for BM from NSCLC.

2. Methods

This study adhered to the Preferred Reporting Items for Systematic Review and Meta-Analysis (PRISMA) statement [14]. Ethical approval and patient consent were unnecessary for the current study as this was a meta-analysis based on published studies. Literature retrieval, literature selection, data extraction, and quality assessment were performed independently by two trained reviewers; disagreements between the reviewers were resolved by consulting a third expert adjudicator.

2.1. Literature Retrieval. Databases retrieved included PubMed, EMBASE.com, Web of Science (via ISI Web of Knowledge), and the Cochrane Library from inception to April 12, 2015, using the terms epidermal growth factor receptor, EGFR, erlotinib, tarceva, erbitinib, iressa, gefitinib, gefitinat, brain neoplasm*, brain cancer*, brain carcinoma*, brain tumor*, metasta*, lung neoplasm*, lung cancer*, lung carcinoma*, lung tumor*, whole-brain radiotherapy, WBRT, and other. The references of included studies were tracked to identify potential relevant studies. The search strategy for PubMed was as follows: (((("lung neoplasm*" [Title/Abstract] OR "lung cancer*" [Title/Abstract] OR "lung carcinoma*" [Title/Abstract] OR "lung tumor*" [Title/Abstract] OR "Lung Neoplasms" [Mesh]))) AND ((metasta* [Title/Abstract]) AND (((("brain neoplasm*" [Title/Abstract] OR "brain cancer*" [Title/Abstract] OR "brain carcinoma*" [Title/Abstract] OR "brain tumor*" [Title/Abstract]))) OR "Brain Neoplasms" [Mesh]))) AND ((("whole-brain radiotherapy" [Title/Abstract] OR WBRT [Title/Abstract] OR "radiation therapy" [Title/Abstract] OR radiotherapy [Title/Abstract] OR "irradiation therapy" [Title/Abstract] OR "radiation therapy" [Title/Abstract] OR "Radiotherapy" [Mesh]))) AND (((("epidermal growth factor receptor" [Title/Abstract] OR EGFR [Title/Abstract] OR erlotinib [Title/Abstract] OR tarceva [Title/Abstract] OR erbitinib [Title/Abstract] OR iressa [Title/Abstract] OR gefitinib [Title/Abstract] OR gefitinat [Title/Abstract]))) OR "Receptor, Epidermal Growth Factor" [Mesh]).

2.2. Inclusion Criteria. Studies meeting the following eligibility criteria were included: (a) type of population: histologically or cytologically confirmed NSCLC and multiple BM (≥ 3) documented by MRI or contrast CT scan; aged 18 years of age or older; (b) type of intervention: WBRT plus erlotinib/ gefitinib; (c) type of comparison: WBRT alone or

WBRT plus chemotherapy; (d) type of design: randomized controlled trials (RCTs) or case-control studies; (e) type of outcomes: response rate (RR) and overall survival (OS) were primary endpoints; toxicity, disease control rate (DCR), 1-year survival rate, and remission rate of central nervous system (RR-CNS) were secondary endpoints.

2.3. Literature Selection. All records were downloaded and imported into EndNote X6, which is a reference management software tool. Duplicates were removed and the title and abstract of the remaining records were examined independently by two reviewers according to inclusion and exclusion criteria. Then the full texts of potentially relevant studies were obtained to identify interesting studies. Reasons for exclusion were documented.

2.4. Data Extraction and Assessment of Risk of Bias. Data were extracted using a pre-designed data extraction sheet including the first author, year of publications, sample, median age, intervention regimen, control regimen, study design, outcomes, median OS, and median PFS. Kaplan-Meier curve was read by Engauge Digitizer version 4.1 (available at <http://sourceforge.net/>) if the adequate data were not reported in the papers [15], and the formula recommended by Spruance et al. [16] was used to calculate the corresponding HR of the missing survival data.

The risk of bias was assessed according to the Cochrane Handbook version 5.1.0 [17], including method of random sequence generation (selection bias), allocation concealment (selection bias), blinding (performance bias and detection bias), incomplete outcome data (detection bias), and selective reporting (detection bias). We evaluated methodological quality as low, high, or unclear risk of bias.

2.5. Data Analysis. The odds ratio (OR) with 95% confidence interval (95% CI) was calculated regarding to RR, CN-RR, DCR, 1-year survival rate, and AEs. The Chi-square statistic was used to assess the heterogeneity between trials with I^2 less than 50% and P value greater than 0.10 suggesting that there was no statistical heterogeneity, and a Mantel-Haenszel fixed effects model was used for meta-analysis. A Mantel-Haenszel random effects model was used when clinical characteristics and methodology were not identified to have great difference and I^2 was greater than 50% and P value was less than 0.10. If the clinical characteristic and/or methodology across studies were considered to be obviously different, only qualitative analysis was adopted [18]. Inverse variance fixed or random effects model was used to pool the overall hazard ratio (HR) for OS. When heterogeneity was identified, subgroup analysis and metaregression were conducted to determine the possible causes of heterogeneity such as different target agents (erlotinib or gefitinib), different study designs (randomized or nonrandomized), and sample size (<100 or ≥ 100). Sensitivity analysis was performed to identify influence of the study regarding overall effective size. In addition, potential publication bias was assessed by using the Begg and Egger tests [19, 20]. P value less than 0.05 was considered significant. All data analysis was performed by

using RevMan 5.3 software (The Nordic Cochrane Centre, Copenhagen, Denmark) and STATA 12.0 software (Stata Corporation, College Station, Texas, USA).

3. Results

3.1. Literature Selection and Characteristics of Included Studies. A total of 426 records were identified from electronic databases and 4 references were tracked. Finally, 7 studies [21–27] involving 622 patients were included. The search results and selection details are shown in Figure 1.

The detailed characteristics of included studies are shown in Table 1. Of the seven studies included, three [22, 24, 26] were randomized controlled trials and four [21, 23, 25, 27] were case-control studies. They were published between 2012 and 2014. The sample sizes ranged from 53 to 161. Three studies could be identified as phase II and four did not report trial phase. Median OS was reported in five studies [22, 24–27], and only two [22, 27] reported median nPFS.

3.2. Assessment of Risk of Bias. The details of this analysis are shown in Figure 2. Four studies were case-control trials; therefore the risk of bias was high regarding adequate sequence generation, adequate allocation concealment, and blinding. Of three RCTs included, all described methods for adequate sequence generation such as center random and minimization method; two RCTs reported using adequate allocation concealment, and one RCT was a double-blinded design study. The overall methodological quality of included studies was poor because only three were RCTs.

4. Results of Meta-Analysis

4.1. Response Rate (RR). Four studies [23–25, 27] reported the overall response rate for patients with BM. The heterogeneity test indicated that a fixed effects model could be used to pool the RR ($I^2 = 17\%$, $P = 0.31$). Compared with WBRT alone, there was a statistically significant improvement in RR for WBRT combined with gefitinib/erlotinib (OR = 2.16, 95% CI: 1.35–3.47; $P = 0.001$) (Figure 3).

Three studies [21, 23, 25] reported the RR-CNS, with 273 patients involved. There was no significant statistical heterogeneity in pooled analysis of all included studies ($I^2 = 22\%$, $P = 0.28$) and thus a fixed effects model was used to perform meta-analysis. Compared with WBRT alone, there was a statistically significant improvement in RR-CNS for WBRT combined with gefitinib/erlotinib (OR = 6.06, 95% CI: 2.57–14.29; $P < 0.0001$) (Figure 3).

4.2. Disease Control Rate (DCR). Four studies [23–25, 27] reported the overall response rate, with 429 patients involved. The heterogeneity test indicated that a fixed effects model could be used ($I^2 = 0\%$, $P = 0.59$). Compared with WBRT alone, there was a statistically significant improvement in DCR for WBRT combined with gefitinib/erlotinib (OR = 3.34, 95% CI: 1.84–6.07; $P < 0.0001$) (Figure 3).

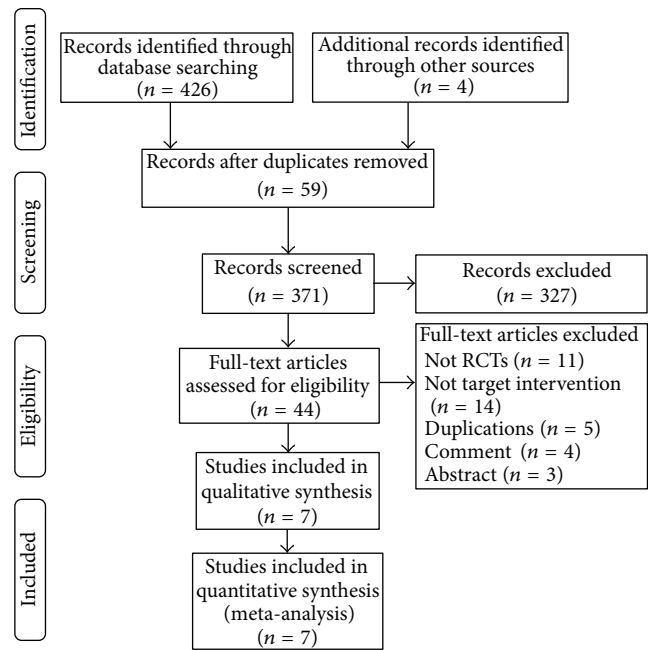


FIGURE 1: Literature selection flow graph.

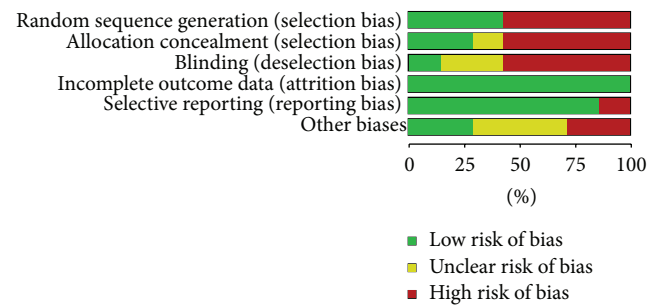


FIGURE 2: Analysis of risk of bias.

4.3. Overall Survival (OS). Five studies [21, 22, 25–27] reported the overall survival, with 408 patients involved. The heterogeneity test indicated that a fixed effects model could be used ($I^2 = 33\%$, $P = 0.20$). The meta-analysis showed that WBRT combined with gefitinib/erlotinib significantly prolonged OS compared to WBRT alone (HR = 0.72, 95% CI: 0.58–0.89; $P = 0.002$) (Figure 4).

4.4. 1-Year Survival Rate. Four studies [24–27] reported the 1-year survival rate, with 327 patients involved. The heterogeneity test indicated that a fixed effects model could be used ($I^2 = 0\%$, $P = 0.45$). The meta-analysis showed that WBRT combined with gefitinib/erlotinib significantly prolonged 1-year survival rate compared to WBRT alone (OR = 2.43, 95% CI: 1.51–3.91; $P = 0.0002$) (Figure 5).

4.5. Adverse Events (III-IV). The results of the meta-analysis for adverse events are shown in Figure 6. The heterogeneity tests for all adverse events indicated that there were no statistical differences except for myelosuppression (III-IV)

TABLE 1: Characteristics of included studies.

Studies	Samples		Median age (years)		Intervention regimens	Control regimens	Design	Phase	Median OS (months)	Median nPFS (months)
	W-T	W	W-T	W						
Zhuang et al., 2013 [21]	23	31	60 (37-76)	63 (43-81)	WBRT 30 Gy/10 f plus erlotinib 150 mg/day	WBRT 30 Gy/10 f	Case-control	II	NR	NR
Lee et al., 2014 [22]	40	40	61.3 (48-75)	62.2 (41-73)	WBRT 20 Gy/5 f plus erlotinib 100 mg/day	WBRT 20 Gy/5 f + placebo	Randomized	II	3.4/2.9	1.6/1.6
Fu et al., 2012 [23]	38	123	A56 (38-77)		WBRT 30-40 Gy/2-3 W plus gefitinib 250 mg/day	WBRT 30-40 Gy/2-3 W	Case-control	NR	NR	NR
Wu et al., 2012 [24]	35	18	18-65		WBRT 40 Gy/20 f plus gefitinib 250 mg/day	WBRT 40 Gy/20 f	Randomized	NR	12.1/9.8	NR
Zhou et al., 2013 [25]	36	22	27-75		WBRT 40 Gy/20 f or 30 Gy/10 f plus gefitinib 250 mg/day or erlotinib 100 mg/day	WBRT 40 Gy/20 f or 30 Gy/10 f plus Taxol 135-175 mg/m ² d1 or Alimta 500 mg/m ² d1 or DDP 25 mg/m ² (d1-3)	Case-control	NR	23.2/7.1	NR
Pesce et al., 2012 [26]	16	43	57 (46-82)	63 (45-79)	WBRT 30 Gy/10 f plus gefitinib 250 mg/day	WBRT 30 Gy/10 f plus TMZ 75 mg/m ² /day	Randomized	II	6.3/4.9	NR
Cai et al., 2013 [27]	65	92	66 (35-81)		WBRT 29.37~41.24 Gy, 3 Gy/d, 5 times/week plus gefitinib 250 mg/day or erlotinib 100 mg/day	WBRT 29.37~41.24 Gy, 3 Gy/d, 5 times/week	Case-control	NR	10.6/7.7	6/3.4

Notes: W-T: WBRT plus erlotinib/ gefitinib; W: WBRT; NR: not reported; OS: overall survival; PFS: progression-free survival.

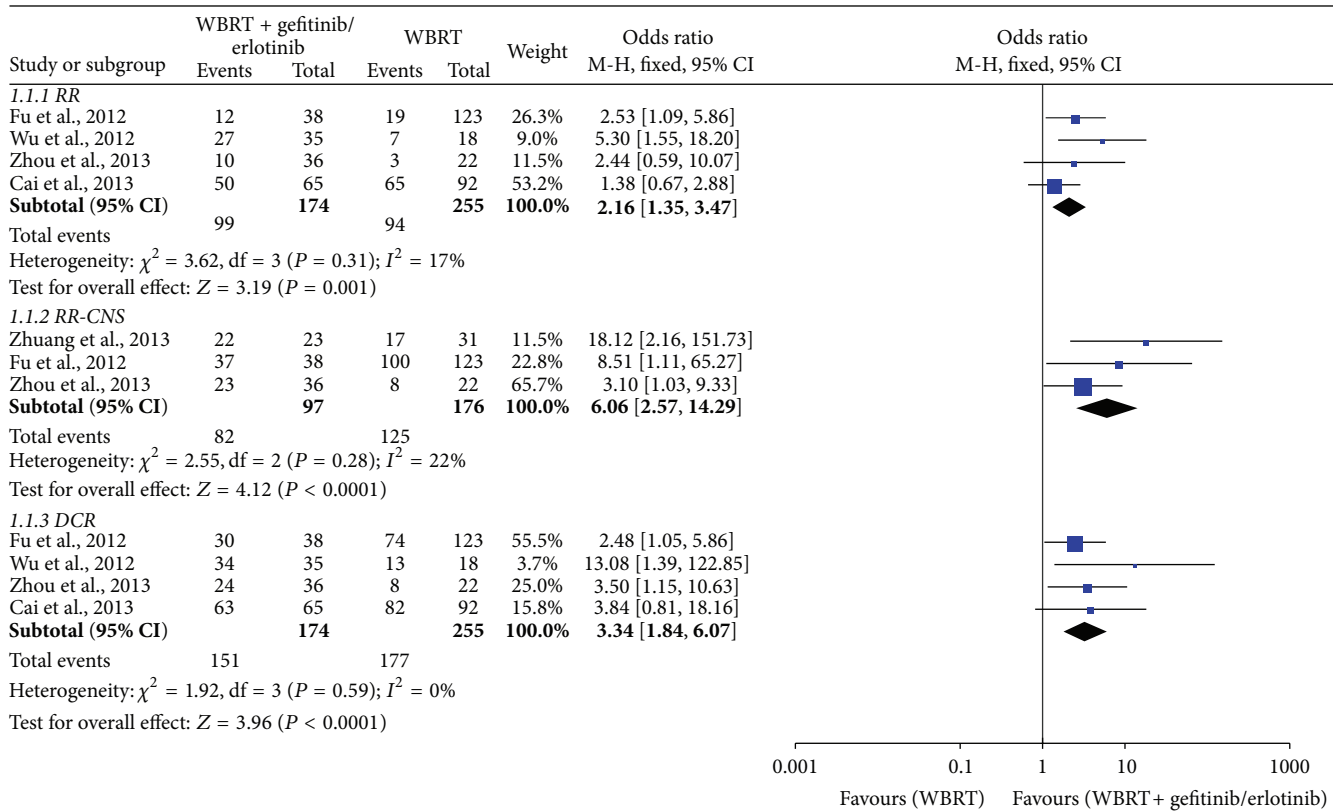


FIGURE 3: Meta-analysis for RR, RR-CNS, and DCR.

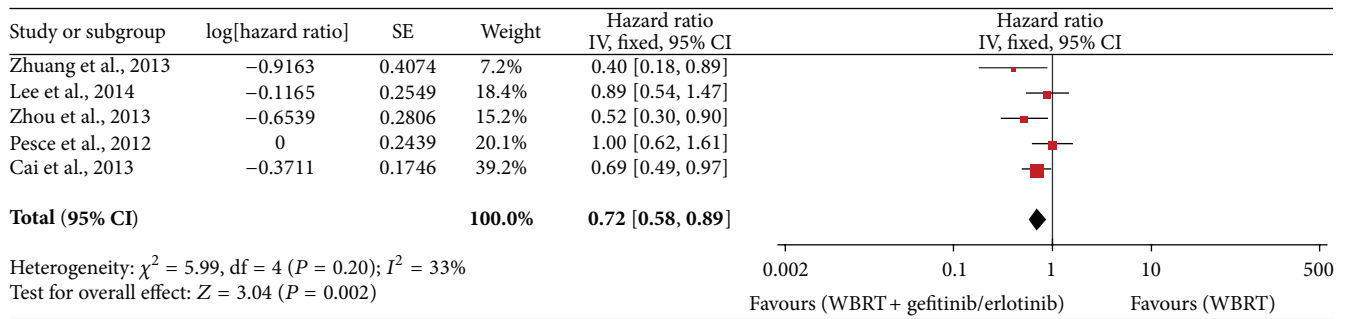


FIGURE 4: Meta-analysis for OS.

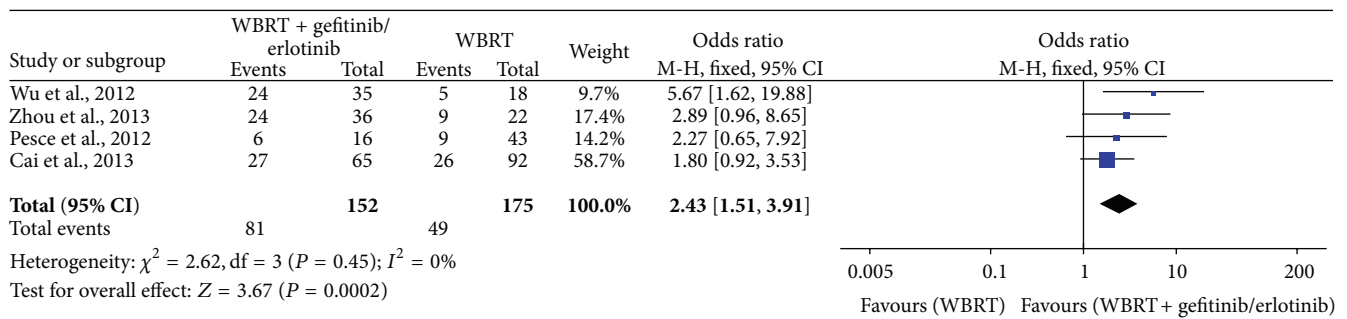


FIGURE 5: Meta-analysis for 1-year survival rate.

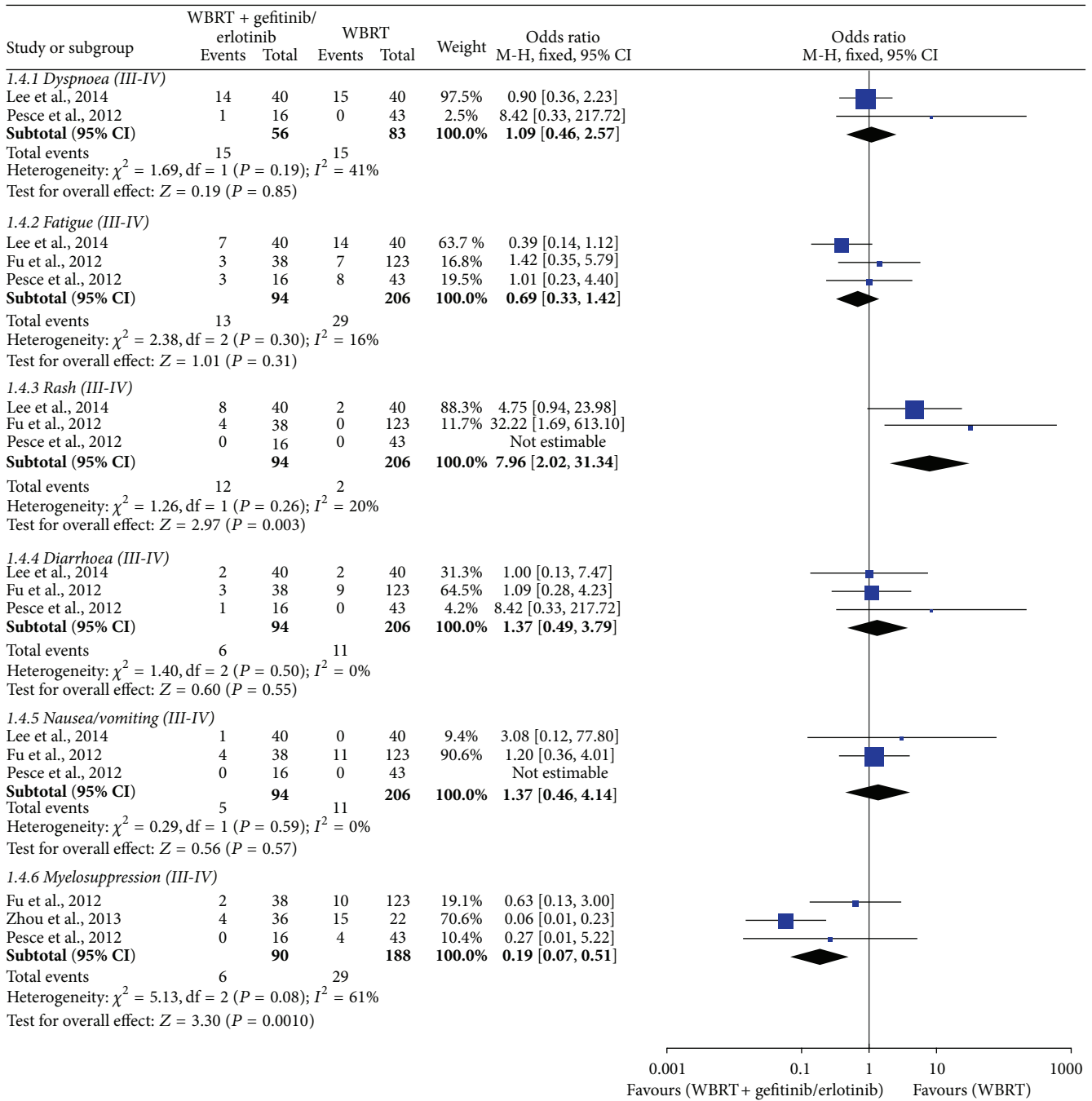


FIGURE 6: Meta-analysis for adverse events (III-IV).

($I^2 < 50\%$, $P > 0.10$). The meta-analysis showed that WBRT plus gefitinib/erlotinib increased the incidence of rash (III-IV) (OR = 7.96, 95% CI: 2.02–31.34; $P = 0.003$) but reduced the incidence of myelosuppression (III-IV) (OR = 0.19, 95% CI: 0.07–0.51; $P = 0.0010$). Statistical differences were not found regarding other adverse events.

4.6. Subgroup Analysis and Sensitivity Analysis. The heterogeneity tests for interesting outcomes indicated that there

were no statistical differences between studies ($I^2 < 50\%$, $P > 0.10$). Therefore subgroup analysis and meta regression were not conducted for the current study.

Figure 7 shows the results of sensitivity analysis regarding OS. We found that excluded studies did not influence the overall effective size.

4.7. Publication Bias. For the meta-analyses of RR and OS, there was no evidence of significant publication bias by

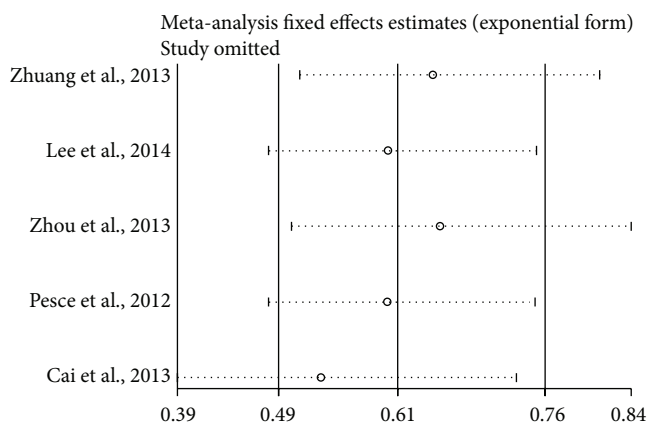


FIGURE 7: Sensitivity analysis of OS.

inspection of the formal statistical tests (RR: Egger's test, $P = 0.276$; Begg's test, $P = 0.497$ and OS: Egger's test, $P = 0.478$; Begg's test, $P = 0.142$).

5. Discussion

This is a systematic review and meta-analysis to comprehensively assess the efficacy and safety of WBRT combined with gefitinib/erlotinib for treatment of BM from NSCLC. The present meta-analysis suggests that compared with WBRT alone or WBRT plus chemotherapy, WBRT plus gefitinib/erlotinib can significantly improve the RR, RR-CNS, and DCR and prolong the OS and 1-year survival rate. Regarding the incidences of adverse events, WBRT plus gefitinib/erlotinib was well tolerated except for increased risk of rash (III-IV) in the treatment of patients with multiple BM from NSCLC.

Current therapeutic approaches for patients with multiple BM from NSCLC mainly include surgery, whole-brain radiotherapy (WBRT), stereotactic radiosurgery (SRS), and chemotherapy [28]. However, advances in the understanding of the BM pathobiology and development of molecular targeted agents hold promise for improved prophylaxis and therapy of BM [29]. Epidermal growth factor receptor (EGFR) tyrosine kinase inhibitors (TKIs), such as erlotinib, have been approved in 2004 by the US Food and Drug Administration for treating locally advanced or metastatic NSCLC [30]. A mass of studies have demonstrated that the objective response rate is 42.9%–87.5%, and DCR is as high as 87.5%–100.0% for targeted agents combined with radiotherapy in the treatment of patients with multiple BM [31]. A phase II trial also showed that the median overall survival time was 11.8 months for patients with BM from NSCLC [32]. These results are consistent with Zhuang et al. [21]. However, Pesce et al. [26] concluded that WBRT plus gefitinib could not prolong the survival time for patients with BM from NSCLC. The discrepancy can be ascribed to the limited sample size of Pesce et al.'s study. A meta-analysis was therefore urgently needed to systematically assess the quality

of available evidence and make a scientific conclusion about WBRT plus gefitinib/erlotinib in treating BM from NSCLC.

Regrettably, a subgroup meta-analysis related to EGFR mutation status was not conducted because only one trial was identified. Previous studies showed that targeted therapy was beneficial for patients with BM. The overall response rate was 70%–89% for patients with intracranial lesions, and the overall survival time was 12.9–19.8 months longer [33, 34]. Zhuang et al.'s study showed that, compared with EGFR wild-type patients, there was no significant improvement in LPFS, PFS, and OS for mutated EGFR mutation patients [21]. More studies of WBRT plus gefitinib/erlotinib in treatment of BM with EGFR mutations are needed.

The present study had certain limitations. Firstly, the overall methodological quality of included studies was low. Only three RCTs were included to assess the efficacy of the combined treatment. Most of the studies evaluating WBRT plus gefitinib/erlotinib for BM from NSCLC were case series, and only few controlled trials could be identified. Secondly, the small sample size of the included studies might have led to inadequate statistical power. The present conclusions are based on phase II trials, and more phase III randomized controlled trials are needed. Thirdly, subgroup analyses of different pathological subtypes, trial phase, smoking status, median age, and EGFR mutations status were not performed due to inadequate reporting across studies.

Overall, the currently available evidence indicates that RR, RR-CNS, DCR, OS, and 1-year survival rate can be improved by using WBRT combined with gefitinib/erlotinib in patients with BM from NSCLC, and the adverse events (III-IV) are well tolerated. Moreover, the efficacy of other targeted agents for BM from NSCLC should be assessed in future studies.

Conflict of Interests

The authors declare that they have no conflict of interests.

Authors' Contribution

Mao-hua Zheng and Hong-tao Sun contributed equally to this work.

References

- [1] J. Gállego Pérez-Larraya and J. Hildebrand, "Brain metastases," in *Handbook of Clinical Neurology*, vol. 121 of *Neurologic Aspects of Systemic Disease Part III*, chapter 77, pp. 1143–1157, Elsevier, 2014.
- [2] D. E. Dawe, J. N. Greenspoon, and P. M. Ellis, "Brain metastases in non-small-cell lung cancer," *Clinical Lung Cancer*, vol. 15, no. 4, pp. 249–257, 2014.
- [3] C. G. Patil, K. Pricola, J. M. Sarmiento, S. K. Garg, A. Bryant, and K. L. Black, "Whole brain radiation therapy (WBRT) alone versus WBRT and radiosurgery for the treatment of brain metastases," *Cochrane Database of Systematic Reviews*, vol. 9, Article ID CD006121, 2012.
- [4] F. J. Lagerwaard, P. C. Levendag, P. J. C. M. Nowak, W. M. H. Eijkenboom, P. E. J. Hanssens, and P. I. M. Schmitz,

- "Identification of prognostic factors in patients with brain metastases: a review of 1292 patients," *International Journal of Radiation Oncology, Biology, Physics*, vol. 43, no. 4, pp. 795–803, 1999.
- [5] V. Franciosi, G. Cocconi, M. Michiara et al., "Front-line chemotherapy with cisplatin and etoposide for patients with brain metastases from breast carcinoma, non small cell lung carcinoma, or malignant melanoma: a prospective study," *Cancer*, vol. 85, pp. 1599–1605, 1999.
 - [6] X.-X. Dinglin, Y. Huang, H. Liu, Y.-D. Zeng, X. Hou, and L.-K. Chen, "Pemetrexed and cisplatin combination with concurrent whole brain radiotherapy in patients with brain metastases of lung adenocarcinoma: a single-arm phase II clinical trial," *Journal of Neuro-Oncology*, vol. 112, no. 3, pp. 461–466, 2013.
 - [7] J. Cortes, J. Rodriguez, J. M. Aramendia et al., "Front-line paclitaxel/cisplatin-based chemotherapy in brain metastases from non-small-cell lung cancer," *Oncology*, vol. 64, no. 1, pp. 28–35, 2003.
 - [8] J. P. Kleisbauer, J. C. Guerin, A. Arnaud, R. Poirier, and D. Vesco, "Chemotherapy with high-dose cisplatin in brain metastasis of lung cancers," *Bulletin du Cancer*, vol. 77, pp. 661–665, 1990.
 - [9] C. Cotto, J. Berille, P. J. Souquet et al., "A phase II trial of fotemustine and cisplatin in central nervous system metastases from non-small cell lung cancer," *European Journal of Cancer*, vol. 32, no. 1, pp. 69–71, 1996.
 - [10] A. Fujita, S. Fukuoka, H. Takabatake, S. Tagaki, and K. Sekine, "Combination chemotherapy of cisplatin, ifosfamide, and irinotecan with rhG-CSF support in patients with brain metastases from non-small cell lung cancer," *Oncology*, vol. 59, no. 4, pp. 291–295, 2000.
 - [11] S. Ma, Y. Xu, Q. Deng, and X. Yu, "Treatment of brain metastasis from non-small cell lung cancer with whole brain radiotherapy and Gefitinib in a Chinese population," *Lung Cancer*, vol. 65, no. 2, pp. 198–203, 2009.
 - [12] G. Lombardi, A. L. Di Stefano, P. Farina, V. Zagonel, and E. Tabouret, "Systemic treatments for brain metastases from breast cancer, non-small cell lung cancer, melanoma and renal cell carcinoma: an overview of the literature," *Cancer Treatment Reviews*, vol. 40, no. 8, pp. 951–959, 2014.
 - [13] F. Barlesi, J.-P. Spano, A. B. Cortot, A. F. Carpentier, G. Robinet, and B. Besse, "Systemic treatment of brain metastases from lung cancer," *Cancer/Radiothérapie*, vol. 19, no. 1, pp. 43–47, 2015.
 - [14] A. Liberati, D. G. Altman, J. Tetzlaff et al., "The PRISMA statement for reporting systematic reviews and meta-analyses of studies that evaluate healthcare interventions: explanation and elaboration," *British Medical Journal*, vol. 339, Article ID b2700, 2009.
 - [15] G. Tarro, A. Perna, and C. Esposito, "Early diagnosis of lung cancer by detection of tumor liberated protein," *Journal of Cellular Physiology*, vol. 203, no. 1, pp. 1–5, 2005.
 - [16] S. L. Spruance, J. E. Reid, M. Grace, and M. Samore, "Hazard ratio in clinical trials," *Antimicrobial Agents and Chemotherapy*, vol. 48, no. 8, pp. 2787–2792, 2004.
 - [17] J. P. T. Higgins and S. Green, *Cochrane Handbook for Systematic Reviews of Interventions Version 5.1.0 [EB/OL]*, The Cochrane Collaboration, 2011, <http://www.cochrane-handbook.org>.
 - [18] J. P. T. Higgins and S. G. Thompson, "Quantifying heterogeneity in a meta analysis," *Statistics in Medicine*, vol. 21, no. 11, pp. 1539–1558, 2002.
 - [19] C. B. Begg and M. Mazumdar, "Operating characteristics of a rank correlation test for publication bias," *Biometrics*, vol. 50, no. 4, pp. 1088–1101, 1994.
 - [20] M. Egger, G. D. Smith, M. Schneider, and C. Minder, "Bias in meta-analysis detected by a simple, graphical test," *British Medical Journal*, vol. 315, no. 7109, pp. 629–634, 1997.
 - [21] H. Zhuang, Z. Yuan, J. Wang, L. Zhao, Q. Pang, and P. Wang, "Phase ii study of whole brain radiotherapy with or without erlotinib in patients with multiple brain metastases from lung adenocarcinoma," *Drug Design, Development and Therapy*, vol. 7, pp. 1179–1186, 2013.
 - [22] S. M. Lee, C. R. Lewanski, N. Counsell et al., "Randomized trial of erlotinib plus whole-brain radiotherapy for NSCLC patients with multiple brain metastases," *Journal of the National Cancer Institute*, vol. 106, no. 7, Article ID dju151, 2014.
 - [23] H. Fu, X. L. Zhang, Y. Xiao, X. J. Liu, C. Long, and Y. D. Hu, "Evaluation of gefitinib plus radiotherapy in non-small-cell lung cancer patients with brain metastases," *National Medical Journal of China*, vol. 92, no. 8, pp. 524–527, 2012.
 - [24] T. A. Wu, D. R. Liu, Z. H. Wang, and Y. Pen, "Effects of gefitinib combined with whole brain radiation on brain metastasis from non-small-cell lung cancer," *Chinese Journal of General Practice*, vol. 10, no. 6, pp. 893–895, 2012.
 - [25] D. Zhou, X. Xu, H.-Y. Xie, X.-M. Ma, and Y.-R. Bai, "Therapeutic effects of whole brain radiotherapy with targeted therapy and concomitant chemo-radiotherapy in treatment of non-small-cell lung cancer with brain metastasis," *Journal of Shanghai Jiaotong University*, vol. 33, no. 4, pp. 480–484, 2013.
 - [26] G. A. Pesce, D. Klingbiel, K. Ribi et al., "Outcome, quality of life and cognitive function of patients with brain metastases from non-small cell lung cancer treated with whole brain radiotherapy combined with gefitinib or temozolomide. A randomised phase II trial of the Swiss Group for Clinical Cancer Research (SAKK 70/03)," *European Journal of Cancer*, vol. 48, no. 3, pp. 377–384, 2012.
 - [27] Y. Cai, J.-Y. Wang, and H. Liu, "Clinical observation of whole brain radiotherapy concomitant with targeted therapy for brain metastasis in non-small cell lung cancer patients with chemotherapy failure," *Asian Pacific Journal of Cancer Prevention*, vol. 14, no. 10, pp. 5699–5703, 2013.
 - [28] S. Y. Kim, C. K. Hong, T. H. Kim et al., "Efficacy of surgical treatment for brain metastasis in patients with non-small cell lung cancer," *Yonsei Medical Journal*, vol. 56, no. 1, pp. 103–111, 2015.
 - [29] M. Preusser, D. Capper, A. Ilhan-Mutlu et al., "Brain metastases: pathobiology and emerging targeted therapies," *Acta Neuropathologica*, vol. 123, no. 2, pp. 205–222, 2012.
 - [30] J. R. Johnson, M. Cohen, R. Sridhara et al., "Approval summary for erlotinib for treatment of patients with locally advanced or metastatic non-small cell lung cancer after failure of at least one prior chemotherapy regimen," *Clinical Cancer Research*, vol. 11, no. 18, pp. 6414–6421, 2005.
 - [31] Y. Wang, Y. Wang, B. Wang et al., "Primary result of the efficacy and tolerance of gefitinib in advanced non-small cell lung cancer patients with brain metastasis," *Chinese Journal of Lung Cancer*, vol. 9, no. 5, pp. 447–451, 2006.
 - [32] J. W. Welsh, R. Komaki, A. Amini et al., "Phase II trial of erlotinib plus concurrent whole-brain radiation therapy for patients with brain metastases from non-small-cell lung cancer," *Journal of Clinical Oncology*, vol. 31, no. 7, pp. 895–902, 2013.

- [33] M. Jamal-Hanjani and J. Spicer, "Epidermal growth factor receptor tyrosine kinase inhibitors in the treatment of epidermal growth factor receptor-mutant non-small cell lung cancer metastatic to the brain," *Clinical Cancer Research*, vol. 18, no. 4, pp. 938–944, 2012.
- [34] H.-K. Sun, J.-H. Zheng, and W.-M. Zhang, "Research progress of brain metastasis in non-small cell cancer with different EGFR gene status," *Chinese Journal of Cancer Prevention and Treatment*, vol. 21, no. 10, pp. 795–799, 2014.

Clinical Study

Replanning Criteria and Timing Definition for Parotid Protection-Based Adaptive Radiation Therapy in Nasopharyngeal Carcinoma

Wei-Rong Yao,^{1,2} Shou-Ping Xu,¹ Bo Liu,³ Xiu-Tang Cao,⁴ Gang Ren,⁵ Lei Du,⁶
Fu-Gen Zhou,³ Lin-Chun Feng,^{1,6} Bao-Lin Qu,¹ Chuan-Bin Xie,¹ and Lin Ma^{1,6}

¹Department of Radiation Oncology, Chinese PLA General Hospital, 28 Fuxing Road, Beijing 100853, China

²Department of Oncology, People's Hospital of Jiangxi Province, 92 Aiguo Road, Nanchang 330006, China

³Image Processing Centre, Beihang University, 37 Xueyuan Road, Beijing 100191, China

⁴Department of Medical Statistics, Chinese PLA General Hospital, 28 Fuxing Road, Beijing 100853, China

⁵Department of Radiation Oncology, Air Force General Hospital, 30 Fucheng Road, Beijing 100141, China

⁶Department of Radiation Oncology, Chinese PLA General Hospital, Hainan Branch, Haitang Bay, Sanya 572000, China

Correspondence should be addressed to Lin Ma; malinpharm@sina.com

Received 26 July 2015; Accepted 30 November 2015

Academic Editor: Jan Plzak

Copyright © 2015 Wei-Rong Yao et al. This is an open access article distributed under the Creative Commons Attribution License, which permits unrestricted use, distribution, and reproduction in any medium, provided the original work is properly cited.

The goal of this study was to evaluate real-time volumetric and dosimetric changes of the parotid gland so as to determine replanning criteria and timing for parotid protection-based adaptive radiation therapy in nasopharyngeal carcinoma. Fifty NPC patients were treated with helical tomotherapy; volumetric and dosimetric (D_{mean} , V_1 , and D_{50}) changes of the parotid gland at the 1st, 6th, 11th, 16th, 21st, 26th, 31st, and 33rd fractions were evaluated. The clinical parameters affecting these changes were studied by analyses of variance methods for repeated measures. Factors influencing the actual parotid dose were analyzed by a multivariate logistic regression model. The cut-off values predicting parotid overdose were developed from receiver operating characteristic curves and judged by combining them with a diagnostic test consistency check. The median absolute value and percentage of parotid volume reduction were 19.51 cm³ and 35%, respectively. The interweekly parotid volume varied significantly ($p < 0.05$). The parotid D_{mean} , V_1 , and D_{50} increased by 22.13%, 39.42%, and 48.45%, respectively. The actual parotid dose increased by an average of 11.38% at the end of radiation therapy. Initial parotid volume, initial parotid D_{mean} , and weight loss rate are valuable indicators for parotid protection-based replanning.

1. Background

Due to the anatomical and biological specificity of nasopharyngeal carcinoma (NPC), radiation therapy or chemoradiotherapy has been recognized as a definitive treatment. Studies have shown that the higher the radiation dose delivered to the target volume, the better the local disease control ratio [1]. The escalation of the delivered dose, however, often leads to severe and related side-effects. Xerostomia is one of the most frequent side-effects and the amount of radiation that is delivered to the parotid glands, assuming a major role in stimulating salivary flow, affects NPC patients' quality of life. Therefore, when treating NPC it is crucial

to minimize the dose to the parotid glands while ensuring adequate dose distribution to the target volumes. Unlike two-dimensional conventional radiation therapy (2DCRT) and three-dimensional conformal radiation therapy (3DCRT), intensity modulated radiation therapy (IMRT) can deliver a highly conformal dose to targets while effectively sparing critical normal organs, potentially improving the local control rate and reducing radiation-related toxicities [2–5].

Patients with head and neck cancer may be subjected to significant anatomical changes during radiation therapy, changes which can cause volume shrinkage near the facial surface [6–8]. And parotid gland variations may result in an unanticipated overdose [9, 10]. Replanning during radiation

therapy can correct these anatomical changes and protect parotid glands from an overdose of irradiation [10–12]. However, the indications and timing of replanning are still unknown.

Helical tomotherapy (HT) is a unique IMRT modality that combines elements of diagnostic radiology and radiation therapy in a single unit. In addition to its ability to deliver a highly conformal dose distribution, HT is equipped with xenon detectors that have been designed to obtain the megavoltage computed tomography (MVCT) images that are used for pretreatment set-up verification and actual dose detection [13]. In the previous study, we evaluated weekly anatomical and dosimetric changes of the parotid gland in 35 NPC patients treated with HT system and found that some patients' parotid volumes and locations varied significantly, generally causing an increase of the actual delivered dose [14]. It is thus necessary to identify relevant factors that affect these changes. We performed this study in order to evaluate the real-time volumetric and dosimetric changes of the parotid gland and thus determine the replanning cut-off values for parotid protection-based adaptive radiation therapy (ART) in NPC.

2. Materials and Methods

2.1. Patients. We pooled data from the 100 parotid glands of 50 NPC patients that were treated with the TomoTherapy Hi-Art Treatment System (Accuray, Sunnyvale, CA). The patients were all initially diagnosed, histologically proven, and had a median age of 44 years (range: 11–80 years). Thirty of the 50 patients received platinum-based chemotherapy, and 20 others received only radiation therapy. Informed consent was obtained from all patients before receiving treatment. The main patient characteristics are summarized in Table 1.

2.2. Delineation and the Dose to Target Volumes and Organs at Risk (OARs). The process of CT simulation and the delineation of targets and OARs have been previously reported [14]. Briefly, the gross target volume of the primary tumor (GTVnx) and metastatic lymph nodes (GTVnd) were, respectively, defined as the visible tumor and involved nodes. The pGTVnx was obtained by expanding the corresponding GTVnx by a margin of 3–5 mm and being limited by the brainstem, spinal cord, optic chiasma, and optic nerve. The pGTVnd was the GTVnd with an expansion of 3 mm. CTV₁ covered the high-risk clinical target volume, and CTV₂ included the low-risk clinical target volume. Each CTV was automatically expanded in order to generate the corresponding planning target volume (PTV) with an isotropic 3 mm margin, while assuring that the edge of the distribution was at least 2 mm from the skin. The contour of parotid glands referred to the standard of van de Water et al. [15].

Treatment planning was made on the TomoTherapy Hi-Art 2.2.4.1 workstation. Treatment was delivered in 33 fractions to the primary tumor and metastatic nodes (pGTVnx and pGTVnd) for a total of 70 Gy, while the PTV1 and PTV2 received 60 Gy and 56 Gy, respectively. The following dose-volume constraints for OARs were utilized: brainstem $D_{\max} < 54$ Gy, lens $D_{\max} < 5$ Gy, optic nerve $D_{\max} < 54$ Gy, spinal

TABLE 1: Patient characteristics.

Characteristics	Number of patients	Percent (%)
Gender		
Male	40	80
Female	10	20
Age	11–80 years (median, 44 years)	
UICC stage (2002)		
T		
1	13	26
2	16	32
3	13	26
4	8	16
N		
0	18	36
1	15	30
2	15	30
3	2	4
M		
0	50	100
Treatment method		
RT	20	40
CCRT	13	26
ICT + CCRT	17	34
Primary tumor volume	37.54 ± 25.23 (4.36–118.00) cm ³	
Volume of metastatic nodes	13.15 ± 23.18 (0–133.35) cm ³	
Weight loss rate at the end of RT	10.80 ± 4.12%	

RT: radiation therapy; CCRT: concurrent chemoradiotherapy; ICT: induced chemotherapy.

cord $D_{\max} < 45$ Gy, temporomandibular joint $D_{\max} < 60$ Gy, inner ear $D_{\max} < 60$ Gy, parotid gland $V_{30} < 50\%$, oral cavity $V_{40} < 30\%$, and larynx-oesophagus-trachea $V_{40} < 30\%$.

2.3. Anatomical and Dosimetric Measurements of the Parotid Gland. HT's adaptive software calculated the volume and actual dose distribution according to the pretreatment MVCT scanning [14]. The MVCT images of the first fraction were collected, followed by additional 7 fractions (fractions numbers 6, 11, 16, 21, 26, 31, and 33) for a total of 8 series of images. According to previously noted setup errors, each patient's MVCT images were merged with each patient's corresponding KVCT images using the adaptive software. The same physician manually contoured the parotid glands of each patient on the MVCT images. According to the contoured images, the actual single fraction dose-volume histograms (DVHs) of the parotid gland were gained in the adaptive software. Variations in parotid volume, D_{mean} (mean dose), V_1 (the volume receiving ≥ 1 Gy), and D_{50} (the dose delivered to 50% of the volume) of each fraction were extracted from the DVH gained from the Planned Adaptive application software. The ipsilateral and contralateral parotid glands were analyzed separately.

TABLE 2: Correlations of factors with parotid (actual) volume and dose.

Factor	Volume (<i>p</i> value)	D_{mean} (<i>p</i> value)	V_1 (<i>p</i> value)	D_{50} (<i>p</i> value)
Age	0.683	0.858	0.846	0.743
T stage	0.690	0.862	0.883	0.716
N stage	0.044	0.439	0.607	0.413
Volume of primary tumor	0.712	0.422	0.689	0.093
Volume of metastatic nodes	0.086	0.463	0.521	0.308
Treatment method	0.061	0.059	0.031	0.039
Initial parotid volume	0.000	0.205	0.241	0.254
Initial parotid D_{mean}	0.549	0.226	0.286	0.002
Weight loss rate	0.036	0.000	0.004	0.014
Reduction of skin separation at C1 level	0.000	0.000	0.000	0.000
Reduction of skin separation at C2 level	0.010	0.000	0.000	0.013
Reduction of skin separation at C4 level	0.042	0.090	0.110	0.271

In order to assess the cumulative dosimetric differences, all data from the 8 fractions were imported as DICOM files into the computational environment for radiotherapy (CERR) [16, 17]. The cumulative delivered dose over the entire treatment course was assessed from the sum of the 8 weekly MVCT images. The total delivered dose was then evaluated on the MVCT images of the 16th fraction using the cumulated dose information from the intermediate weekly scanning images.

Anatomical parameters such as skin separation were determined on the original KVCT and MVCT images. The skin separations at the level of the odontoid processes of the C2 vertebra and the intervertebral foramina of the C1 and C4 vertebrae were used to assess the anatomical changes. Patient characteristics (e.g., age, gender, weight loss, tumor stage, primary tumor volume, total volume of metastatic nodes, initial D_{mean} , and initial parotid volume) were collected and analyzed.

2.4. Statistical Analysis. Statistical analyses were performed using repeated measures analysis of variance, Pearson correlation calculations, logistic multivariate regression analysis, and receiver operating characteristic (ROC) analysis by SPSS 17.0 (SPSS Inc., Chicago, IL, USA). To determine the effectiveness of replanning cut-off values in ROC analysis, the consistency test was performed. All statistical tests were performed two-sided and a *p* value of <0.05 was considered to indicate statistical significance.

3. Results

3.1. Anatomical Changes. The average weight loss rate during radiation therapy was 10.66% (range, 3–21%). Inter-weekly weight variations had statistical differences. Significant changes in skin separations between the first and last fractions at the level of the odontoid processes of C2 and that of the intervertebral foramina of the C1 and C4 vertebrae were observed. Separations at the C1, C2, and C4 levels averaged –11.05%, –11.23%, and –13.29%, respectively. Reductions in

skin separations were smooth during the course of radiation therapy and no plateau was found. Weight loss rates had a moderate-to-strong correlation with reductions in skin separation at the C1, C2, and C4 levels ($r = 0.568$, $p = 0.000$; $r = 0.441$, $p = 0.017$; $r = 0.480$, $p = 0.010$; resp.).

In our cohort, the data of 100 parotid glands were evaluated. The median absolute value and percentage of parotid volume reduction were 19.51 cm³ (range, 6.58–40.26 cm³) and 35% (range, 6.80–69.44%), respectively. The median parotid volume reduction was 1.07%/d of the initial volume. No differences were found between the ipsilateral and the contralateral parotid glands.

3.2. Dosimetric Findings. Parotid dosimetric parameters of the 8 fractions during radiation therapy included D_{mean} , D_{50} , and V_1 . The increasing rates of parotid D_{mean} , V_1 , and D_{50} were 22.13%, 39.42%, and 48.45%, respectively. The variation trend of these dosimetric parameters between the ipsilateral and contralateral parotids was almost the same. The total cumulative parotid dose was also estimated. The initial average D_{mean} of 100 parotid glands was 30.28 Gy, while the cumulative average D_{mean} at the end of radiation therapy, as estimated by CERR, was 33.8 Gy, an increase of 11.38%. It is worth noting that increases in parotid dose were very individual and varied, as shown by the fact that cumulative parotid doses ranged from –1.51% to 30.57%.

3.3. Factors Affecting Parotid Volumetric and Dosimetric Changes. A summary of the relevant potential predictive factors for parotid volumetric and dosimetric changes is given in Table 2. Single-factor repetitive measurement analysis was performed. The most consistent predictive factor was the variation rate of skin separation. Reductions in skin separation at the C1 and C2 levels predicted a decrease in parotid volume and an increase in delivered dose to the parotid glands ($p = 0.000$ and $p < 0.05$, resp.). Weight loss rate was another predictive factor for volumetric and dosimetric changes (including the D_{mean} , V_1 , and D_{50} of each of the 8 fractions) in the parotid glands ($p < 0.05$). The

TABLE 3: AUC and cut-off values in ROC analysis.

Parameter	AUC value	Cut-off value
Initial parotid volume	0.570	52.80 cm ³
Initial parotid D_{mean}	0.566	32.04 Gy
Weight loss rate	0.568	12.24%
Weight loss rate at 11th fraction	0.662	2.30%
Weight loss rate at 16th fraction	0.597	3.60%
Weight loss rate at 21st fraction	0.575	4.40%

N stage and initial parotid volume affected the variation in parotid volume during radiation therapy ($p = 0.044$ and $p = 0.000$, resp.). Different treatment modalities affected the variations of V_1 and D_{50} ($p = 0.031$ and $p = 0.039$, resp.); patients who received concurrent chemoradiotherapy had larger variations of V_1 and D_{50} . The initial parotid D_{mean} affected the variation of D_{50} ($p = 0.002$). Age, T stage, primary tumor volume, volume of metastatic nodes, and area of metastatic nodes did not affect parotid volumetric and dosimetric parameters.

3.4. Possible Prognostic Factors of Replanning. We wondered whether clinical characteristics and some externally measurable parameters, including anatomical changes, could predict the necessity of replanning. In our research, replanning was thus based on the anatomical and dosimetric parameters of the parotid gland. At the end of radiation therapy, if the cumulative actual parotid dose was more than 10% of the initial planning dose, replanning was considered to be necessary. Multivariate logistic regression analysis indicated that initial parotid volume, initial parotid D_{mean} , and weight loss rate were significant predictive parameters for the increase of actual parotid dose ($p < 0.05$). In other words, these 3 parameters were possible prognostic factors for parotid protection-based replanning.

3.5. Candidate Cut-Off Values of Replanning. ROC curves were used to establish replanning cut-off values. The 3 parameters (initial parotid volume, initial parotid D_{mean} , and weight loss rate) that were filtered from logistic analysis were used in ROC analysis. The area under the curve (AUC) and cut-off values of these parameters are shown in Table 3. To predict the necessity of replanning during treatment, weight loss rates at the 11th, 16th, and 21st fractions were used in ROC analysis. The AUC and cut-off values are shown in Table 3.

When these 3 parameters were used independently, they had weak predictive power for replanning ($0.5 < \text{AUC} < 0.7$) (see Table 4). To improve their predictive power, we performed a multivariate consistency check. These parameters were combined together in two ways: first, 2 of the 3 parameters reached the cut-off values; second, all 3 parameters reached the cut-off values. The results of the multivariate consistency check showed that when 2 of the 3 parameters reached the cut-off values, their predictive power was better than another combination modality (Table 5). In other words, at the 11th, 16th, and 21st fraction, when 2 of the 3 parameters including initial parotid volume, initial parotid D_{mean} , and weight loss rate reach their cut-off values, the possibility of

overdose in the parotid gland is high and the patient should then receive a replanning.

4. Discussion

In recent years there has been great interest in highly conformal radiation technologies with steep dose gradients between tumor and normal structures, such as IMRT, and their ability to reduce the side-effects of radiation therapy, including xerostomia, in head and neck cancer [18]. As parotid glands produce approximately 60% of saliva and their anatomical changes during radiation therapy may have significant dosimetric implications, parotid protection-based ART has become a hot field of study in head and neck cancer IMRT [19, 20]. In this study, we attempted to quantify the effect of anatomical changes on parotid dosimetry and to detect the factors that affect the actual dose that is delivered to the parotid gland. On the basis of these data, we screened out 3 cut-off values which could predict the need for replanning in parotid protection-based ART in NPC.

As shown by published studies, parotid volume decreases when the gland migrates into the high-dose volume during radiation therapy for NPC patients, leading to a higher actual parotid dose than was intended in the initial planning [8, 14]. In our study we observed that the actual parotid D_{mean} increased, as well as V_1 and D_{50} , after a single fraction. We also found that the magnitude of the dosimetric changes varied among our different patients, suggesting that not all NPC patients need a replanning. Recently, Hunter et al. [21] treated 18 oropharyngeal cancer patients. In order to calculate their cumulative delivered doses, parotid glands in cone-beam CT (CBCT) images were aligned by deformable registration. Stimulated salivary flow rates were measured before therapy and, periodically, after therapy. The outcomes suggested that, in most cases, ART was not likely to improve measurable salivary output. However, the researchers admitted that the residual setup error was still largely responsible for causing the dosimetric deviation that occurred after CBCT image guidance was used to correct the translational setup. Additionally, when researching the effect of adaptive replanning on locoregional control, Zhao et al. [22] and Chen et al. [23] argued that routine replanning was probably not necessary but still suggested that there would be a significant benefit if appropriate patients were selected.

In our study we screened for certain factors that would predict dosimetric variations in NPC patients during radiation therapy. Parameters such as age, T/N stage, tumor volume, initial parotid volume, weight loss rate, and reduction of facial skin separation were analyzed using correlation and logistic multivariate regression analyses. Weight loss rate was detected to be one of the most important parameters to correlate with the variation of actual parotid dose. Similar to our results, Hansen et al. [24] performed a retrospective chart review for 13 head and neck cancer patients who were treated with IMRT and received repeat CT imaging and replanning when weight loss became obvious during treatment. They showed that weight loss amplified the actual dose variation to normal tissue and bone (including the spinal cord, parotid glands, and mandible) and increased the D_{mean} , D_{50} , and V_{26}

TABLE 4: Consistency check of single factors.

Parameter	Sensitivity (%)	Specificity (%)	Positive predictive value (%)	Negative predictive value (%)	Kappa value	<i>p</i> value
Initial parotid volume > 52.80 cm ³	73.1	41.7	57.6	58.8	0.149	0.27
Initial parotid D_{mean} > 32.04 Gy	42.3	79.2	68.8	55.9	0.211	0.10
Weight loss rate at 11th fraction > 2.30%	50.0	66.7	61.9	55.2	0.165	0.23
Weight loss rate at 16th fraction > 3.60%	57.7	54.2	57.7	54.2	0.119	0.40
Weight loss rate at 21st fraction > 4.40%	73.1	25	56.4	41.2	0.200	0.88

TABLE 5: Consistency check of multiple factors.

Fraction number and combination	Sensitivity (%)	Specificity (%)	Positive predictive value (%)	Negative predictive value (%)	Kappa value	<i>p</i> value
Number 11						
a	69.2	66.7	69.2	66.7	0.359	0.011
b	87.5	52.4	25.9	91.7	0.143	0.155
Number 16						
a	66.7	65.2	69.2	62.5	0.320	0.025
b	77.8	53.7	26.9	91.7	0.181	0.087
Number 21						
a	84.6	54.2	66.7	76.5	0.392	0.004
b	44.0	95.7	91.7	61.1	0.388	0.002

a: two of the 3 parameters (initial parotid volume, initial parotid D_{mean} , and weight loss rate) reached their cut-off values.

b: all the 3 parameters reached their cut-off values.

of the right parotid gland. They also suggested that weight loss might have a stronger impact on dosimetric changes than tumor shrinkage. Chen et al. [25] also found that weight loss caused significant dosimetric changes of targets and OARs in NPC patients treated with IMRT and believed that repeated scanning and replanning for patients with an obvious weight loss might be necessary. Our study's data also showed that weight loss during radiation therapy could forecast overdose to the parotid gland.

The timing of replanning is a controversial topic in parotid protection-based ART in head and neck cancer. Someone recommended replanning when it became obvious that a tumor had shrunk, weight loss had occurred, or skin separation had reduced [7, 11, 12, 21–23], while others believe that replanning should be performed when a specific fraction has been reached [26–28]. Our previous study found that parotid volume variation presented a linear pattern throughout IMRT of NPC realized by HT technique, and the rate of volume variation reached its peak at the 16th fraction and then decreased gradually, suggesting that replanning is appropriate in the fourth week [14]. In this study, we raised the specific criteria coupled with timing of replanning for parotid protection-based ART in NPC. The criteria consisted of 3

parameters: (1) an initial parotid volume of > 52.80 cm³; (2) an initial parotid D_{mean} of > 32.04 Gy; (3) a weight loss rate at the 11th fraction of > 2.3%, a weight loss rate at the 16th fraction of > 3.6%, or a weight loss rate at the 21st fraction of > 4.4%. If the patient reached 2 of these 3 parameters, the parotid gland would likely to be overdosed and a replanning was recommended at the current fraction of radiation therapy. Recently, Brown et al. [29] analyzed 110 patients with oropharyngeal squamous cell carcinoma and NPC. Patient demographics and tumor characteristics were compared between patients who were replanned and those that were not. Nodal disease stage, pretreatment of largest involved node size, diagnosis, and initial weight were identified as being significant for inclusion in the predictive model and ART risk profiles. However, among the 110 patients, only 5 had replanning, suggesting a low credibility of their model. Castelli et al. [30] estimated the parotid overdose and the xerostomia risk increase during IMRT with weekly CTs and replanning in 15 patients with locally advanced head and neck cancer. Parotid cumulated doses were estimated for the two scenarios, with or without replanning, using deformable image registration. Compared to the initial planning, a parotid overdose was observed in 59% of the parotid glands, with an average

D_{mean} increase of 3.7 Gy. The parotid overdose increased with the tumor shrinkage and the neck thickness reduction. Weekly replanning decreased the parotid D_{mean} by 5.1 Gy and the absolute risk of xerostomia by 11%. However, weekly replanning consumes a large amount of medical resources and is difficult to be routinely applied.

Our criteria have at least 3 advantages. First, the parameters involved in our criteria address the combination of factors that correlate with actual volumetric and dosimetric variations in the parotid gland. We evaluated the predictive factors of these variations, screened out some parameters which could predict parotid overdose by logistic stepwise regression analysis, used ROC analysis to obtain the cut-off values of these parameters, and then used single- and multiple-factor consistency tests to confirm the predictive value of these parameters in order to combine them as replanning criteria. Hansen et al. [24] carried out replanning when obvious tumor shrinkage and/or weight loss were noted but did not clarify the replanning thresholds of these 2 parameters. A similarly ambiguous replanning standard was seen in the research of Zhao et al. [22] who compared the treatment results of replanning and no replanning in NPC patients. Recently, Lee et al. [31] studied the tumor volume reduction rate (TVRR) during radiation therapy and found that TVRR was a prognosticator of locoregional disease control in patients with oropharyngeal cancer. To ensure locoregional control, they suggested a few therapeutic modifications that were based on TVRR. Second, our parameters reflect patients' individual characteristics. As the initial parotid volume reflects the condition of the parotid gland before treatment, the initial parotid D_{mean} reflects how initial planning and weight loss rate correlate with the variation degree of parotid anatomical and dosimetric changes during radiation therapy. Our criteria are more comprehensive than those which paid more attention to anatomical changes but less attention to the initial conditions of the parotid gland. Initial conditions of the parotid gland, such as its initial volume and D_{mean} , have since been confirmed to relate to the variation of parotid dose [32]. Fiorentino et al. [26] used CBCT images to analyze the parotid volume of 10 patients with head and neck cancer during radiation therapy and suggested that replanning should be performed during the third week. However, the individual conditions in our study patients make it clear that replanning at the same time point is not suitable for every patient. Third, the parameters of our criteria are easy to measure, even without repeated CT scanning during treatment. Specifically, the initial volume and D_{mean} of the parotid gland can be evaluated from simulation CT images and initial planning and weight loss rate can be measured easily during treatment, unlike other parameters such as facial skin separation which is only measurable by repeated CT imaging during treatment.

However, taking into account the complexity of ART, the cut-off values raised in our study have some limitations. First, these cut-off values are based on the possibility of an overdose to the parotid gland and can thus only be used to protect the parotid gland. They cannot be used to protect the other OARs or correct for an underdose to a tumor target which may not be correlated with volumetric changes. The study of Yan et al.

[33] showed that GTV volume reduction was negatively correlated with the apparent diffusion coefficient (ADC) values of pretreatment tumors but not pretreatment tumor volume, and CTV volume reduction was correlated with pretreatment body mass index (BMI). Second, delineation of the parotid gland affects the use of these cut-off values. For example, when the deep lobe of the parotid gland is not contoured, our criteria will not be suitable for replanning prediction. Third, deformable registration was not used in this study. Deformable registration is being increasingly used in ART research, not only in anatomical registration but also in dose calculation [21, 30, 34–36]. We are developing home-made deformable registration software and will compare its results with those from this study. Fourth, if the initial parotid volume and D_{mean} are all above the cut-off values, the patient is suitable for replanning, though it is not clear when that should happen.

5. Conclusions

During the IMRT of NPC, the actual volume and dose of the parotid gland vary significantly in some patients. The initial volume and mean dose of the parotid gland and body weight loss rate are the most significant predictors for these variations. Replanning is suggested if these parameters reach the cut-off values recommended in this paper.

Conflict of Interests

There is no conflict of interests in connection with this work.

Authors' Contribution

All of the authors participated in the design, execution, and analysis of this work. Wei-Rong Yao and Gang Ren participated in acquisition of data, performed the statistical analysis, and helped to write the paper. Shou-Ping Xu and Chuan-Bin Xie contributed to data analysis. Bo Liu and Fu-Gen Zhou contributed to image processing. Xiu-Tang Cao was responsible for statistical analysis instruction of data. Lei Du, Lin-Chun Feng, and Bao-Lin Qu participated in acquisition of data. Lin Ma was responsible for study conception and design, participated in acquisition of data, and drafted the paper. All authors read and approved the final paper.

Acknowledgment

This work was supported by Grant no. 2009-2036 from the Foundation for Capital Medical Development.

References

- [1] P. M. L. Teo, S. F. Leung, S. Y. Tung et al., "Dose-response relationship of nasopharyngeal carcinoma above conventional tumoricidal level: a study by the Hong Kong nasopharyngeal carcinoma study group (HKNPCSG)," *Radiotherapy & Oncology*, vol. 79, no. 1, pp. 27–33, 2006.

- [2] N. Lee, J. Harris, A. S. Garden et al., "Intensity-modulated radiation therapy with or without chemotherapy for nasopharyngeal carcinoma: radiation therapy oncology group phase II trial 0225," *Journal of Clinical Oncology*, vol. 27, no. 22, pp. 3684–3690, 2009.
- [3] S. Lin, J. J. Lu, L. Han, Q. Chen, and J. Pan, "Sequential chemotherapy and intensity-modulated radiation therapy in the management of locoregionally advanced nasopharyngeal carcinoma: experience of 370 consecutive cases," *BMC Cancer*, vol. 10, pp. 39–47, 2010.
- [4] S.-F. Su, F. Han, C. Zhao et al., "Long-term outcomes of early-stage nasopharyngeal carcinoma patients treated with intensity-modulated radiotherapy alone," *International Journal of Radiation Oncology Biology Physics*, vol. 82, no. 1, pp. 327–333, 2012.
- [5] G. Peng, T. Wang, K.-Y. Yang et al., "A prospective, randomized study comparing outcomes and toxicities of intensity-modulated radiotherapy vs. conventional two-dimensional radiotherapy for the treatment of nasopharyngeal carcinoma," *Radiotherapy & Oncology*, vol. 104, no. 3, pp. 286–293, 2012.
- [6] J. L. Barker Jr., A. S. Garden, K. K. Ang et al., "Quantification of volumetric and geometric changes occurring during fractionated radiotherapy for head-and-neck cancer using an integrated CT/linear accelerator system," *International Journal of Radiation Oncology Biology Physics*, vol. 59, no. 4, pp. 960–970, 2004.
- [7] L. Capelle, M. Mackenzie, C. Field, M. Parliament, S. Ghosh, and R. Scrimger, "Adaptive radiotherapy using helical tomotherapy for head and neck cancer in definitive and postoperative settings: initial results," *Clinical Oncology*, vol. 24, no. 3, pp. 208–215, 2012.
- [8] C. Han, Y.-J. Chen, A. Liu, T. E. Schultheiss, and J. Y. C. Wong, "Actual dose variation of parotid glands and spinal cord for nasopharyngeal cancer patients during radiotherapy," *International Journal of Radiation Oncology Biology Physics*, vol. 70, no. 4, pp. 1256–1262, 2008.
- [9] T. Nishi, Y. Nishimura, T. Shibata, M. Tamura, N. Nishigaito, and M. Okumura, "Volume and dosimetric changes and initial clinical experience of a two-step adaptive intensity modulated radiation therapy (IMRT) scheme for head and neck cancer," *Radiotherapy & Oncology*, vol. 106, no. 1, pp. 85–89, 2013.
- [10] R.-H. Wang, S.-X. Zhang, L.-H. Zhou et al., "Volume and dosimetric variations during two-phase adaptive intensity-modulated radiotherapy for locally advanced nasopharyngeal carcinoma," *Bio-Medical Materials and Engineering*, vol. 24, no. 1, pp. 1217–1225, 2014.
- [11] D. L. Schwartz, A. S. Garden, J. Thomas et al., "Adaptive radiotherapy for head-and-neck cancer: initial clinical outcomes from a prospective trial," *International Journal of Radiation Oncology Biology Physics*, vol. 83, no. 3, pp. 986–993, 2012.
- [12] D. L. Schwartz, A. S. Garden, S. J. Shah et al., "Adaptive radiotherapy for head and neck cancer—dosimetric results from a prospective clinical trial," *Radiotherapy & Oncology*, vol. 106, no. 1, pp. 80–84, 2013.
- [13] K. M. Langen, S. L. Meeks, D. O. Poole et al., "The use of megavoltage CT (MVCT) images for dose recomputations," *Physics in Medicine and Biology*, vol. 50, no. 18, pp. 4259–4276, 2005.
- [14] G. Ren, S. P. Xu, L. Du et al., "Actual anatomical and dosimetric changes of parotid glands in nasopharyngeal carcinoma patients during intensity modulated radiation therapy," *BioMed Research International*, vol. 2015, Article ID 670327, 6 pages, 2015.
- [15] T. A. van de Water, H. P. Bijl, H. E. Westerlaan, and J. A. Langendijk, "Delineation guidelines for organs at risk involved in radiation-induced salivary dysfunction and xerostomia," *Radiotherapy & Oncology*, vol. 93, no. 3, pp. 545–552, 2009.
- [16] J. O. Deasy, A. I. Blanco, and V. H. Clark, "CERR: a computational environment for radiotherapy research," *Medical Physics*, vol. 30, no. 5, pp. 979–985, 2003.
- [17] M. N. Duma, S. Kampf, T. Schuster, C. Winkler, and H. Geinitz, "Adaptive radiotherapy for soft tissue changes during helical tomotherapy for head and neck cancer," *Strahlentherapie und Onkologie*, vol. 188, no. 3, pp. 243–247, 2012.
- [18] Y. Li, J. M. G. Taylor, R. K. Ten Haken, and A. Eisbruch, "The impact of dose on parotid salivary recovery in head and neck cancer patients treated with radiation therapy," *International Journal of Radiation Oncology Biology Physics*, vol. 67, no. 3, pp. 660–669, 2007.
- [19] S. A. Bhide, M. Davies, K. Burke et al., "Weekly volume and dosimetric changes during chemoradiotherapy with intensity-modulated radiation therapy for head and neck cancer: a prospective observational study," *International Journal of Radiation Oncology Biology Physics*, vol. 76, no. 5, pp. 1360–1368, 2010.
- [20] P. H. Ahn, C.-C. Chen, A. I. Ahn et al., "Adaptive planning in intensity-modulated radiation therapy for head and neck cancers: single-institution experience and clinical implications," *International Journal of Radiation Oncology Biology Physics*, vol. 80, no. 3, pp. 677–685, 2011.
- [21] K. U. Hunter, L. L. Fernandes, K. A. Vineberg et al., "Parotid glands dose-effect relationships based on their actually delivered doses: implications for adaptive replanning in radiation therapy of head-and-neck cancer," *International Journal of Radiation Oncology Biology Physics*, vol. 87, no. 4, pp. 676–682, 2013.
- [22] L. Zhao, Q. Wan, Y. Zhou, X. Deng, C. Xie, and S. Wu, "The role of replanning in fractionated intensity modulated radiotherapy for nasopharyngeal carcinoma," *Radiotherapy and Oncology*, vol. 98, no. 1, pp. 23–27, 2011.
- [23] A. M. Chen, M. E. Daly, J. Cui, M. Mathai, S. Benedict, and J. A. Purdy, "Clinical outcomes among patients with head and neck cancer treated by intensity-modulated radiotherapy with and without adaptive replanning," *Head & Neck*, vol. 36, no. 11, pp. 1541–1546, 2014.
- [24] E. K. Hansen, M. K. Bucci, J. M. Quivey, V. Weinberg, and P. Xia, "Repeat CT imaging and replanning during the course of IMRT for head-and-neck cancer," *International Journal of Radiation Oncology Biology Physics*, vol. 64, no. 2, pp. 355–362, 2006.
- [25] C. Chen, Z. Fei, L. Chen, P. Bai, X. Lin, and J. Pan, "Will weight loss cause significant dosimetric changes of target volumes and organs at risk in nasopharyngeal carcinoma treated with intensity-modulated radiation therapy?" *Medical Dosimetry*, vol. 39, no. 1, pp. 34–37, 2014.
- [26] A. Fiorentino, R. Caivano, V. Metallo et al., "Parotid gland volumetric changes during intensity-modulated radiotherapy in head and neck cancer," *The British Journal of Radiology*, vol. 85, no. 1018, pp. 1415–1419, 2012.
- [27] W. W. K. Fung, V. W. C. Wu, and P. M. L. Teo, "Developing an adaptive radiation therapy strategy for nasopharyngeal carcinoma," *Journal of Radiation Research*, vol. 55, no. 2, pp. 293–304, 2014.
- [28] K. Brock, C. Lee, S. Samuels et al., "TU-AB-303-05: clinical guidelines for determining when an adaptive replan may be

- warranted for head and neck patients,” *Medical Physics*, vol. 42, no. 6, article 3590, 2015.
- [29] E. Brown, R. Owen, F. Harden et al., “Predicting the need for adaptive radiotherapy in head and neck cancer,” *Radiotherapy & Oncology*, vol. 116, no. 1, pp. 57–63, 2015.
- [30] J. Castelli, A. Simon, G. Louvel et al., “Impact of head and neck cancer adaptive radiotherapy to spare the parotid glands and decrease the risk of xerostomia,” *Radiation Oncology*, vol. 10, no. 1, article 6, 2015.
- [31] H. Lee, Y. C. Ahn, D. Oh, H. Nam, Y. I. Kim, and S. Y. Park, “Tumor volume reduction rate measured during adaptive definitive radiation therapy as a potential prognosticator of locoregional control in patients with oropharyngeal cancer,” *Head & Neck*, vol. 36, no. 4, pp. 499–504, 2014.
- [32] S. Broggi, C. Fiorino, I. Dell’Oca et al., “A two-variable linear model of parotid shrinkage during IMRT for head and neck cancer,” *Radiotherapy & Oncology*, vol. 94, no. 2, pp. 206–212, 2010.
- [33] D. Yan, S. Yan, Q. Wang, X. Liao, Z. Lu, and Y. Wang, “Predictors for replanning in loco-regionally advanced nasopharyngeal carcinoma patients undergoing intensity-modulated radiation therapy: a prospective observational study,” *BMC Cancer*, vol. 13, pp. 548–556, 2013.
- [34] A. Kumarasiri, F. Siddiqui, C. Liu et al., “Deformable image registration based automatic CT-to-CT contour propagation for head and neck adaptive radiotherapy in the routine clinical setting,” *Medical Physics*, vol. 41, no. 12, Article ID 121712, 2014.
- [35] X. Gu, B. Dong, J. Wang et al., “A contour-guided deformable image registration algorithm for adaptive radiotherapy,” *Physics in Medicine and Biology*, vol. 58, no. 6, pp. 1889–1901, 2013.
- [36] J. Lu, Y. Ma, J. Chen et al., “Assessment of anatomical and dosimetric changes by a deformable registration method during the course of intensity-modulated radiotherapy for nasopharyngeal carcinoma,” *Journal of Radiation Research*, vol. 55, no. 1, pp. 97–104, 2014.

Clinical Study

Volumetric Modulated Arc Therapy of the Pelvic Lymph Nodes to the Aortic Bifurcation in Higher Risk Prostate Cancer: Early Toxicity Outcomes

**Gina Hesselberg,^{1,2} Gerald Fogarty,^{3,4,5} Lauren Haydu,⁴
Nicole Dougheney,³ and Phillip Stricker⁵**

¹Prince of Wales Hospital, High Street, Randwick, NSW 2031, Australia

²University of New South Wales, High Street, Kensington, NSW 2052, Australia

³Genesis Cancer Care, Mater Sydney Radiation Oncology, 25 Rocklands Road, Crows Nest, NSW 2065, Australia

⁴University of Texas MD Anderson Cancer Center, Surgical Oncology, 1400 Pressler Street, FCT 176000, Houston, TX, USA

⁵St Vincent's Hospital, 390 Victoria Street, Darlinghurst, NSW 2010, Australia

Correspondence should be addressed to Gerald Fogarty; gerald.fogarty@cancer.com.au

Received 31 March 2015; Revised 17 June 2015; Accepted 21 June 2015

Academic Editor: Yuanming Feng

Copyright © 2015 Gina Hesselberg et al. This is an open access article distributed under the Creative Commons Attribution License, which permits unrestricted use, distribution, and reproduction in any medium, provided the original work is properly cited.

Background. Treatment of pelvic lymph nodes (PLNs) in higher risk prostate carcinoma is controversial. The primary focus of the study was to evaluate the early toxicity profile for this cohort of patients treated with Volumetric Modulated Arc Therapy (VMAT). **Methods.** Patient, tumour, and treatment characteristics of those who received VMAT from May 2010 to December 2012 were analysed. A simplified contouring process of the PLNs to the aortic bifurcation was developed based on consensus guidelines. Acute and late genitourinary (GU) and gastrointestinal (GI) toxicities were documented according to the Radiation Therapy Oncology Group (RTOG) Version 2 Guidelines. Successive Prostate Specific Antigen (PSA) values after treatment were measured on average 3 months apart. **Results.** 113 patients were treated between May 2010 to December 2012 with a median follow-up of 14 months. No patients experienced acute grade 3 or 4 GU and GI toxicity. Only 1 patient experienced a late grade 3 GU complication. No late grade 4 GU or GI events have yet occurred. **Conclusions.** This study reviews the first Australian experience of VMAT in the treatment of pelvic lymph nodes in prostate cancer, specifically to the level of the aortic bifurcation. It demonstrates a favorable acute toxicity profile whilst treating large PLN volumes with optimal dose coverage.

1. Introduction

Prostate cancer is the most commonly diagnosed cancer in Australian males with an incidence of approximately 18,500 new cases per annum [1]. Management options for prostate cancer include radical prostatectomy (RP), radiotherapy (RT), androgen deprivation therapy (ADT), active surveillance, or a combination of these. The question of whether pelvic lymph nodes (PLN) should be treated in intermediate and high-risk settings with either surgery or radiotherapy is controversial. Two seminal phase III trials (RTOG 9413 and GETUG-01) reached conflicting conclusions [2, 3]. Additionally, no randomized trial has yet shown a survival advantage. Retrospective surgical series have demonstrated

lower biochemical failure (BF) rates (defined as prostate specific antigen (PSA) greater than 0.2 ng/mL) in patients undergoing extended pelvic lymph node dissection [4]. This is applicable to patient populations with either clinically node negative disease [4] or low volume of nodal involvement [5]. Morikawa and Roach explore why some of these studies were negative in demonstrating a benefit of whole pelvic radiotherapy (WPRT) and conclude that predictions of nodal disease based on surgical series may in fact underestimate the true extent of involvement [6].

Consensus guidelines on pelvic lymph node clinical target volumes (CTV) in the setting of high-risk prostate cancer have been published to enable uniformity and accuracy in WPRT [7, 8]. Intensity modulated radiotherapy (IMRT)

enhances treatment dose conformality [9]. This enables dose escalation to the clinical target volume whilst decreasing dose to surrounding normal tissue, thereby increasing the therapeutic ratio [9–11]. Volumetric modulated arc therapy (VMAT) has been shown in the Australian context to be superior to 3D conformal radiotherapy (3D-CRT) and step and shoot IMRT in terms of dose-volume histogram coverage of planning target volumes (PTVs) and organs at risk (OARs) [12]. Additionally VMAT is a further evolution of IMRT, enabling more efficient treatment [12]. VMAT can be utilized in the treatment of prostate cancer either in the definitive setting, in conjunction with high dose rate brachytherapy (HDRB) and post RP as either an adjuvant or salvage treatment. Compared to IMRT, VMAT is associated with lower rates of acute gastrointestinal (GI) and genitourinary (GU) toxicity in the treatment of prostate cancer [13].

This study documents the first Australian clinical experience of VMAT in the treatment of PLNs in higher risk prostate cancer. This occurred at the Mater Sydney Hospital, the Australian centre that has treated the largest cohort of such patients to date. The primary focus of the study was to validate our clinical impression of VMAT in terms of having an improved toxicity profile compared with published data on IMRT and 3D-CRT, particularly when treating large PLN volumes in the salvage setting following RP.

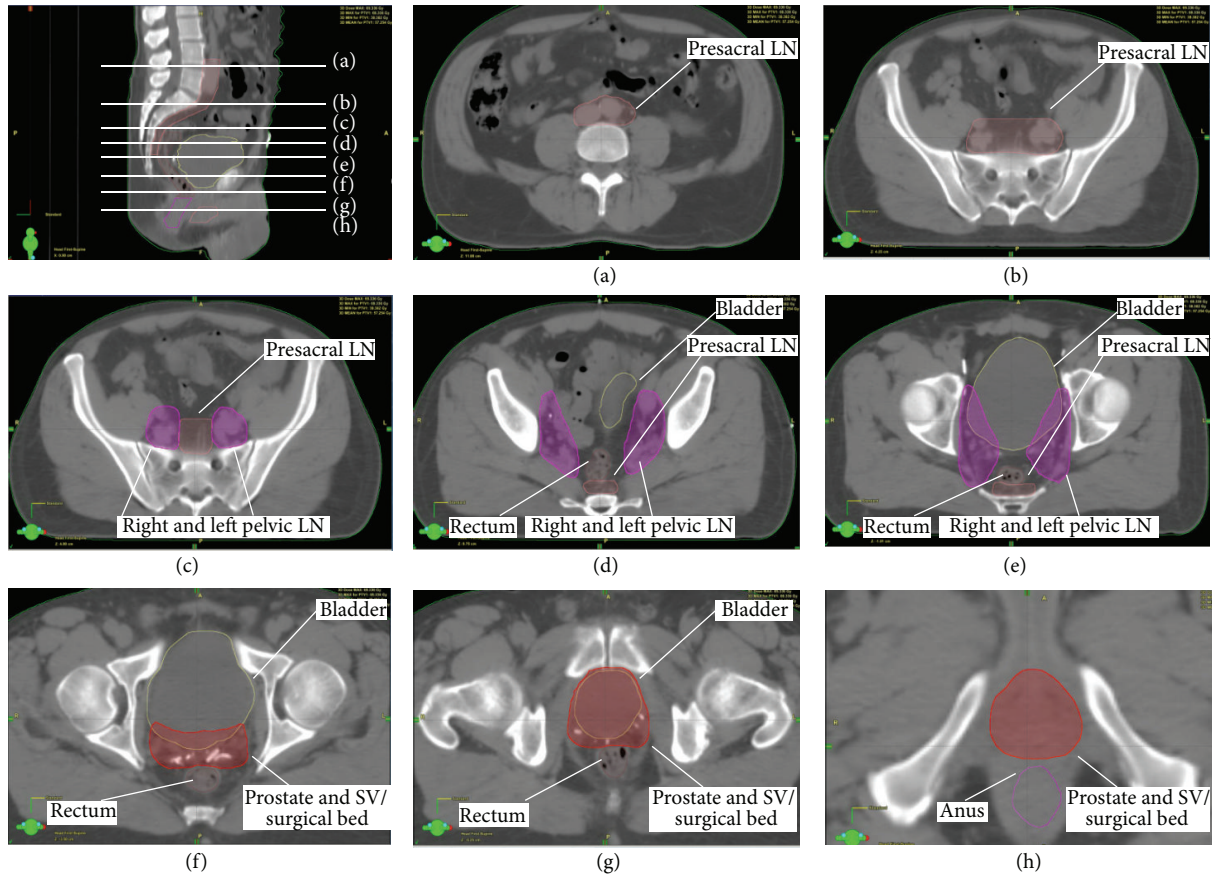
2. Materials and Methods

2.1. Patient Selection and Follow-Up. Patients with a diagnosis of prostate carcinoma who received VMAT radiotherapy from the start of the VMAT program in May 2010 to December 2012 were reviewed. Patient, tumour, and treatment characteristics were recorded and analysed. Staging details regarding the primary tumour, nodal involvement and presence of metastasis were derived from available documentation. The performance and extent of lymph node dissection was ascertained from the operation report or correspondence from the urologist. Due to the paucity of histopathological detail for patients who did not undergo RP, two separate cohorts were analyzed: those undergoing definitive RT and those who underwent adjuvant or salvage RT.

During treatment patients were assessed on a weekly basis. Acute and late genitourinary and gastrointestinal toxicities were documented according to the RTOG Version 2 Guidelines [14, 15]. Follow-up post treatment was performed at routine intervals, primarily by the treating radiation oncologist and if applicable, in conjunction with the referring urologist. The maximum toxicity suffered was recorded. Successive PSA values were measured on average 3 months apart. Given the short-term length of follow-up, oncological control was not a primary outcome of the study. An evaluation of early biochemical trends was performed by comparing the PSA levels before and after treatment as well as the need for ADT at one year following VMAT. Further analysis was performed to assess whether our clinical impression of patients who halved their PSA at 6 weeks following salvage radiotherapy continued to have a lowering of their PSA as observation continued.

2.2. Simulation. As per standard department policy, patients were requested to have an empty rectum and comfortably full bladder at simulation and treatment. CT simulation scans were performed in the supine position, scan window was from the top of L1 to mid femur, scanned at 2.5 mm intervals. Knee and feet supports and immobilization devices were utilized.

2.3. Contouring Technique. Contouring was manually performed by the treating Radiation Oncologist (GF). Clinical target volumes (CTVs) were contoured on the CT simulation scan with reference to RTOG and FROGG consensus guidelines [7, 8]. The prostate and seminal vesicles or the surgical bed of the prostate and seminal vesicles were contoured, with the aid of fiducial markers or surgical clips (Figures 1(f)–1(h)). The right and left PLN volumes were contoured, starting immediately above the prostate and seminal vesicle volumes (Figures 1(c)–1(e)). These volumes included the obturator, external, and internal iliac nodes with the anterior border beginning inferiorly at the anterior level of the acetabulum and following the external iliac artery posteriorly. The posterior border extended to encompass the internal iliac artery up to the bifurcation of the common iliac artery. The medial border of the volume was 0.5–1 cm short of the midline rectal structures. The right and left PLNs were combined into a single volume and treated as a single volume when no macroscopic nodal disease was present. The sacral lymph node volume started at the midline at the level of S3 (Figures 1(b)–1(e)). The contour was extended to embrace the bifurcation of the aorta, with the upper limit often at the level of the L4-5 disc space (Figure 1(a)). At the superior level of the previous right and left pelvic lymph node volumes, the sacral lymph node volume was expanded to include both the common iliac arteries. In the definitive, adjuvant, and salvage settings all of these volumes were expanded to a planning target volume (PTV) by 0.5 cm, excluding a volume termed “rectanus” (the combined contoured volumes of the anus and rectum). The anus was contoured from the first appearance inferiorly of a complete circle of sphincter tissue. The contour was taken in a superior direction until the most anterior circle that was devoid of rectal gas was reached (approximately 3–4 cm long). The rectum was then volumed superiorly from this level in a posterior direction until the structure started to turn anteriorly, which was taken as the start of the sigmoid colon. This was in concordance with the FROGG consensus guidelines [8]. The sigmoid colon and small bowel were also contoured but not excluded from the treatment volumes as these are structures on a mesentery and can therefore move between fractions. The dose volume constraints for each organ at risk are detailed in Table 1. The pelvic lymph node volumes were treated to higher doses if imaging or histopathology post RP showed disease in the pelvic lymph nodes. All patients were treated daily at five fractions per week. Image Guided radiotherapy (IGRT) with filming based on bony anatomy was done daily. A weekly kilovoltage CT scan was done on the department CT to confirm adequate bladder filling.



Red: prostate and seminal vesicles or surgical bed.
 Peach: sacral lymph node
 Orange: rectum
 Magenta (filled in): right and left pelvic lymph node
 Yellow: bladder
 Magenta (outline): anus

FIGURE 1: CT simulation scan demonstrating contoured volumes.

TABLE 1: Dose-volume constraints for organs at risk.

Organ	Dose (Gy)	Volume (%)
Bladder	40	<60
Anus	40	<35
Rectum	40	<35
Rectum	50	<30
Sigmoid colon	40	<35
Bowel	45	<30
Penile bulb	40	<50
Femoral head	35	<100

2.4. Treatment Planning and VMAT Delivery. Treatment plans were generated using Eclipse version 8.6 (copyright Varian, Palo Alto). Treatment delivery was done using a 21ix Varian Linear Accelerator. VMAT was delivered in two to three arcs with maximum range of 360-degree with simultaneous variation of the gantry speed, dose rate, and leaf position. An energy of 10 MV and a max dose rate of 600 monitor units per minute were used. Treatment prescriptions are summarized in Table 2. Treatment was delivered using

a simultaneous integrated boost (SIB) technique (Figure 2). Orthogonal kilovoltage images taken before the treatment confirmed patient position.

2.5. Statistical Analysis. The collected data was analysed to see if our clinical impression of patients who halved their PSA at 6 weeks following salvage radiotherapy continued to have a lowering of their PSA as observation continued. Statistical analysis was performed using IBM SPSS Statistic v21 (Chicago, IL) and SAS v9.3 (Cary, NC).

3. Results

3.1. Patient and Tumour Characteristics. 113 patients treated between May 2010 and December 2012 were identified. The median follow-up of the cohort was 14 months. Tables 3 and 4 summarize patient and tumour characteristics. Additional tumour characteristics for the cohort of patients who underwent RP are separated out in Table 4 due to the additional histopathological features available for this subset.

3.2. Toxicity. The acute GU and GI toxicity profiles for the entire and salvage cohorts are depicted in Table 5. Of note,

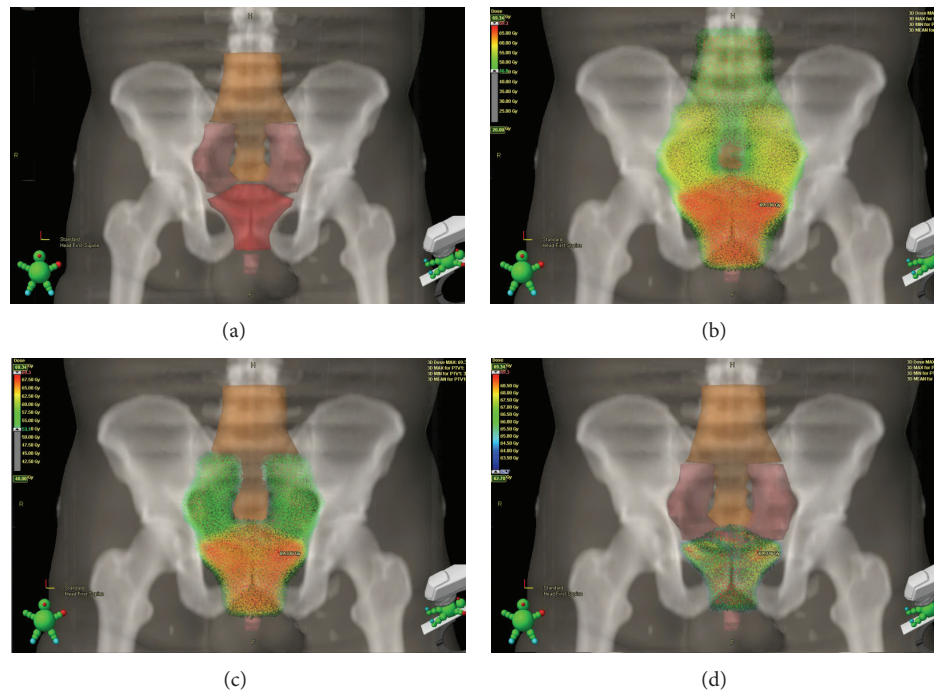


FIGURE 2: Dose distribution in adjuvant and salvage VMAT treatment. (a) Clinical target volumes: CTV 1 (orange) including presacral, common iliac, and para-aortic lymph nodes, left and right pelvic lymph nodes and prostate and seminal vesicles or prostatic fossa. CTV 2 (pink) including left and right pelvic lymph nodes and prostate and seminal vesicles or prostatic fossa. CTV 3 (red) including prostate and seminal vesicles or prostatic fossa. (b) Dose cloud superimposed on CTV 1: demonstrating dose of 49.5 Gy delivered to 95% of CTV 1 at 1.5 Gy per fraction for 33 fractions. (c) Simultaneous boost to 56.1 Gy: dose cloud superimposed on CTV 2 demonstrating dose of 56.1 Gy delivered to 95% of CTV 2 at 1.7 Gy per fraction for 33 fractions. (d) Simultaneous boost to 66 Gy: dose cloud superimposed on CTV 3 demonstrating dose of 66 Gy delivered to 95% of CTV 3 at 2 Gy per fraction for 33 fractions.

TABLE 2: Dose, fractionation schedules, and treatment groups.

Treatment intent	Prescription dose	Number of fractions	Number of patients (%)		
			No ADT	ADT	Total
Definitive VMAT					
Intermediate risk	74 Gy	37	5	4	9
High risk	78 Gy	39	1	15	16
Total	—	—	6 (5%)	19 (17%)	25 (22%)
VMAT following HDR brachytherapy	50.4 Gy	28	9 (8%)	16 (14%)	25 (22%)
Salvage VMAT	66 Gy	33	38 (34%)	11 (10%)	49 (44%)
Adjuvant VMAT	66 Gy	33	9 (8%)	5 (4%)	14 (12%)
Total	—	—	62 (55%)	51 (45%)	113 (100%)

no patients experienced an acute grade 3 or 4 complication. All acute reactions were symptomatically managed in the outpatient setting. No patients required hospital admission for management of acute side effects. In terms of late toxicity, only 1 patient experienced a late grade 3 GU complication. No late grade 4 GU or GI events have yet occurred at this early median follow-up.

3.3. Treatment Outcomes. A subset analysis was performed on the PSA dynamics of the 38 patients who underwent salvage VMAT for biochemical failure following radical prostatectomy, excluding those patients who used ADT at any stage of their treatment. The mean nadir PSA level reached

following VMAT was 0.08 ug/L at the end time point of this study. The PSA trend of biochemical failure following RP and the favorable trend following salvage treatment with VMAT is depicted in Figure 3.

In the same subset analysis of these 38 patients, analysis of the ratio of the PSA level taken immediately prior to salvage VMAT (defined as PSA_0) and the PSA value at 6 weeks following salvage treatment (defined as PSA_6) was undertaken. The mean PSA_0 was 0.39 ug/L (range 0.04–7.9) and PSA_6 was 0.15 ug/L (range 0.01–2.4). Twenty-one patients (55%) demonstrated a $PSA_6 : PSA_0 \leq 50\%$ and 17 patients (45%) demonstrated a $PSA_6 : PSA_0 > 50\%$. The relationship between the $PSA_6 : PSA_0$ ratio and BF following VMAT is

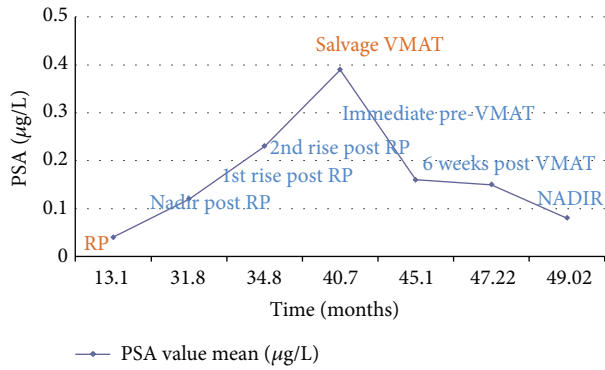


FIGURE 3: Average PSA dynamics following salvage VMAT treatment.

TABLE 3: Patient and tumour characteristics: entire cohort (n = 113).

Age (yrs)	Mean (range)	Distant metastases	N (%)
	67 (49–81)	No	107 (95%)
		Yes	4 (4%)
		Unknown	2 (2%)
T stage	N (%)	Gleason score	N (%)
T1-2a	38 (34%)	7	50 (44%)
T2b	8 (7%)	8	18 (16%)
T2c-4	60 (53%)	9	42 (37%)
Unknown	7 (6%)	Unknown	3 (3%)
Nodal status	N (%)	D'Amico Risk Group	N (%)
Negative	74 (65%)	Intermediate	46 (41%)
Positive	15 (13%)	High	63 (56%)
Unknown	24 (21%)	Unknown	4 (4%)

demonstrated in Table 6. The sensitivity and specificity of $PSA_6 : PSA_0 > 50\%$ for determining biochemical failure was 80% and 60.6% respectively. The sensitivity and specificity of $PSA_6 : PSA_0 > 75\%$ for determining biochemical failure was 80% and 84.8%, respectively.

Five patients (13.2% of the salvage, no ADT cohort) demonstrated biochemical failure following their salvage VMAT treatment. One out of 21 patients with $PSA_6 : PSA_0 \leq 50\%$ failed following their salvage VMAT treatment. The salvage treatment volumes for this particular patient only included the prostatic fossa as the patient had an extended lymph node dissection at the time of radical prostatectomy. This patient was retreated with a second course of salvage VMAT with lymph node volumes starting above his previous treatment level and extending superiorly to L4 and following this he remains biochemically disease-free. Of the 17 patients with a $PSA_6 : PSA_0 > 50\%$, 4 patients demonstrated biochemical failure following their salvage treatment. Two of these 4 patients were treated with a second course of salvage VMAT to their upper pelvic lymph nodes, with treatment volumes starting above their initial salvage volumes. After the second course of salvage treatment, PSA levels demonstrated trends towards biochemical control (being 0.02 and 0.04 ug/L, resp.). The other 2 patients were investigated further with

TABLE 4: Tumour characteristics: RP cohort (n = 63).

T stage	N (%)	Gleason score at margin	N (%)
T1-2a	20 (32%)	3	7 (11%)
T2b	1 (1%)	4	17 (27%)
T2c-4	37 (59%)	5	2 (3%)
Unknown	5 (8%)	Unknown	37 (59%)
Nodal status	N (%)	Seminal vesicle involvement	N (%)
Negative	44 (70%)	No	41 (65%)
Positive	9 (14%)	Unilateral	11 (17%)
Unknown	10 (16%)	Bilateral	5 (8%)
		Unknown	6 (10%)
Gleason score	N (%)	Vascular space involvement	N (%)
7	29 (46%)	No	40 (63%)
8	11 (17%)	Yes	15 (24%)
9	20 (32%)	Unknown	8 (13%)
Unknown	3 (5%)		
D'Amico Risk Group	N (%)	Perineural involvement	N (%)
Intermediate	31 (49%)	No	36 (57%)
High	29 (46%)	Yes	17 (27%)
Unknown	3 (5%)	Unknown	10 (16%)
Extracapsular extension	N (%)	Lymph node dissection (LND)	N (%)
Absent	19 (30%)	No	25 (40%)
Present	41 (65%)	Yes	37 (59%)
Unknown	3 (5%)	N/A or unknown	1 (1%)
Positive margin	N (%)	Extended LND	N (%)
Absent	34 (54%)	No	20 (32%)
Present	27 (43%)	Yes	22 (35%)
Unknown	2 (3%)	Unknown	21 (33%)

F-18 bone scans and found to have new bony metastasis in the ribs (n = 1) and spine (n = 1). One patient was subsequently commenced on ADT. This was the only patient out of the salvage cohort (3%) who went on to require ADT 12 months after their salvage treatment and PSA dynamics were excluded from analysis following commencement of ADT. The second patient who failed post salvage VMAT declined any further treatment at the time of his last review. Of note, ADT use 12 months following VMAT treatment for the entire cohort of patients was 12 out of 113 (11%).

4. Discussion

This study reviews the first Australian experience of VMAT in the treatment of pelvic lymph nodes of prostate cancer,

TABLE 5: Acute toxicity: entire and salvage cohort.

	Grade	Entire (<i>n</i> = 113) number (%)	Salvage (<i>n</i> = 38) number (%)
Acute GU	0	21 (19%)	14 (37%)
	1	67 (59%)	20 (53%)
	2	25 (22%)	4 (10%)
	3 or 4	0 (0%)	0 (0%)
Acute GI	0	20 (18%)	4 (10%)
	1	62 (55%)	22 (58%)
	2	31 (27%)	12 (32%)
	3 or 4	0 (0%)	0 (0%)

TABLE 6: Biochemical failure (BF) post salvage VMAT (*n* = 38) and relationship to $PSA_6 : PSA_0$.

Number of patients with BF post-VMAT	5
Number of patients with BF post-VMAT and $PSA_6 : PSA_0 > 0.5$	4
% of patients with BF with $PSA_6 : PSA_0 > 0.5$	80% (4 of 5 patients)
% of patients with $PSA_6 : PSA_0 > 0.5$ with BF	23.5% (4 of 17 patients)
% of patients with $PSA_6 : PSA_0 \leq 0.5$ without BF	95.2% (20 of 21 patients)

specifically to the level of the aortic bifurcation. Our study audited 113 patients diagnosed with prostate cancer who were treated with VMAT at the Mater Hospital in Sydney. It demonstrates the utility of VMAT across a range of clinical indications. Moreover our results indicate a favorable acute toxicity profile whilst treating large pelvic nodal volumes with optimal dose coverage up to the level of the aortic bifurcation. Finally, our study intimates promising oncological outcomes as indicated by the PSA trend and minimal use of ADT post VMAT.

A particular focus of the study was to analyze the utilization of VMAT in treating PLN volumes in the salvage setting where a major concern is treatment morbidity given the large treatment volumes. The acute GU and GI toxicity profiles experienced by our salvage cohort can be compared to those reported in published data following treatment of pelvic lymph node volumes using different radiotherapy modalities. In a study by Alongi et al., the acute toxicity profiles of 172 patients who underwent adjuvant or salvage whole pelvis radiotherapy (WPRT) with either 3DCRT or IMRT were analyzed [16]. The median dose and dose range delivered to the pelvic lymph nodes in our study using VMAT and in Alongi's report on 3DCRT and IMRT were 52.8 Gy (46.1–66), 50.4 Gy (45–50.4), and 50.4 Gy (50.4–54.0), respectively [16]. With the use of 3DCRT, the reported lower and upper acute GI toxicities grade ≥ 2 were 8.6% and 22%, respectively, and acute GU toxicities grade ≥ 2 were 12.3%. In another study by Ashman et al., acute GI and GU toxicities grade ≥ 2 were

reportedly as high as 57% and 34.7% [17]. Utilizing IMRT in WPRT delivers, as expected, an improved acute toxicity profile compared to 3D-CRT. Acute GI toxicities grade ≥ 2 have been reported as ranging from 6.6% to 40% and acute GU toxicities grade ≥ 2 ranging from 6.6% to 36.7% [9, 16, 18, 19]. Furthermore, studies have indicated that post-RP RT using IMRT is not associated with a decline in patient-reported urinary bowel or sexual quality of life indices at 2 years following completion of RT [20].

We have demonstrated in our study that with the use of VMAT, the acute toxicity profile can be improved upon even further. Acute GI and GU toxicities grade ≥ 2 for our salvage cohort were 34% and 13%, respectively. Similar promising results with VMAT have been reported in a recent study by Hall et al. in which acute GI and GU toxicities grade ≥ 2 were reported as 13.7% and 25%, respectively [13]. This observed benefit of VMAT may be due to its ability to deliver highly conformal dose distributions with improved target volume coverage and sparing of organs at risk [21]. This has been evident in the literature, which has demonstrated the superiority of both IMRT and VMAT in terms of dosimetry and sparing organs at risk compared to 3D-CRT [21–23]. VMAT further confers an additional advantage over IMRT and 3D-CRT in terms of its efficiency, safety, reduced monitor unit requirement, and cost-effectiveness [12, 22, 23]. VMAT delivered on treating a greater volume with an even better toxicity profile, further enhancing the therapeutic ratio in this small retrospective single institution study. Further follow-up of this cohort is required to ascertain whether a similar benefit is achieved in terms of late toxicities. Additionally, prospective randomized trials would be needed comparing the different radiotherapy modalities to conclusively demonstrate the toxicity profile advantage with VMAT.

Our study explored the validity of using the PSA value at 6 weeks post-VMAT treatment as a predictive tool for biochemical failure. Of the 21 patients who had a $PSA_6 : PSA_0 \leq 0.5$, only 1 patient demonstrated BF with the remainder 95% of patients remaining free from biochemical failure. The sensitivity and specificity of $PSA_6 : PSA_0 > 0.5$ for determining biochemical failure was calculated as 80% and 60.6%, respectively. Our findings demonstrate that this parameter may be useful in predicting biochemical failure; however, the validity of this would need to be assessed in a more robust study design.

This audit demonstrates an easy and simplified contouring technique for whole pelvis radiotherapy including large nodal volumes up to the level of the aortic bifurcation. The technique used by the treating radiation oncologist in our study draws upon both the FROGG and RTOG consensus guidelines [7, 8]. Delineation of the surgical bed CTV was done as per the FROGG and RTOG guidelines.

There are several limitations of our study to acknowledge. Firstly, the retrospective nature of this audit made it prone to missing data. Investigator bias may exist in that the patients were treated by a single radiation oncologist at a single institution. Our median follow-up time is at this stage is insufficient to fully assess late toxicities and long term biochemical control. Additionally, our study lacks validated quality of life assessment tools. Finally, the superiority of

VMAT over other treatment modalities would need to be assessed in a prospective randomized controlled trial.

5. Conclusions

VMAT can be utilized efficaciously in a variety of indications to manage carcinoma of the prostate especially in high risk disease where pelvic lymph node volumes can be included up to the aortic bifurcation. Our study demonstrates that this can be achieved with a favorable toxicity profile, both in the definitive and salvage settings. Short-term follow-up has demonstrated a trend towards favorable rates of biochemical control, which further supports the use of VMAT. With growing evidence to treat pelvic lymph nodes, both in the definitive and salvage settings, the utilization of VMAT will enable radiotherapy to be efficiently delivered to the required target volumes. Further follow-up is needed to assess long-term biochemical control and toxicity.

List of Abbreviations Used

3D-CRT:	3D conformal radiotherapy
ADT:	Androgen deprivation therapy
BF:	Biochemical failure
CT:	Computed tomography
CTV:	Clinical target volume
EBRT:	External beam radiotherapy
FROGG:	Faculty of Radiation Oncology Genito-Urinary Group
GETUG:	Genitourinary Tumor Group
GI:	Gastrointestinal
GU:	Genitourinary
HDRB:	High dose rate brachytherapy
IMRT:	Intensity modulated radiotherapy
PET:	Positron emission tomography
PLN:	Pelvic lymph nodes
PSA:	Prostate specific antigen
PTV:	Planning target volume
RP:	Radical prostatectomy
RT:	Radiotherapy
RTOG:	Radiation Therapy Oncology Group
VMAT:	Volumetric Modulated Arc Therapy
WPRT:	Whole pelvic radiotherapy.

Conflict of Interests

The authors declare that there is no conflict of interests regarding the publication of this paper.

Authors' Contribution

Gina Hesselberg and Gerald Fogarty are responsible for the initiation and coordination of the entire study. Data collection was conducted by Gina Hesselberg and Nicole Dougheney. Data was analysed by Lauren Haydu, Gina Hesselberg, and Gerald Fogarty. The paper was drafted, revised, and edited by Gina Hesselberg, Gerald Fogarty, and Phillip Stricker. All authors read and approved the final paper.

References

- [1] W. Ho, L. Mills, T. Negrello, H. Min, and E. Connell, *Cancer in Australia: An Overview 2012*, vol. 74 of *Australian Institute of Health and Welfare Cancer Series*, Australian Institute of Health and Welfare, 2012.
- [2] M. Roach III, M. DeSilvio, R. Valicenti et al., "Whole-pelvis, 'mini-pelvis,' or prostate-only external beam radiotherapy after neoadjuvant and concurrent hormonal therapy in patients treated in the Radiation Therapy Oncology Group 9413 trial," *International Journal of Radiation Oncology Biology Physics*, vol. 66, no. 3, pp. 647–653, 2006.
- [3] P. Pommier, S. Chabaud, J. L. Lagrange et al., "Is there a role for pelvic irradiation in localized prostate adenocarcinoma? Preliminary results of GETUG-01," *Journal of Clinical Oncology*, vol. 25, no. 34, pp. 5366–5373, 2007.
- [4] R. Schiavina, A. Bertaccini, A. Franceschelli et al., "The impact of the extent of lymph-node dissection on biochemical relapse after radical prostatectomy in node-negative patients," *Anti-cancer Research*, vol. 30, no. 6, pp. 2297–2302, 2010.
- [5] S. Daneshmand, M. L. Quek, J. P. Stein et al., "Prognosis of patients with lymph node positive prostate cancer following radical prostatectomy: long-term results," *The Journal of Urology*, vol. 172, no. 6, pp. 2252–2255, 2004.
- [6] L. K. Morikawa and M. Roach III, "Pelvic nodal radiotherapy in patients with unfavorable intermediate and high-risk prostate cancer: evidence, rationale, and future directions," *International Journal of Radiation Oncology*, vol. 80, pp. 6–16, 2011.
- [7] J. M. Michalski, C. Lawton, I. El Naqa et al., "Development of RTOG consensus guidelines for the definition of the clinical target volume for postoperative conformal radiation therapy for prostate cancer," *International Journal of Radiation Oncology Biology Physics*, vol. 76, no. 2, pp. 361–368, 2010.
- [8] M. A. Sidhom, A. B. Kneebone, M. Lehman et al., "Post-prostatectomy radiation therapy: consensus guidelines of the Australian and New Zealand Radiation Oncology Genito-Urinary Group," *Radiotherapy and Oncology*, vol. 88, no. 1, pp. 10–19, 2008.
- [9] L. P. Muren, E. Wasbø, S. I. Helle et al., "Intensity-modulated radiotherapy of pelvic lymph nodes in locally advanced prostate cancer: planning procedures and early experiences," *International Journal of Radiation Oncology, Biology, Physics*, vol. 71, no. 4, pp. 1034–1041, 2008.
- [10] A. Goenka, J. M. Magsanoc, X. Pei et al., "Improved toxicity profile following high-dose postprostatectomy salvage radiation therapy with intensity-modulated radiation therapy," *European Urology*, vol. 60, no. 6, pp. 1142–1148, 2011.
- [11] O. Riou, P. Fenoglio, B. Laliberté et al., "Three years of salvage IMRT for prostate cancer: results of the Montpellier Cancer Center," *ISRN Urology*, vol. 2012, Article ID 391705, 7 pages, 2012.
- [12] G. B. Fogarty, D. Ng, G. Liu, L. E. Haydu, and N. Bhandari, "Volumetric modulated arc therapy is superior to conventional intensity modulated radiotherapy—a comparison among prostate cancer patients treated in an Australian centre," *Radiation Oncology*, vol. 6, no. 1, article 108, 2011.
- [13] W. A. Hall, L. Colbert, D. Nickleach et al., "Reduced acute toxicity associated with the use of volumetric modulated arc therapy for the treatment of adenocarcinoma of the prostate," *Practical Radiation Oncology*, vol. 3, no. 4, pp. e157–e164, 2013.
- [14] RTOG, *Acute Radiation Morbidity Scoring Criteria*, Radiation Therapy Oncology Group, Philadelphia, Pa, USA, 2015,

<http://www.rtog.org/ResearchAssociates/AdverseEventReporting/AcuteRadiationMorbidityScoringCriteria.aspx>.

- [15] RTOG, *RTOG/EORTC Late Radiation Morbidity Scoring Schema*, Radiation Therapy Oncology Group, Philadelphia, Pa, USA, 2015, <http://www.rtog.org/ResearchAssociates/AdverseEventReporting/RTOGEORTCLateRadiationMorbidityScoringSchema.aspx>.
- [16] F. Alongi, C. Fiorino, C. Cozzarini et al., "IMRT significantly reduces acute toxicity of whole-pelvis irradiation in patients treated with post-operative adjuvant or salvage radiotherapy after radical prostatectomy," *Radiotherapy and Oncology*, vol. 93, no. 2, pp. 207–212, 2009.
- [17] J. B. Ashman, M. J. Zelefsky, M. S. Hunt, S. A. Leibel, and Z. Fuks, "Whole pelvic radiotherapy for prostate cancer using 3D conformal and intensity-modulated radiotherapy," *International Journal of Radiation Oncology Biology Physics*, vol. 63, no. 3, pp. 765–771, 2005.
- [18] T. Guerrero Urbano, V. Khoo, J. Staffurth et al., "Intensity-modulated radiotherapy allows escalation of the radiation dose to the pelvic lymph nodes in patients with locally advanced prostate cancer: preliminary results of a phase i dose escalation study," *Clinical Oncology*, vol. 22, no. 3, pp. 236–244, 2010.
- [19] R. McCammon, K. E. Rusthoven, B. Kavanagh, S. Newell, F. Newman, and D. Raben, "Toxicity assessment of pelvic intensity-modulated radiotherapy with hypofractionated simultaneous integrated boost to prostate for intermediate- and high-risk prostate cancer," *International Journal of Radiation Oncology Biology Physics*, vol. 75, no. 2, pp. 413–420, 2009.
- [20] K. S. Corbin, R. Kunnavakkam, S. E. Eggener, and S. L. Liauw, "Intensity modulated radiation therapy after radical prostatectomy: early results show no decline in urinary continence, gastrointestinal, or sexual quality of life," *Practical Radiation Oncology*, vol. 3, no. 2, pp. 138–144, 2013.
- [21] M. Teoh, C. H. Clark, K. Wood, S. Whitaker, and A. Nisbet, "Volumetric modulated arc therapy: a review of current literature and clinical use in practice," *British Journal of Radiology*, vol. 84, no. 1007, pp. 967–996, 2011.
- [22] D. Wolff, F. Stieler, G. Welzel et al., "Volumetric modulated arc therapy (VMAT) vs. serial tomotherapy, step-and-shoot IMRT and 3D-conformal RT for treatment of prostate cancer," *Radiotherapy and Oncology*, vol. 93, no. 2, pp. 226–233, 2009.
- [23] D. Palma, E. Vollans, K. James et al., "Volumetric modulated arc therapy for delivery of prostate radiotherapy: comparison with intensity-modulated radiotherapy and three-dimensional conformal radiotherapy," *International Journal of Radiation Oncology Biology Physics*, vol. 72, no. 4, pp. 996–1001, 2008.

Research Article

An IMRT/VMAT Technique for Nonsmall Cell Lung Cancer

Nan Zhao, Ruijie Yang, Junjie Wang, Xile Zhang, and Jinna Li

Department of Radiation Oncology, Peking University Third Hospital, Beijing 100191, China

Correspondence should be addressed to Ruijie Yang; ruijiyang@yahoo.com

Received 9 May 2015; Revised 13 July 2015; Accepted 21 July 2015

Academic Editor: Jun Deng

Copyright © 2015 Nan Zhao et al. This is an open access article distributed under the Creative Commons Attribution License, which permits unrestricted use, distribution, and reproduction in any medium, provided the original work is properly cited.

The study is to investigate a Hybrid IMRT/VMAT technique which combines intensity modulated radiation therapy (IMRT) and volumetric modulated arc therapy (VMAT) for the treatment of nonsmall cell lung cancer (NSCLC). Two partial arcs VMAT, 5-field IMRT, and hybrid plans were created for 15 patients with NSCLC. The hybrid plans were combination of 2 partial arcs VMAT and 5-field IMRT. The dose distribution of planning target volume (PTV) and organs at risk (OARs) for hybrid technique was compared with IMRT and VMAT. The monitor units (MUs) and treatment delivery time were also evaluated. Hybrid technique significantly improved the target conformity and homogeneity compared with IMRT and VMAT. The mean delivery time of IMRT, VMAT, and hybrid plans was 280 s, 114 s, and 327 s, respectively. The mean MUs needed for IMRT, VMAT, and hybrid plans were 933, 512, and 737, respectively. Hybrid technique reduced V_5 , V_{10} , V_{30} , and MLD of normal lung compared with VMAT and spared the OARs better with fewer MUs with the cost of a little higher V_5 , V_{10} , and mean lung dose (MLD) of normal lung compared with IMRT. Hybrid IMRT/VMAT can be a viable radiotherapy technique with better plan quality.

1. Introduction

Treatment of nonsmall cell lung cancer (NSCLC) remains one of the major challenges for radiotherapy. Three-dimensional conformal radiotherapy (3D-CRT) has proved to be a promising treatment method for NSCLC allowing higher doses to be delivered to the target by improved shaping of radiation portals and conformal avoidance of normal structures compared with the conventional radiotherapy [1]. Compared to 3D-CRT, intensity modulated radiation therapy (IMRT) further significantly improved the dose conformity and sparing of organs at risk [2]. However, the longer treatment time in IMRT could increase the discomfort of the patients during the treatment, and more MUs could increase the incidence of secondary radiation-induced cancer [3, 4]. Volumetric modulated arc therapy (VMAT) provided more conformal target coverage and better sparing of organs at risk (OARs), with shorter treatment delivery time and fewer MUs than IMRT in treating cancers of different sites [5–9]. However, a larger volume of lung receiving lower dose (V_5 and V_{10}) in VMAT has been reported [10]. Dose volume histogram parameters of V_5 [11–14] and V_{10} [12, 14, 15] have been showed to be the predictors of the radiation pneumonitis.

The aim of this study is to investigate a radiotherapy technique we call Hybrid IMRT/VMAT for nonsmall cell lung cancer treatments. The dosimetric quality and delivery efficiency of the Hybrid IMRT/VMAT technique were evaluated by comparing with IMRT and VMAT for 15 nonsmall cell lung cancer patients.

2. Methods and Materials

2.1. Patients' Characteristics. Fifteen NSCLC patients who underwent radiotherapy from January 2012 to April 2013 in our hospital were retrospectively selected for this study.

2.2. Delineation of Target Volumes and Critical Structures. The patients underwent four-dimensional computed tomography (4D-CT) (Brilliance Big Bore, Philips Medical Systems, Cleveland, USA) scanning in 5 mm slice thickness, 0.5 seconds of scan time per rotation during normal breathing in supine arm-up position. The gross tumor volume (GTV) was defined as the visualization of any gross tumor and lymph nodes involved (>1 cm on CT). An internal target volume (ITV) was obtained as a union of the GTVs from all respiratory motion phases. The CTV was defined as the potential

TABLE 1: Treatment planning objectives used for Hybrid IMRT/VMAT, IMRT, and VMAT plans.

PTV	$D_{98\%}$	>62.7 Gy
	$D_{2\%}$	<72.6 Gy
Normal lung	$*V_5$	<60%
	$*V_{10}$	<40%
	$*V_{20}$	<30%
	$*V_{30}$	<20%
	Mean dose	<16 Gy
Spinal cord	Max dose	<50 Gy
Esophagus	Max dose	<66 Gy
	Mean dose	<34 Gy
Heart	$*V_{40}$	<80%
	$*V_{50}$	<30%
	Mean dose	<30 Gy

PTV is planning target volume.

$*V_N$ is percentage volume of OARs receiving at least N Gy of radiation dose.

harboring microscopic disease. The PTV was created by expanding the CTV by 0.5 cm. The OARs delineated included the double lungs, normal lung, spinal cord, esophagus, and heart. We defined the double lungs minus GTV as normal lung. The spinal cord and the esophagus were contoured starting at least 2 cm above the superior extent of the PTV and continuing on every CT slice to at least 2 cm below the inferior extent of the PTV. No margins were added to the organs at risk.

2.3. Treatment Planning. Hybrid IMRT/VMAT, IMRT, and VMAT plans were designed for each patient. The prescribed dose to the PTV was 66 Gy in 33 fractions. The plans were normalized to cover 95% of the PTV with 100% of the prescribed dose. The optimization objectives and constraints shown in Table 1 were the same for the three techniques. Eclipse 10.0 (Varian, Palo Alto, CA) treatment planning system was used for all treatment planning, utilizing 6 MV photon beams generated from Varian Trilogy linac equipped with a 120 leaf Millennium Multileaf Collimator (MLC).

2.4. IMRT. The beam angles of IMRT were initially optimized by the beam angle optimization algorithm (Varian Eclipse 10.0); a set of initial optimization objectives were loaded into the treatment planning system. The number of the fields was confined to five. Some beam angles were adjusted according to the experience of the dosimetrists, if the results of the beam angle optimization did not satisfy the dosimetric criteria. The plans were iteratively optimized to obtain the optimal PTV coverage and OARs sparing. After inverse planning, the leaf sequences using sliding window technique were generated for IMRT plans.

2.5. VMAT. All VMAT plans were generated using 2 partial arcs. The collimator angle varied between 0° and 90° according to the shape of the target while minimizing the leakage, tongue, and groove effects. Other planning parameters were

MLC motion speed 0 to 2.5 cm/s, gantry rotation speed 0.5 to 4.8 degrees/s, and dose rate 0 to 600 MU/min.

2.6. Hybrid IMRT/VMAT. The Hybrid IMRT/VMAT technique integrates IMRT and VMAT. The IMRT part consists of a 5-field IMRT plan (Hybrid-IMRT), which contributes half of the total prescribed dose, while the VMAT parts consist of a 2 partial arcs VMAT plan (Hybrid-VMAT) which was optimized with the IMRT plan as a base plan, to deliver the other half of the prescribed dose.

2.7. Dosimetric Evaluation. The dosimetric quality of the Hybrid IMRT/VMAT plans was evaluated by comparison with IMRT and VMAT. To evaluate the dose distribution of the target, we calculated the minimal dose delivered to the 98% of the target volume ($D_{98\%}$), the maximum dose delivered to the 2% of the target volume ($D_{2\%}$), the median absorbed dose delivered to the 50% of the target volume ($D_{50\%}$), conformation number (CN), and homogeneity index (HI) according to the ICRU report 83 [16]. All parameters were computed on the basis of the DVH. The CN was defined using the equation [11]

$$CN = \frac{TV_{RI}}{TV} \times \frac{TV_{RI}}{V_{RI}}, \quad (1)$$

where CN is conformation number, TV_{RI} is target volume covered by the reference isodose, TV is target volume, and V_{RI} is volume of the reference isodose. The CN ranged from 0 to 1, where 1 was the ideal value. A larger CN indicated a smaller volume of the prescription dose delivered outside the PTV. The HI was defined using the equation [16]

$$HI = \frac{D_{2\%} - D_{98\%}}{D_{50\%}}. \quad (2)$$

An HI of 0 indicated that the dose distribution was almost homogenous. A larger HI indicated a greater dose exceeding the prescribed dose and/or a larger volume of the target receiving too small dose. The evaluation criteria of OARs were defined basically according to RTOG 1106 protocols. V_5 , V_{10} , V_{20} , V_{30} , and mean lung dose (MLD) values were recorded and compared for normal lung, as well as the maximum dose of the spinal cord, the mean and maximum dose of the esophagus, the $D_{2\%}$, V_{40} , V_{60} , and mean dose of the heart.

2.8. Treatment Delivery Time and MUs. The Hybrid IMRT/VMAT, IMRT, and VMAT plans for 15 patients were delivered to a solid water phantom (Multicube Phantom, IBA, Germany) on the Trilogy linear accelerator. The treatment delivery time and MUs were recorded and evaluated. The treatment delivery time was defined as the time from first beam on until last beam off.

2.9. Dosimetric Evaluation Stratified by Target Volume. In order to investigate the target volume effect on the selection of the optimal technique, we separated the 15 patients into two groups according to the volumes of the PTVs, 8 patients with

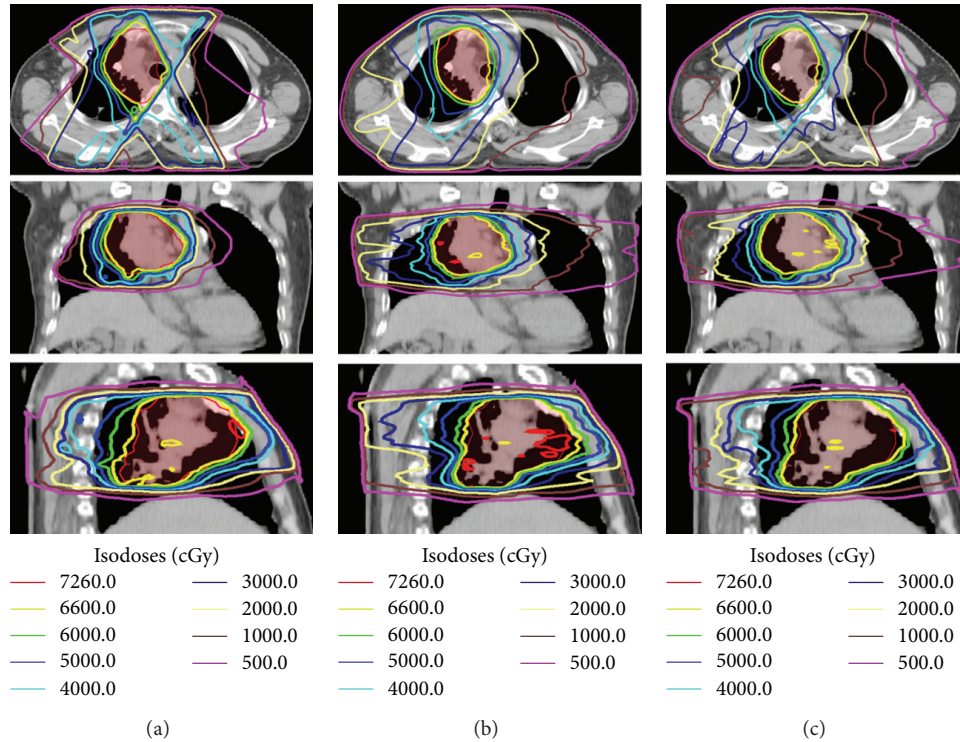


FIGURE 1: Representative axial, coronal, and sagittal computed tomography slices showing isodose distribution for (a) IMRT, (b) VMAT, and (c) Hybrid IMRT/VMAT. Planning target volume (PTV) shown in red.

the PTV volumes smaller and 7 patients larger than the mean volume of the PTVs (416.1 cm^3). The dose distribution of planning target volume (PTV) and organs at risk (OARs) for Hybrid IMRT/VMAT was compared with IMRT and VMAT for two groups separately.

2.10. *Statistical Analysis.* Paired two tailed *t*-test was used to compare the three techniques. Statistical analysis was performed using the SPSS (version 13.0, Chicago, IL) for Windows. Differences were reported to be statistically significant at $p < 0.05$.

3. Results

The mean volume of the PTV was 416.1 cm^3 (173.4 cm^3 to 887.0 cm^3). For all 15 cases, all the plans were clinically acceptable in terms of target coverage, with at least 98% PTV receiving 95% of the prescribed dose. The typical isodose distribution and DVH comparison were given in Figures 1 and 2 for a patient with stage IIIB nonsmall cell lung cancer. The PTV was 414.0 cm^3 . The lesions were located in the right hilus pulmonis and the upper lobe of the right lung. The beams obtained by the beam angle optimization for IMRT are 39° , 150° , 210° , 306° , and 342° . Two partial arcs of $0^\circ \sim 181^\circ$ and $181^\circ \sim 0^\circ$ were used for VMAT.

3.1. *Target Coverage.* The data for PTV coverage and OARs sparing of IMRT, VMAT, and Hybrid IMRT/VMAT plans

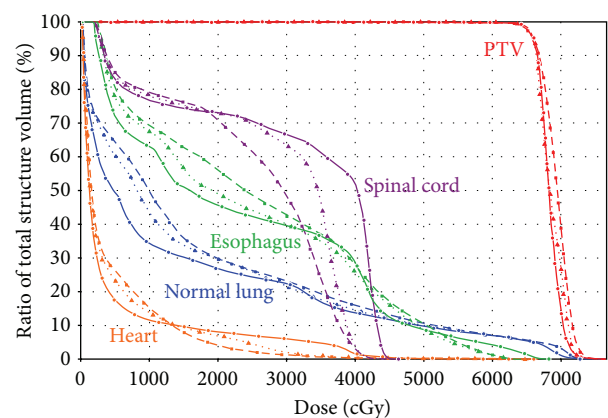


FIGURE 2: Representative dose volume histogram for IMRT, VMAT, and Hybrid IMRT/VMAT. The curves of IMRT, VMAT, and Hybrid IMRT/VMAT are indicated in solid lines, dashed lines, and dotted lines, respectively.

were summarized in Tables 2 and 3. Hybrid IMRT/VMAT significantly improved the target conformity compared with IMRT and VMAT. The mean CN was 0.79, 0.86, and 0.88 for IMRT, VMAT, and hybrid plans, respectively. Hybrid IMRT/VMAT also significantly improved the PTV dose homogeneity compared with IMRT (9.8 versus 11.3; $p < 0.05$) and VMAT (9.8 versus 12.6; $p < 0.05$). Compared with IMRT, VMAT also improved the dose conformity.

TABLE 2: The data for PTV coverage for IMRT, VMAT, and Hybrid IMRT/VMAT plans.

	IMRT Mean \pm SD	VMAT Mean \pm SD	Hybrid Mean \pm SD	IMRT versus VMAT <i>p</i> value	IMRT versus Hybrid <i>p</i> value	VMAT versus Hybrid <i>p</i> value
PTV						
$D_{98\%}$ (Gy)	64.6 \pm 0.5	64.6 \pm 0.5	65.0 \pm 0.3	>0.05	<0.05	<0.05
$D_{2\%}$ (Gy)	72.6 \pm 1.7	73.3 \pm 1.7	71.5 \pm 1.0	>0.05	<0.05	<0.05
CN	0.79 \pm 0.05	0.86 \pm 0.04	0.88 \pm 0.03	<0.05	<0.05	<0.05
HI (%)	11.3 \pm 0.7	12.6 \pm 0.6	9.8 \pm 0.3	<0.05	<0.05	<0.05

PTV is planning target volume, IMRT is intensity modulated radiation therapy, VMAT is volumetric modulated arc therapy, CN is conformation number, and HI is homogeneity index.

TABLE 3: The data for OARs sparing for IMRT, VMAT, and Hybrid IMRT/VMAT plans.

	IMRT Mean \pm SD	VMAT Mean \pm SD	Hybrid Mean \pm SD	IMRT versus VMAT <i>p</i> value	IMRT versus Hybrid <i>p</i> value	VMAT versus Hybrid <i>p</i> value
Normal lung						
$D_{2\%}$ (Gy)	67.5 \pm 2.7	67.9 \pm 3.7	67.7 \pm 3.2	>0.05	>0.05	>0.05
* V_{30} (%)	18.7 \pm 4.1	18.4 \pm 4.2	17.7 \pm 3.9	>0.05	<0.05	<0.05
* V_{20} (%)	25.4 \pm 4.9	25.2 \pm 6.1	25.5 \pm 5.6	>0.05	>0.05	>0.05
* V_{10} (%)	35.2 \pm 6.9	41.7 \pm 8.0	38.5 \pm 7.3	<0.05	<0.05	<0.05
* V_5 (%)	50.0 \pm 8.2	60.3 \pm 11.2	57.2 \pm 10.7	<0.05	<0.05	<0.05
Mean (Gy)	14.2 \pm 2.2	15.2 \pm 2.6	14.6 \pm 2.3	<0.05	<0.05	<0.05
Spinal cord						
D_{\max} (Gy)	41.5 \pm 10.0	35.7 \pm 10.5	35.9 \pm 9.0	<0.05	<0.05	>0.05
Esophagus						
D_{\max} (Gy)	67.0 \pm 5.7	66.2 \pm 6.9	63.7 \pm 7.9	>0.05	<0.05	<0.05
Mean (Gy)	22.9 \pm 9.9	23.0 \pm 9.6	22.4 \pm 9.7	>0.05	<0.05	<0.05
Heart						
$D_{2\%}$ (Gy)	34.0 \pm 25.7	31.3 \pm 24.0	31.6 \pm 23.8	>0.05	<0.05	>0.05
Mean (Gy)	8.5 \pm 8.8	7.4 \pm 7.1	7.8 \pm 7.8	<0.05	<0.05	>0.05
* V_{60} (%)	1.1 \pm 2.0	0.9 \pm 1.6	0.8 \pm 1.5	<0.05	<0.05	>0.05
* V_{40} (%)	4.5 \pm 5.6	2.8 \pm 4.0	3.2 \pm 4.4	<0.05	<0.05	>0.05

PTV is planning target volume, IMRT is intensity modulated radiation therapy, VMAT is volumetric modulated arc therapy, CN is conformation number, and HI is homogeneity index.

* V_N is percentage volume of OARs receiving at least N Gy of radiation dose.

3.2. Organs at Risk Sparing. The V_{30} of normal lung for hybrid plans was significantly lower than IMRT plans (17.7% versus 18.7%; $p < 0.05$) and VMAT plans (17.7% versus 18.4%; $p < 0.05$). There was no significant difference in V_{20} of normal lung among three techniques. The V_5 , V_{10} , and mean lung dose (MLD) of normal lung for hybrid plans were 12.6%, 8.6%, and 2.7% higher than those for IMRT plans, respectively ($p < 0.05$). However, the V_5 , V_{10} , V_{30} , and MLD of normal lung for hybrid plans were 5.1%, 7.7%, 3.8%, and 3.9% lower than those for VMAT plans, respectively ($p < 0.05$). The maximum doses of spinal cord and esophagus for hybrid plans were 5.6 Gy and 3.3 Gy lower than those for IMRT plans ($p < 0.05$). The mean doses of esophagus and heart for hybrid plans were 2.2% and 8.2% lower than IMRT plans ($p < 0.05$). The V_{40} and V_{60} of heart for hybrid plans were 27.3% and 28.9% lower than those for IMRT plans ($p < 0.05$).

3.3. Treatment Delivery Time and MUs. The mean delivery time of hybrid plans was longer than that of IMRT plans (327 s

versus 280 s; $p < 0.05$) and that of VMAT plans (327 s versus 114 s; $p < 0.05$). The number of mean MUs of hybrid plans (797 \pm 81) was between the values of IMRT (997 \pm 140) and VMAT plans (509 \pm 53).

3.4. Dosimetric Evaluation Stratified by Target Volume. For the patients with the PTV volume smaller than 416.1 cm³, the mean CN was 0.72, 0.86, and 0.89 for IMRT, VMAT, and hybrid plans, respectively. Hybrid plans also significantly improved the PTV dose homogeneity compared with IMRT (9.9 versus 17.1; $p < 0.05$) and VMAT (9.9 versus 14.9; $p < 0.05$). The mean V_5 and V_{10} of normal lung for hybrid plans were 31.3% and 19.0%, with an absolute difference of 4.1% and 1.1% lower than those for VMAT plans ($p < 0.05$), respectively. The MLD for hybrid plans was 6.8 Gy, 0.4 Gy lower than that for VMAT plans ($p < 0.05$). No difference of V_{20} of normal lung among the IMRT, VMAT, and hybrid plans was found. The mean V_{30} of normal lung for hybrid

plans was 20.3% lower than that for IMRT plans ($p < 0.05$). No significant difference was found in the mean V_{30} of normal lung between hybrid and VMAT plans. The maximum dose of spinal cord for hybrid plans was 27.6 Gy, which was 4.3 Gy lower than that for IMRT plans ($p < 0.05$). The mean dose of esophagus for hybrid plans was 9.4 Gy, which was 0.7 Gy lower than that for VMAT plans ($p < 0.05$). No differences in the mean D_{\max} of esophagus and $D_{2\%}$, mean dose, V_{60} , V_{40} of heart among the IMRT, VMAT, and hybrid plans were found.

For the patients with the PTV volume larger than 416.1 cm^3 , the mean CN was 0.64, 0.80, and 0.83 for IMRT, VMAT, and hybrid plans, respectively. Hybrid plans also significantly improved the PTV dose homogeneity compared with IMRT (10.0 versus 14.6; $p < 0.05$). The mean V_5 of normal lung for hybrid plans was 49.2%, with an absolute difference of 4.4% lower than that for VMAT plans ($p < 0.05$), while no difference was found for V_{10} between two techniques. The MLD for hybrid plans was 10.4 Gy, 0.6 Gy lower than that for VMAT plans ($p < 0.05$). No differences of V_{20} and V_{30} of normal lung among the IMRT, VMAT, and hybrid plans were found. The maximum dose of spinal cord for hybrid plans was 37.0 Gy, which was 5.8 Gy lower than that for IMRT plans ($p < 0.05$). No differences of D_{\max} , mean dose of esophagus and $D_{2\%}$, mean dose, V_{60} , V_{40} of heart among the IMRT, VMAT, and hybrid plans were found.

4. Discussion

In this study, we investigated a Hybrid IMRT/VMAT technique for primary nonsmall cell lung cancer. Compared with IMRT and VMAT, the improvements in conformity and homogeneity with Hybrid IMRT/VMAT were especially important when the target was in close proximity to the spinal cord limiting a satisfactory coverage of PTV. Compared with IMRT, Hybrid IMRT/VMAT significantly reduced the irradiated volume of the OARs and normal tissue receiving medium to high dose. Compared with VMAT, Hybrid IMRT/VMAT reduced the volume of normal lung receiving dose higher than 5 Gy, 10 Gy, 30 Gy, and MLD significantly.

Several studies suggested that V_5 [11–14], V_{10} [12, 14, 15], and MLD [14, 15, 17, 18] were correlated with radiation pneumonitis, although the determination of the contributors to radiation pneumonitis was challenging, since a variety of treatment/patient-related factors appeared to influence this risk.

There were several studies demonstrating that VMAT could reduce delivery time and MUs compared with IMRT [12–15]. Reduction of delivery time could decrease the possibility of the intrafraction patient motion that leads to target underdosage and/or worse OARs sparing. However, the treatment delivery time of hybrid plans was longer than that of VMAT and IMRT plans in our study, because a hybrid plan comprised of both a 5-field IMRT and a 2 partial arcs VMAT. Liu et al. [19] reported that IMRT plans with fewer beams (five or seven beams) could achieve dosimetric quality comparable to those using nine equal-spaced beams, with reduced MUs and field segments. Using nine equal-spaced beams could allow more conformal plans but increased V_5 and V_{10} of normal lung. So, we used 5-field IMRT plans to

reduce the low dose distribution for normal lung. Chan et al. [20] reported that, in their pilot study of using VMAT, dosimetric distribution of one full arc was less favorable compared to those with two half arcs. So, 2 partial arcs VMAT was a good choice to compare with IMRT and Hybrid IMRT/VMAT.

Hybrid IMRT/VMAT improved the target dose conformity and homogeneity compared with IMRT and VMAT, while the difference of dose homogeneity of hybrid and VMAT plans became insignificant for the patients with the PTV volume larger than 416.1 cm^3 . The possible reason was that IMRT and VMAT made compromises in different aspects. IMRT achieved a reasonable dose distribution by intensity modulation with limited angular beam sampling. Due to the sparse angular sampling in IMRT, the conformity of the resultant dose distribution was often limited. On the other hand, while VMAT had sufficient angular sampling, it did not provide the desired intensity modulation in some beam directions. The final dose distribution depended on the level of intensity modulation and angular sampling. Hybrid IMRT/VMAT improved the target conformity and homogeneity by increasing the freedom to find the optimal combination of angular sampling and intensity modulation. The reason for the insignificance of homogeneity difference with increasing target volume between VMAT and hybrid plans was perhaps due to the fact that the homogeneity saturated by increasing the angular sampling in VMAT beyond a certain level, with the side effect of spreading low dose, which was also demonstrated as the reduced V_{30} in VMAT and hybrid plans compared with IMRT for smaller targets, whereas no difference was found among three techniques for larger targets.

Several recent publications have introduced hybrid techniques which consisted of IMRT and arc with the purpose of combining the efficiency of arc and OARs sparing of IMRT. Martin et al. [17] reported that a novel IMRT & Arc technique consisted of 4-field IMRT in conjunction with a conformal arc. They demonstrated that for patients with esophageal cancers the IMRT & Arc technique could potentially improve the therapeutic ratio in reduction of cardiorelated and pulmonary toxicity compared with plans for either helical tomotherapy or single-arc RapidArc plans. The forward planning for the conformal arc, as well as the manual IMRT beam arrangement, was used in their study. Similarly, Robar and Thomas [18] reported a HybridArc technique combining optimized dynamic conformal arcs and IMRT. In contrast to VMAT component in Hybrid IMRT/VMAT, the arc component of IMRT & Arc and HybridArc did not involve intensity modulation, for example, via dose rate or gantry speed modulation, overlapping multiple arcs, or associated linac functionality. Compared with Hybrid IMRT/VMAT technique, the degrees of freedom of IMRT & Arc and HybridArc were limited by (1) only a single pass by each arc, (2) constant dose rate, and (3) constant gantry speed. So no improvements in the brainstem and optic chiasm sparing were found in HybridArc compared with IMRT for the complex cranial cases. Chan et al. [20] reported that the Hybrid-RapidArc technique utilizing two arcs with additional static conformal fields could produce lower V_5 ,

V_{10} , and MLD than double arcs RapidArc technique for lung cancers. However, Hybrid-RapidArc failed to meet the plan acceptance criteria due to the limited ability of intensity modulation with the conformal radiotherapy component, especially for the challenging cases (highly irregular PTV), with involving mediastinal lymphadenopathy. Furthermore, the ability to reduce the volume of normal lung receiving low doses was limited, because the intensity of the static beams could not be modulated to achieve good target conformity.

We developed a Hybrid IMRT/VMAT technique using IMRT as the base plan and then optimized the VMAT plan achieving trade-off between better dosimetric quality of IMRT and delivery efficiency (fewer MUs) of VMAT. This technique can be used on any treatment planning system capable of producing both VMAT and IMRT plans. Additional research work on the Hybrid IMRT/VMAT strategy is warranted in several areas. Most notable is to develop an optimization algorithm which can optimize both VMAT and IMRT simultaneously to determine the optimal proportion of the prescribed dose for the IMRT and VMAT components, the delivery sequence integrating the IMRT and VMAT components. Furthermore, the types of cancer sites and geometries that will benefit most from this Hybrid IMRT/VMAT technique should be further investigated.

We investigated the influence of prescription dose ratio between IMRT and VMAT in Hybrid IMRT/VMAT on the dose distribution and delivery efficiency, by creating the plans with the weighting of IMRT to VMAT of 1:1, 1:2, and 2:1. The results demonstrated that better conformity, homogeneity, sparing of normal lung from higher dose irradiation, and delivery efficiency were obtained with the increasing weight of the VMAT, with the cost of increasing the volume of low dose to normal lung (V_5 , V_{10}) and MLD. In addition, the ideal number of IMRT beams and VMAT arcs and the start and stop angle of arcs in hybrid plans would likely vary for different cases. For the representative case in this study, the beam angles of the IMRT plan were optimized using the beam angle optimization algorithm. Two right-anterior oblique fields and a right-posterior oblique field with gantry angles of 342° , 306° , and 210° , a left-anterior oblique field with gantry angle of 39° , and a left-lateral field with gantry angle of 150° were used. For the VMAT plan, two half arcs with the gantry angle 181° to 0° and 0° to 181° were used. We will further investigate a feasibility of automatic determination of these parameters for the individual patients in the optimization, so that the full potential of hybrid technique can be explored and the hybrid plans can be planned and delivered together, not separately. Hoover et al. [21] investigated an optimization and delivery technique called united intensity-modulated arc therapy (UIMAT), which optimized IMRT and VMAT simultaneously and delivered IMRT and VMAT in the same arc. They found that UIMAT has the potential to be superior to IMRT or VMAT.

The Hybrid IMRT/VMAT technique can be implemented to find the optimal compromise between gantry-angle and intensity modulation degrees of freedom, dosimetric quality, and delivery efficiency. It may be delivered without switching between delivery techniques in the future. That is, hybrid

plans will be delivered as modulated arcs with IMRT inside, that is, IMRT control points (with no gantry motion) within a VMAT control point sequence (with gantry changes) rather than current two separate components, so that the delivery time would be further reduced. In addition, the emergence of autofield sequencing, which eliminates the unnecessary operator manual control of gantry rotation during dose delivery, and the dramatically increased dose rate in modern digital LINACs will make Hybrid IMRT/VMAT more efficient.

Our previous study demonstrated that some gantry angles benefited plan quality the most from beam modulation for some specific targets and OARs configuration [22]. Li and Xing [23] and Matuszak et al. [24] also demonstrated that an additional modulation from "optimal" beam angle improved plan quality compared with VMAT alone. While there were some optimal beam orientations that would benefit from IMRT, the selection of the best beam orientations for modulation might become increasingly difficult for the complicated cases. Li and Xing [23] proposed a dense angularly sampled and sparse intensity modulated RT (DASSIM-RT) strategy, in which a large number of beam angles were used to increase the angular sampling while simplifying the intensity modulation by eliminating the dispensable segments, to improve dose distribution while maintaining high delivery efficiency. In contrast with Hybrid IMRT/VMAT, DASSIM-RT utilized an IMRT delivery mode, which could be time intensive. In addition, the number of beams and intensity level were arbitrarily selected in DASSIM-RT. Matuszak et al. [24] reported a similar strategy called FusionArc and proposed and validated gradient factor as the metric to find the optimal IMRT beam directions. They used a single-arc VMAT plan as the baseline plan and then converted selected VMAT apertures with the highest gradient into IMRT beams. Different from the arbitrarily selecting the number of beams and intensity level in DASSIM-RT, and using one arc and sequentially converting IMRT beam one by one in FusionArc, in our study, the Hybrid IMRT/VMAT integrated 5 IMRT fields and 2 partial VMAT arcs, in which the optimal IMRT beam directions were created by using beam angle optimization, while the VMAT arcs were optimized with the IMRT part as a base plan.

5. Conclusions

In combining VMAT and IMRT beams, Hybrid IMRT/VMAT significantly improved both the target dose conformity and the homogeneity compared with IMRT and VMAT for nonsmall cell lung cancer. It reduced V_5 , V_{10} , V_{30} , and MLD of normal lung compared with VMAT and protected the OARs better with fewer MUs with the cost of a little higher V_5 , V_{10} , and mean lung dose (MLD) of normal lung compared with IMRT. Hybrid IMRT/VMAT technique can be a viable radiotherapy technique with better plan quality.

Conflict of Interests

This study was funded by the grant project: National Natural Science Foundation of China (no. 81071237).

References

- [1] R. R. Patel and M. Mehta, "Three-dimensional conformal radiotherapy for lung cancer: promises and pitfalls," *Current Oncology Reports*, vol. 4, no. 4, pp. 347–353, 2002.
- [2] H. Murshed, H. H. Liu, Z. Liao et al., "Dose and volume reduction for normal lung using intensity-modulated radiotherapy for advanced-stage non-small-cell lung cancer," *International Journal of Radiation Oncology Biology Physics*, vol. 58, no. 4, pp. 1258–1267, 2004.
- [3] W. Dörr and T. Herrmann, "Second primary tumors after radiotherapy for malignancies. Treatment-related parameters," *Strahlentherapie und Onkologie*, vol. 178, no. 7, pp. 357–362, 2002.
- [4] E. J. Hall, "Intensity-modulated radiation therapy, protons, and the risk of second cancers," *International Journal of Radiation Oncology, Biology, Physics*, vol. 65, pp. 1–7, 2006.
- [5] M. Pasler, D. Georg, S. Bartelt, and J. Lutterbach, "Node-positive left-sided breast cancer: does VMAT improve treatment plan quality with respect to IMRT?" *Strahlentherapie und Onkologie*, vol. 189, no. 5, pp. 380–386, 2013.
- [6] A. Holt, D. Van Gestel, M. P. Arends et al., "Multi-institutional comparison of volumetric modulated arc therapy vs. intensity-modulated radiation therapy for head-and-neck cancer: a planning study," *Radiation Oncology*, vol. 8, article 26, 2013.
- [7] S. D. McGrath, M. M. Matuszak, D. Yan, L. L. Kestin, A. A. Martinez, and I. S. Grills, "Volumetric modulated arc therapy for delivery of hypofractionated stereotactic lung radiotherapy: a dosimetric and treatment efficiency analysis," *Radiotherapy and Oncology*, vol. 95, no. 2, pp. 153–157, 2010.
- [8] C. L. Ong, W. F. A. R. Verbakel, J. P. Cuijpers, B. J. Slotman, F. J. Lagerwaard, and S. Senan, "Stereotactic radiotherapy for peripheral lung tumors: a comparison of volumetric modulated arc therapy with 3 other delivery techniques," *Radiotherapy and Oncology*, vol. 97, no. 3, pp. 437–442, 2010.
- [9] M. Rao, W. Yang, F. Chen et al., "Comparison of Elekta VMAT with helical tomotherapy and fixed field IMRT: plan quality, delivery efficiency and accuracy," *Medical Physics*, vol. 37, no. 3, pp. 1350–1359, 2010.
- [10] X. Jiang, T. Li, Y. Liu et al., "Planning analysis for locally advanced lung cancer: dosimetric and efficiency comparisons between intensity-modulated radiotherapy (IMRT), single-arc/partial-arc volumetric modulated arc therapy (SA/PA-VMAT)," *Radiation Oncology*, vol. 6, article 140, 2011.
- [11] A. Van Riet, A. C. A. Mak, M. A. Moerland, L. H. Elders, and W. Van Der Zee, "A conformation number to quantify the degree of conformality in brachytherapy and external beam irradiation: application to the prostate," *International Journal of Radiation Oncology Biology Physics*, vol. 37, no. 3, pp. 731–736, 1997.
- [12] A. S. Abbas, D. Moseley, Z. Kassam, S. M. Kim, and C. Cho, "Volumetric-modulated arc therapy for the treatment of a large planning target volume in thoracic esophageal cancer," *Journal of Applied Clinical Medical Physics*, vol. 14, no. 3, pp. 192–202, 2013.
- [13] K. Nguyen, D. Cummings, V. C. Lanza et al., "A dosimetric comparative study: volumetric modulated arc therapy vs intensity-modulated radiation therapy in the treatment of nasal cavity carcinomas," *Medical Dosimetry*, vol. 38, no. 3, pp. 225–232, 2013.
- [14] T.-F. Lee, P.-J. Chao, H.-M. Ting et al., "Comparative analysis of SmartArc-based dual arc volumetric-modulated arc radiotherapy (VMAT) versus intensity-modulated radiotherapy (IMRT) for nasopharyngeal carcinoma," *Journal of Applied Clinical Medical Physics*, vol. 12, no. 4, article 3587, 2011.
- [15] M. T. Studenski, V. Bar-Ad, J. Siglin et al., "Clinical experience transitioning from IMRT to VMAT for head and neck cancer," *Medical Dosimetry*, vol. 38, no. 2, pp. 171–175, 2013.
- [16] A. Doses, "3. Special considerations regarding absorbed-dose and dose—volume prescribing and reporting in IMRT," *Journal of the ICRU*, vol. 10, no. 1, pp. 27–40, 2010.
- [17] S. Martin, J. Z. Chen, A. Rashid Dar, and S. Yartsev, "Dosimetric comparison of helical tomotherapy, RapidArc, and a novel IMRT & Arc technique for esophageal carcinoma," *Radiotherapy and Oncology*, vol. 101, no. 3, pp. 431–437, 2011.
- [18] J. L. Robar and C. Thomas, "HybridArc: a novel radiation therapy technique combining optimized dynamic arcs and intensity modulation," *Medical Dosimetry*, vol. 37, no. 4, pp. 358–368, 2012.
- [19] H. H. Liu, M. Jauregui, X. Zhang, X. Wang, L. Dong, and R. Mohan, "Beam angle optimization and reduction for intensity-modulated radiation therapy of non-small-cell lung cancers," *International Journal of Radiation Oncology Biology Physics*, vol. 65, no. 2, pp. 561–572, 2006.
- [20] O. S. H. Chan, M. C. H. Lee, A. W. M. Hung, A. T. Y. Chang, R. M. W. Yeung, and A. W. M. Lee, "The superiority of hybrid-volumetric arc therapy (VMAT) technique over double arcs VMAT and 3D-conformal technique in the treatment of locally advanced non-small cell lung cancer—a planning study," *Radiotherapy and Oncology*, vol. 101, no. 2, pp. 298–302, 2011.
- [21] D. A. Hoover, M. MacFarlane, E. Wong, J. J. Battista, and J. Z. Chen, "Feasibility of a unified approach to intensity-modulated radiation therapy and volume-modulated arc therapy optimization and delivery," *Medical Physics*, vol. 42, no. 2, pp. 726–734, 2015.
- [22] R. Yang, J. Dai, Y. Yang, and Y. Hu, "Beam orientation optimization for intensity-modulated radiation therapy using mixed integer programming," *Physics in Medicine and Biology*, vol. 51, pp. 3653–3666, 2006.
- [23] R. Li and L. Xing, "Bridging the gap between IMRT and VMAT: dense angularly sampled and sparse intensity modulated radiation therapy," *Medical Physics*, vol. 38, pp. 4912–4919, 2011.
- [24] M. M. Matuszak, J. M. Steers, T. Long et al., "FusionArc optimization: a hybrid volumetric modulated arc therapy (VMAT) and intensity modulated radiation therapy (IMRT) planning strategy," *Medical Physics*, vol. 40, no. 7, Article ID 071713, 2013.